CHALMERS
UNIVERSITY OF TECHNOLOGY

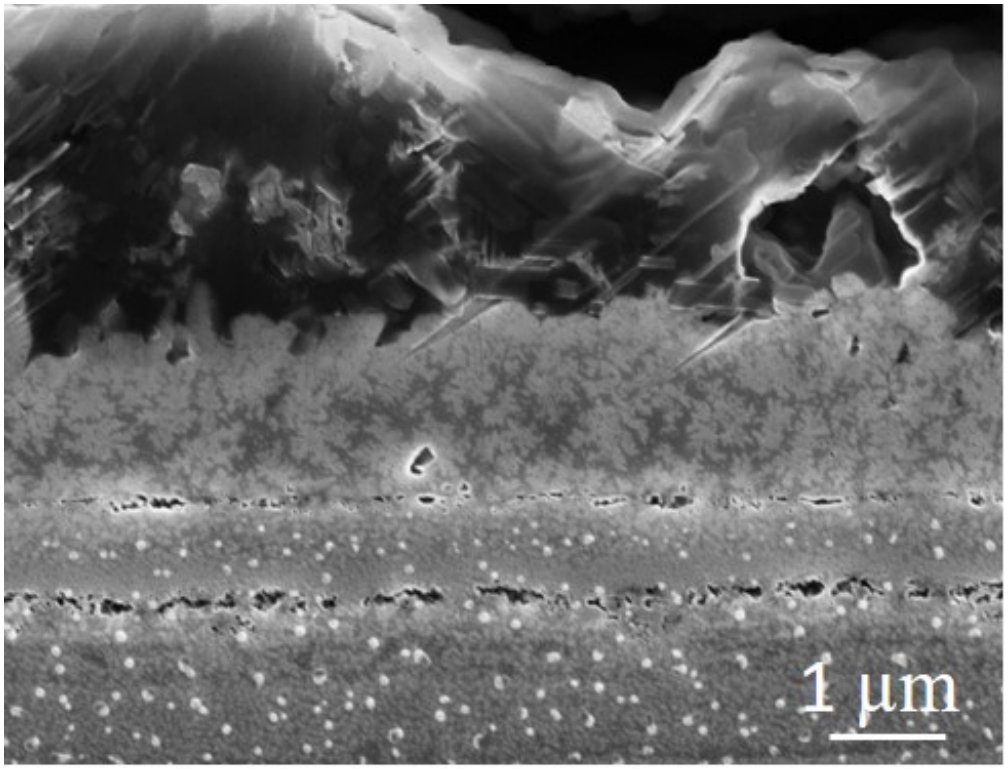

Evaluating corrosion regimes of Fe-based alloys in high temperature corrosion

A literature review combined with experimental work

Master's thesis in Materials Chemistry

JENNIE LINDSTRÖM
WALIDA SOMSRI

DEPARTMENT OF CHEMISTRY AND CHEMICAL ENGINEERING
CHALMERS UNIVERSITY OF TECHNOLOGY
Gothenburg, Sweden 2021
www.chalmers.se

Master's thesis 2021

Evaluating corrosion regimes of Fe-based alloys in high temperature corrosion

A literature review combined with experimental work

JENNIE LINDSTRÖM
WALIDA SOMSRI

CHALMERS
UNIVERSITY OF TECHNOLOGY

Department of Chemistry and Chemical engineering
Division of Energy and Materials
Chalmers University of Technology
Gothenburg, Sweden 2021

Evaluating corrosion regimes of Fe-based alloys in high temperature corrosion
A literature review combined with experimental work
JENNIE LINDSTRÖM
WALIDA SOMSRI

Supervisor: Amanda Persdotter [a]
Supervisor: Johan Eklund [a]
Supervisor: Torbjörn Jonsson [a]
Examiner: Jesper Liske [a]
[a] Department of Chemistry and Chemical engineering,
Chalmers University of Technology

Master's Thesis 2021
Department of Chemistry and Chemical engineering
Division of Energy and Materials
Chalmers University of Technology
SE-412 96 Gothenburg
Telephone + 46 (0)31-772 1000

Cover: A cross section of the oxide scale formed on Fe-18Cr-3Al after 48h exposure in 5% O_2 + 95% N_2 in presence of K_2CO_3 at 600°C, pp. 50

Printed by Chalmers Reproservice
Gothenburg, Sweden 2021

Evaluating corrosion regimes of Fe-based alloys in high temperature corrosion

A literature review combined with experimental work

JENNIE LINDSTRÖM

WALIDA SOMSRI

Department of Chemistry and Chemical engineering

Chalmers University of Technology

Abstract

In high temperature applications, breakaway corrosion is a major issue where corrosion limits the useful life of alloy components. The focus for many previous studies have therefore been on preventing this event. However, in harsh and more corrosive environments, where the protective oxide scale generally cannot be retained, the protective properties must rely on the oxide formed after breakaway. Thus, Persdotter et al. [1] introduced the concepts primary and secondary corrosion protection. The primary corrosion protection is defined as a thin, well adherent slow-growing corundum type oxide, while the secondary corrosion protection is a iron-rich multi-layered fast-growing oxide. However, by altering the alloys composition, the secondary corrosion protective may be improved.

The aim of this master thesis work is to collect data from previous studies to evaluate the applicability of the concept of primary and secondary corrosion regimes in a broader temperature range. The focus is however on the secondary corrosion protection for FeCr(Ni) alloys in various temperatures and environments. The literature review suggest that the concept can be applied in a broader temperature range but is however more complex with more factors to consider. It was observed that increasing the temperature improved the secondary corrosion protection for Fe-20Cr when isothermally exposed. In contrast, the effect of cyclic oxidation is more severe at higher temperatures for Fe-Cr alloys. In addition, under cyclic oxidation, adding Ni was shown to increase the risk of spallation since thermal stresses occur between the metal and the formed oxide. Thermal stresses more severe in alloys with high thermal expansion coefficients. Materials with an austenitic structure have a higher thermal expansion than ferritic materials and therefore a possible explanation for higher spallation risks.

The result from the experimental part indicate that an alloy with poor secondary corrosion protection also formed a similar oxide scales after spallation and stabilized around the same oxide thickness, regardless how much of the scale that was removed. Moreover, when part of the oxide scales was removed from an alloy with a good secondary protection, a thicker oxide scale was observed when re-exposed. On the contrary, when the entire oxide was removed, a similar oxide scales as a good secondary corrosion protection, was formed. This suggests that a good secondary corrosion protection may be sensitive towards cyclic oxidation and spallation in general while this have minor effect on a poor secondary protection.

Keywords: Breakaway oxidation, Fe-based alloys, High temperature corrosion, Primary corrosion protection, Secondary corrosion protection, Spallation.

Acknowledgements

In order to make this master's thesis possible during the circumstances regarding the covid-19 pandemic, we will first of all thank Torbjörn Jonsson for putting together the supervision team. We will especially thank Dr. Johan Eklund and Dr. Amanda Persdotter for all the time, support, and participation during the project.

Furthermore, we would also like to express our gratitude to Dr. Johan Eklund for performing the experiments and providing us the data for the experimental part.

Last but not least, we would like to thank our examiner Assoc. prof. Jesper Liske.

Acronyms

PP - Primary corrosion protection.
SP - Secondary corrosion protection.

POS - A slow-growing oxide scale (no spallation).
AA - A fast-growing oxide scale (no spallation).
AAS - A fast-growing oxide scale (with spallation).
SEM - Scanning Electron Microscopy.
EDX - Energy Dispersive X-ray Spectroscopy.

BCC - Body-centered cubic.
FCC - Face-centered cubic.

Contents

1

Introduction

At room temperature, most metals and alloys are thermodynamically unstable in oxygen-containing atmosphere and spontaneously react with the environment to form different oxides on the surface. However, over a wide range of conditions and at elevated temperature, the formation of corrosion products is rapid which leads to material degradation. Temperature is a factor that influence the growth of the formed oxides but other factors such as the environment and the chemical composition of the alloy also of importance [2, 3]. The properties on the oxide formed determines the corrosion resistance of the metal which is dependent of the formation of an inert, slow-growing and well-adherent oxide scale. Moreover, high temperature corrosion includes many processes such as oxidation, chlorination and carburization. In numerous commercial processes, oxidation is often the most important high temperature reaction [4].

This section describes the background behind the issue to be investigated and the aim of this master thesis work. The limitations and specifications of the issue under investigation are also considered in this section.

1.1 Background

High temperature corrosion of Fe-based alloys is a major challenge for many applications such as power plants. Alloying elements, such as chromium (Cr), aluminium (Al) and nickel (Ni) are often added in varying amounts to improve the corrosion resistance at the temperature range 400-1200 °C [1, 2, 3]. The oxides formed on stainless steel or alloys containing chromium and/or aluminium are of a slow growing corundum type oxide (M_2O_3) which act protective. However, the oxide scales formed on the metals in a certain environment can be divided into two regimes, a primary and a secondary corrosion regime. The concept of primary and secondary corrosion regimes of Fe-based alloys is introduced by Persdotter et al. [1]. In relatively mild environments (e.g. O_2), these Cr-rich and/or Al-rich oxide scales are referred to as the primary corrosion protection. The characteristic of the primary corrosion protection is the slow oxide growth rate that is diffusion-controlled and can thus be model by diffusion-based modelling tools such as DICTRA [5]. Metals and Fe-based alloys that can form protective and slow-growing oxide scales are therefore desired in most applications to be able to reduce material degradation and maintenance costs [4]. However, in harsh corrosive environments (e.g. presence of salts and/or water vapor), these protective oxide scales can break down through different

corrosion mechanism and lose their protective properties. This behavior, in which the protective oxide scale degrade, is called breakaway corrosion. The breakaway corrosion leads to a rapid formation of multi-layered iron-rich oxide scales composed of an outward-growing iron oxide (Fe_2O_3/Fe_3O_4) and an inward-growing mixed spinel ($(Fe,Cr,M)_3O_4$) [6, 7, 8, 9]. This type of oxide scale is generally considered non-protective due to its significantly higher growth rate in comparison to chromia and alumina. However, it has been shown that by changing the alloy composition, the growth rate of the Fe-rich oxide can be reduced, and hence the protective properties can be improved. Thus, the protective oxide formed after breakaway is referred as the secondary corrosion protection [1].

With regards to the breakdown of the primary corrosion protection where corrosion limits the useful life of an alloy component, many previous studies have been focused on how to prevent or delay the breakaway corrosion of these protective oxides. In the many cases where it is impossible to retain the primary protection in harsh environments during long-term operation, the lifetime of these materials must rely on the oxide scale formed after breakaway corrosion, i.e. the secondary corrosion protection [1]. However, the concept of secondary corrosion protection has not been investigated to the same extent as the primary corrosion protection, but it could be of great importance for many applications if this concept is more understood. Since the terminology of primary and secondary corrosion protection is new in the corrosion community, it is of great importance to investigate the applicability in a broader temperature range to be able to understand and to gage the robustness of the concept. In addition, this concept will also be strengthened by investigating if the spallation of a previously formed secondary protection will affect the corrosion resistance of a new secondary protection.

1.2 Aim

The aim of this master thesis work is to investigate and evaluate corrosion regimes for different Fe-based alloys with varying Al, Ni and Cr content in the temperature range 400-850 °C. The scope and focus will be on the secondary corrosion protection but also to provide a broader understanding and applicability of the concept in high temperature corrosion. The purpose is also to do a literature review on these concepts and combine it with new experimental results.

1.3 Limitations

As mentioned above, this thesis work will be focused on the secondary corrosion protection. The primary corrosion protection will therefore not be investigated. The investigation will be focused on the temperature range 400-850 °C, higher temperature will thus not be considered.

1.4 Specification of issue under investigation

The issue under investigation is specified by answering the following questions:

1. How does the alloy compositions affect the secondary corrosion protection?
2. How does the temperature affect a poor respective a good secondary protection?
3. How does the spallation of a previously formed secondary protection affect the corrosion resistance of a new secondary protection?

2

Theory

In order to understand the concept of the primary and secondary protection, knowledge about the underlying theory of high temperature corrosion is necessary. The following section and subsections present general information about Fe-based alloys including the microstructures, followed by information about oxidation of metals. In addition, information about thermodynamic and kinetics, corrosion products, the different corrosion regimes and the influence of salt will also be presented.

2.1 Metal alloys

Alloys are compounds that consist of at least 2 elements where one of them is a metal and the other one is either a metal or a non-metal. A common non-metal that is used to produce alloys are carbon. For instance, carbon steel is an alloy consisting of iron and carbon [10]. When it comes to Fe-based alloys, there are different names to describe the metallic component of the material that mostly represent about 90% or more as the base metal, parent metal or the main metal. A base metal, common in high temperature corrosion applications is iron. The other element which are involved together with the base metal are refereed to alloying agents. The alloying agents are usually present in small quantities and can be less than 1% of the total material. Common alloying agents in high temperature corrosion are chromium and aluminium [2].

2.2 Microstructures

The most common phases of steels are ferrite and austenite. The microstructure of a steel can be made up of both the ferrite and austenite phases simultaneously and is then called a duplex steel. Another microstructure is martensitic but in this thesis the focus will be on ferrite, austenite and austenite-ferrite for the literature review [11].

2.2.1 Ferrite

Ferrite has a crystal structure known as body-centered cubic (BCC). The unit cell of the BCC structure is shown in Figure 2.1. From the Figure one can see that the unit cell consists of 1 atom in the centrum and 1/8 atom at each corner. The total number of atoms in a BCC unit cell is 2 [12].

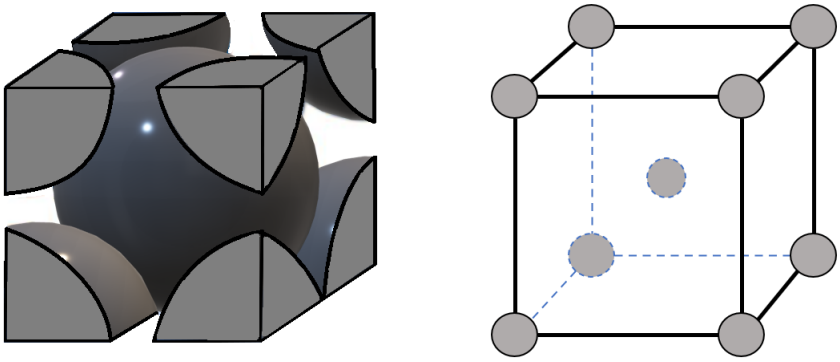

Figure 2.1: *Illustrate the unit cell of the body-centered cubic crystal structure. Inspiration from [13].*

In Figure 2.2, the surface morphology of ferrite is shown. Furthermore, the properties of a material changes depending on which phase that occurs. A ferritic material have the properties to be poor conductors when it comes to conduct electricity. Other typical properties of ferrites is that they are brittle and hard. Moreover, ferrites can be further divided into 3 other divisions, soft-, semi-hard and hard ferrites but this will not be further described in this thesis [14].

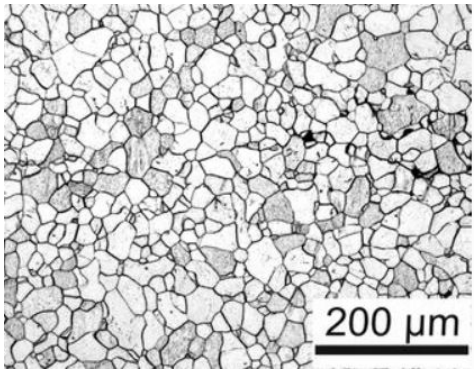

Figure 2.2: *Microstructure/surface morphology of ferrite [11].*

2.2.2 Austenite

Austenite has a different crystal structure compared to ferrite and is called face-centered cubic (FCC). In Figure 2.3 the unit cell of the FCC structure is shown. From the Figure one can see that the total number of atoms in an FCC unit cell is 4, since there is 6×1/2 atoms at each side and 8×1/8 atoms from the corners [12].

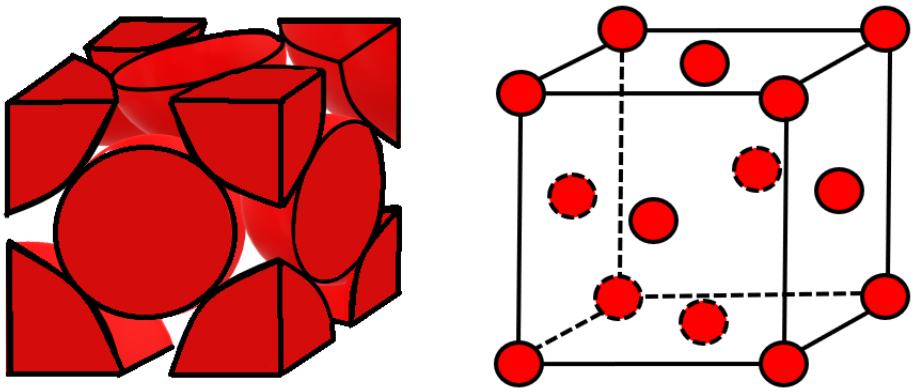

Figure 2.3: *Illustrate the unit cell of the face-centered cubic crystal structure. Inspiration from [15].*

In Figure 2.4, the surface morphology of austenite is shown. The austenitic phase characterize by the grain structure and forms when nickel is added in the alloy. It needs a certain amount of nickel in an Fe-based alloy in order to reach a transition from ferrite to austenite. One example is that an alloy that contains 18% chromium needs between 8-10% nickel to be considered as an austenitic phase [16].

Regarding the properties of the austenite phase is that it is very ductile and tough even at low temperatures. Austenitic phases also have high strength and toughness even at elevated temperatures [16].

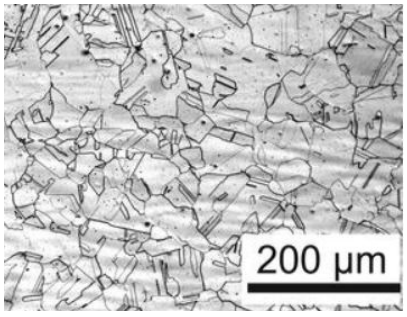

Figure 2.4: *Microstructure/surface morphology of austenite [11].*

2.2.3 Austenite-ferrite

A steel called duplex is characterized by its phase structure and is made up of the two phases that were previously described, austenite and ferrite but simultaneously. In Figure 2.5, the surface morphology of austenite is shown. Furthermore, the properties of a duplex steels is among other things, higher strength and higher thermal conductivity compared to just austenite itself [11].

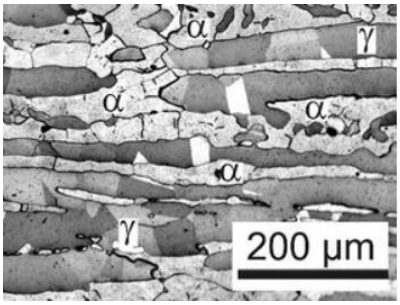

Figure 2.5: *Microstructure/surface morphology of austenite-ferrite [11].*

2.3 Oxidation of metals

Metal oxidation is the chemical reaction between metals and oxygen according to reaction 2.1, where M refers to the metal, O the oxygen and M_xO_y the metal oxide [2].

$$\mathrm{xM\,(s)} + \frac{\mathrm{y}}{2}\,\mathrm{O_2\,(g)} \rightarrow \mathrm{M}_x\mathrm{O}_y\,\mathrm{(s)} \tag{2.1}$$

The reaction take place if it is energetically feasible. However, whether or not a reaction take place will be explained by thermodynamics in the next subsection. Furthermore, the properties of the oxide formed determines the corrosion resistance of metal, which will be covered in the subsection Oxidation kinetics.

2.3.1 Thermodynamics

Ellingham diagrams are a common tool when it comes to high temperature oxidation of metals and was constructed by Harold Ellingham for the first time in 1944. Ellingham diagram provides information on which reaction is the most likely one to occur for a given metal when it comes to the prediction of spontaneous oxidation. There are some limitations/disadvantages with the Ellingham diagrams and that is that no kinetics of the reactions is considered [17].

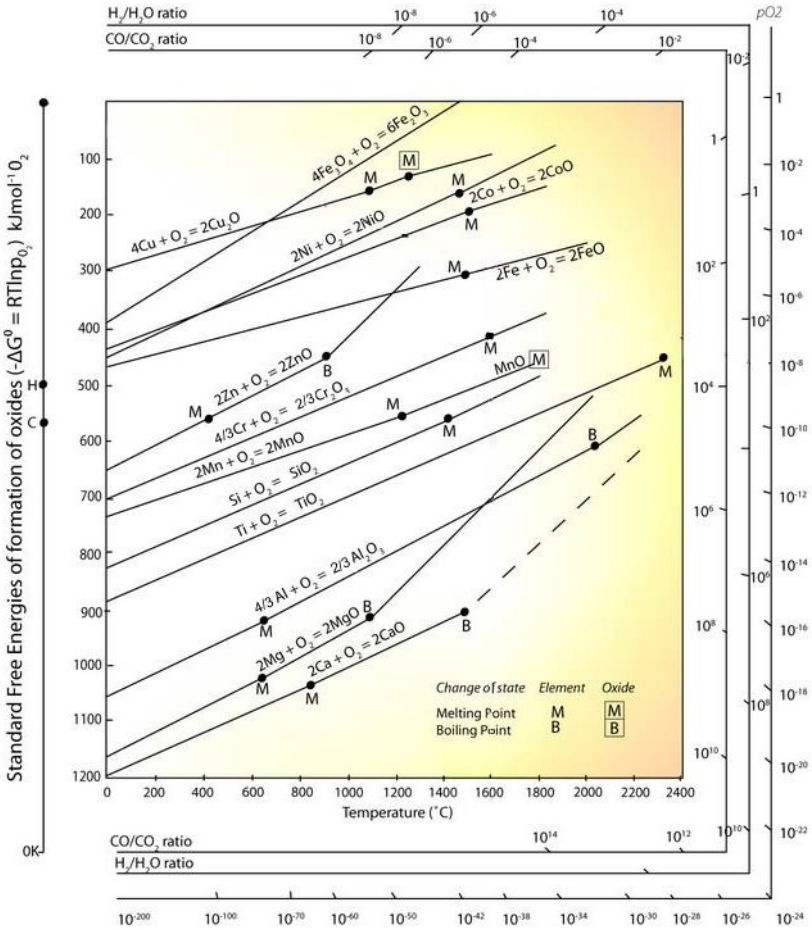

Figure 2.6: *Showing an example of an Ellingham diagram for a few metals. The diagram can be used to predict if the oxide is stable when the oxygen partial pressure is varying as it does when oxide scales grows in alloys at different depths [18].*

The diagram illustrates the Gibbs free energy as a function of temperature and this temperature-dependence is graphically represented in Figure 2.6. There are both straight lines and lines were the slope at some point gets a higher gradient, for instance in the case when magnesium are oxidized into magnesium oxide, as in Reaction 2.2

$$2\,\mathrm{Mg} + \mathrm{O_2} \rightarrow \mathrm{MgO} \tag{2.2}$$

This increase of the slope is due to phase changes when the metal goes from a liquid state into a gaseous state for example. These phase changes are denoted in Figure 2.6 as M and B were M represents the melting point and B represents the boiling point of the element. For the oxide, the notation for the melting point and boiling point are $\boxed{\mathrm{M}}$ and $\boxed{\mathrm{B}}$, respectively.

To be able to understand the thermodynamics of oxide formation it is necessary to be familiar with the Gibbs free energy. The definition of Gibbs free energy at standard states

is formulated in Eq. 2.3

$$\Delta G^\circ = \Delta H^\circ - T\Delta S^\circ \tag{2.3}$$

Were G is the Gibbs energy, H is the enthalpy, T is the temperature and S is the entropy. At equilibrium, ΔG° is equal to –RTlnK. To illustrate how the Ellingham diagram works and how to use it, select first a temperature of interest, draw a vertical line from that point on the x-axis up to the line that represents the metal oxidation of interest. The next step is to look on the left y-axis and draw a line from the black dot "O" through the intersect of the earlier drawn vertical line and continue to the right y-axis named pO_2. The point on the pO_2-axis determines the dissociation pressure of oxygen (O_2) and this indicate the lowest value regarding the oxygen partial pressure where the chosen oxide can form. In other words this means that above and at that value of the determined pO_2 the oxide can form and below that value the metal is not oxidized.

2.3.2 Oxide formation and growth

The oxidation process can be divided into three steps as illustrated in Figure 2.7. The initial step involves the adsorption of oxygen from the environment on the metal surface. The adsorbed oxygen is reduced to oxygen ions (O^{2-}) at the surface with electrons from the metal. The oxygen ions then react with metal cations (M^{n+}) to form oxide nuclei that will grow laterally until it completely covers the surface with a thin film. Factors such as function of surface orientation, crystal defects at the surface, surface preparation, and impurities in both the metal and the gas influence both the adsorption and the initial oxide formation [2, 17].

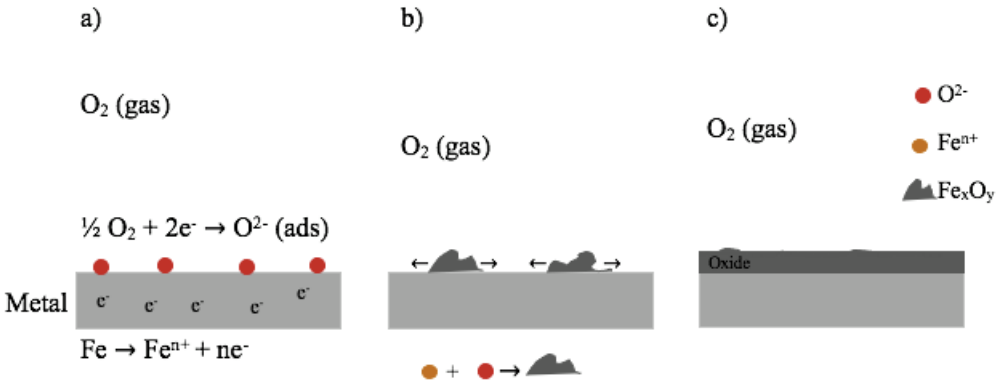

Figure 2.7: *Illustration of the oxide formation on a metal surface. a) The oxygen is absorbed and reduced at the surface. b) The metal cations and oxygen anions react and form an oxide nucleus. c) The nuclei grow laterally until a continuous and thin film covering the surface. The drawing is inspired by [19, 20].*

When the surface is completely covered and no longer in contact with the oxidizing environment, the thin film will continue to grow in thickness by diffusion of the ions and electrons through the film. Thus, for the reaction to continue, metal cations (M^{n+} or Fe^{n+}) must be transported through the oxide to the oxide-gas interface (outward growing) or anionic oxygen (O^{2-}) must be transported to the oxide-metal interface (inward growing), as illustrated in Figure 2.8 [21].

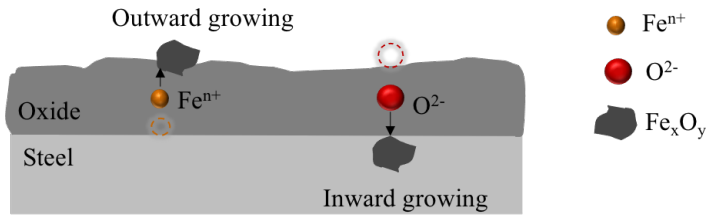

Figure 2.8: *Schematic illustration of outward and inward growing oxide scale formed by transport of cationic metal ions and anionic oxygen ions respectively. Figure inspired by [20].*

The growth of the oxide therefore depends on the diffusion of ions and electrons through the oxide. The diffusion can be divided into two groups depending on what type of defects that is used to transport the ions. It is called lattice diffusion (bulk diffusion) if the diffusion occurs through point defects such as vacancies and interstitial. The diffusion by vacancies occurs by the movement of an ion in an ordinary site to an adjacent vacancy which leaves behind a new vacancy so that the process can be continued, Figure 2.9a. Similarly, the diffusion of interstitial ion occurs by movement from one interstitial site to an adjacent interstitial sites as illustrated in Figure 2.9b [2, 17]. In addition, ions can also diffuse along line defects such as grain boundaries, dislocations, voids and cracks in the scale. This type of diffusion is faster than bulk diffusion and is thus called short-circuit diffusion [2].

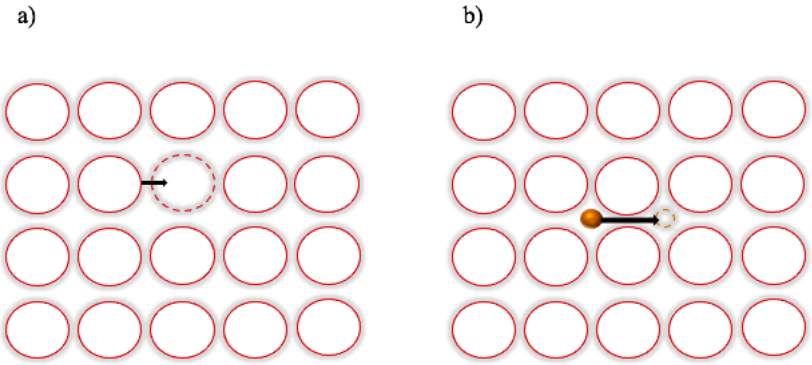

Figure 2.9: *Illustration of lattice diffusion by a) vacancy diffusion and b) interstitial diffusion. The drawing is based on [20].*

The rate of diffusion for both mentioned diffusion types (lattice and short-circuit) can be described by Eq. 2.4, where D is the diffusion coefficient, D_0 is the frequency factor which is temperature dependent, and Q_D is the activation energy for diffusion to happen. The diffusion coefficient varies for different type of diffusion and depends on the element, phases and temperature [2].

$$D = D_0 e^{-Q_D/RT} \tag{2.4}$$

At lower temperature, below 600 °C, the short-circuit diffusion is more favored than lattice diffusion which is due to its lower activation energy [2]. Moreover, lattice diffusion have much slower diffusion which leads to greater flux of atoms along the grain boundaries [19]. However, at higher temperature, the lattice diffusion becomes more important, but this depends on factors such as partial pressure, porosity, defect concentration and grain size (i.e. grain boundary area) [2]. Since the grain size have an effect on the diffusion, the corrosion resistance will therefore also be affected by the grain size. Both of the diffusion type are relevant and important for this study since the temperature to be investigated is between 400-850 °C.

2.3.3 Oxide defects

The transportation of ions and electrons though the oxides occur through defects in the crystal structure of the oxide as previously mentioned. All materials contain defects, but the nature and number of defects can vary considerably from one material to another one. In addition, different kind of defects in the crystal structure results in different diffusion paths and mechanisms. There are two groups of defects, point defects and line/surface defects [2].

Point defects

Points defects in the form of the Schottky and Frenkel defects are the most important in stoichiometric oxides such as Al_2O_3 and SiO_2, which have low concentration of point defects due to the number of cations and anions are in balance. In the case of Schottky defects, as illustrated in Figure 2.10a, equal number of anions and cations are missing in the lattice (ionic vacancies) and the transport of both species is therefore possible. For Frenkel defects, the anion or cation (usually cation) is displayed from it normal lattice site and moved to a nearby interstitial site which create a vacancy, as showed in Figure 2.10b. The transport of both species is also possible for Frenkel defects [21].

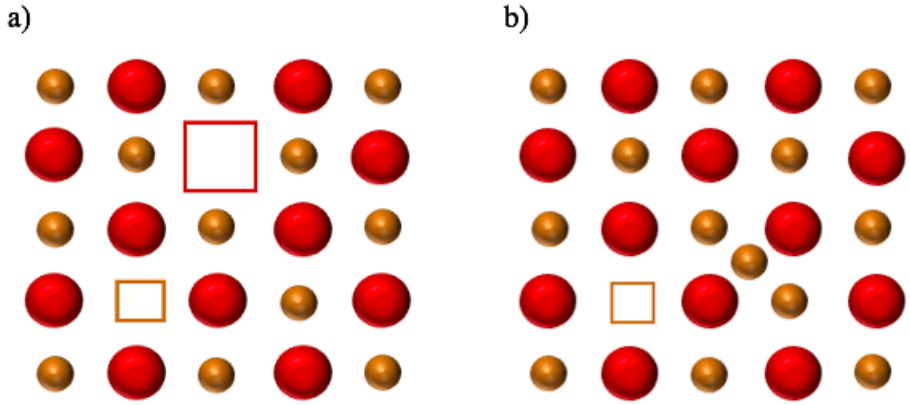

Figure 2.10: *Illustration of stoichiometric oxide defects: a) Schottky defect and b) Frenkel defect.*

For the oxidation reaction to proceed, electrons and ions/neutral atoms must be transported through the oxide. However, both mentioned defects types only provide information about the ion mobility but not the electrons migration. Hence, in order to study the migration of ions and electrons it is necessary to assume that the oxides formed are non-stoichiometric [21].

Non-stoichiometric oxides (e.g., $M_{1-x}O$) are oxide for which the ratio of the metal and oxygen is not exactly that is given by the chemical formula such as Fe_2O_3. In comparison to the stoichiometric oxides, non-stoichiometric oxides have higher defect concentration and are better ion conductors. Thus, these oxides are also classified as semiconductors and are divided into two types, n-type and p-type semiconductors [21].

The negative (n-type) semiconductors are oxides with either metal excess or oxygen deficit in the form of metal ion interstitials respective oxygen vacancies, as presented in Figure 2.11. This results in a positive charge which is compensated with excess of electrons to maintain the charge neutrality. The charges are therefore transferred by negative carriers. The ionic transport for the n-type semiconductors occurs by interstitial diffusion if there is an excess of metal ions (outwards) or diffusion of vacancies in the case of oxygen deficiency (inwards) [17, 21].

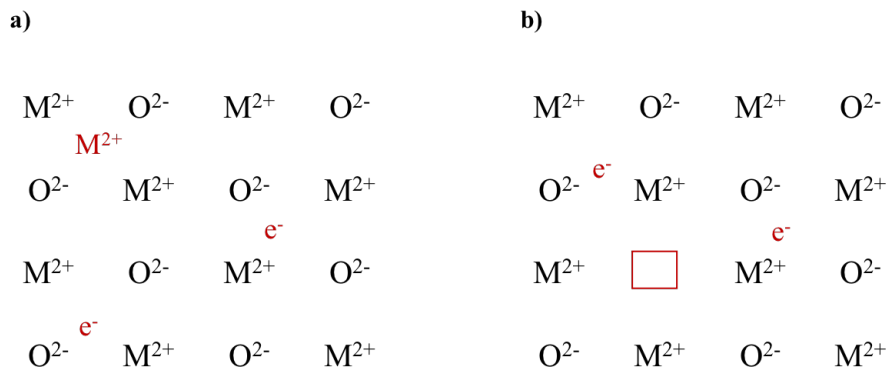

Figure 2.11: *Illustration of n-type semiconductors a) Metal excess and b) Oxygen deficit.*

However, if the charges are transferred by positive carriers, this type of semiconductors are referred as positive (p-type). The p-type is thus the opposite of the n-type with either metal deficit or oxygen excess, see Figure 2.12, and the ionic transport occurs by diffusion of vacancies and interstitial diffusion respectively [17, 21].

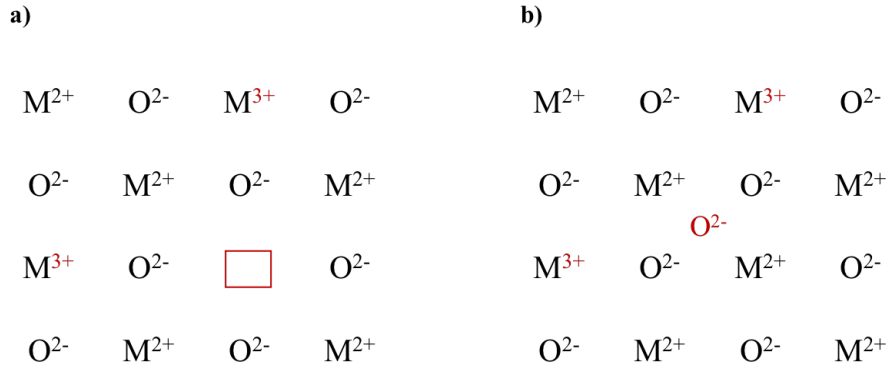

Figure 2.12: *Illustration of p-type semiconductors a) Metal deficit and b) Oxygen excess.*

Line defects

Other defects such as line dislocations and grain boundaries are classified as line and surface defects. Line defects or dislocations are deviation from a periodic arrangement of atoms along a line. Surface defects are defects that arises at the boundary between grains that have different crystallographic orientation [22]. Grain boundaries are more reactive and have higher energy state than the grains, as a consequence, impurities tend to segregate along these grain boundaries [23]. Both of these defects are important for stoichiometric oxides which enable short-circuit diffusion through the oxide.

2.3.4 Oxidation kinetics

Studies of reaction rate and kinetics provide information about the reaction mechanism and the rate-limiting step of the total reaction. It is therefore important to gain knowledge about these to be able to estimate the lifetime of the metal to be used at a specific temperature and environment [2, 24].

For a particular metal, the reaction rates and corresponding rate equations depends on several factors. Temperature, oxygen pressure, elapsed time of reaction, surface preparation, and pre-treatment of the metals are example of factors that influence the reaction rates [2]. The kinetics of high temperature oxidation are usually studied experimentally by for example thermogravimetry which is the measurement of mass change as a function of temperature or mass change as a function of time at a constant temperature called isothermal oxidation. In addition to the isothermal tests, the tests can also be carried out under thermal cycling. These types of test begin with exposure of the sample at high temperature for a specified exposure time, followed by cooling and end with measurement of mass change, then this is repeated for several cycles. These types of tests provide information about the stability of the oxide scale for instance by studying the effect of thermal stresses that occur during thermal cycling [24].

The mass gain, which is proportional to the thickness of the formed oxide, can be used to estimate oxidation rate [17]. The mass gain can be plotted as a function of exposure time or number of cycles and the obtained curves is illustrated in Figure 2.13. The oxidation follows three different rate laws, i.e., linear, parabolic, and logarithmic. However, the curves obtained experimentally may differ from the curve showed in Figure 2.13.

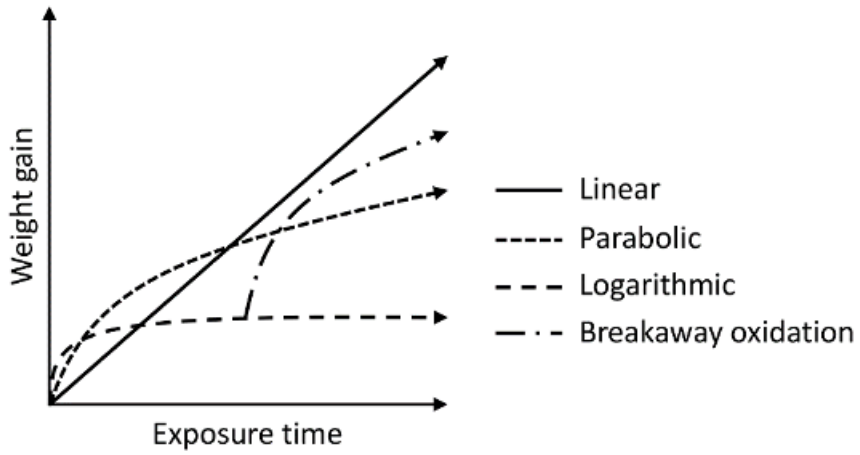

Figure 2.13: *Kinetic rate laws during oxidation and breakaway oxidation [19].*

Metals with constant rate of oxidation which is independent of the amount of gas or metal previously consumed in the reaction, follow the linear rate law. In this case, the rate of reaction is proportional to time and is given by Eq. 2.5 [2],

$$x = k_l t + C \tag{2.5}$$

where x is the oxide thickness, k_l is the linear rate constant, t is the exposure time and C is the integration constant. This type of growth rate is controlled by phase boundary or surface reaction, meaning that the oxygen supply from the atmosphere to the interface is rate determining when the diffusion through the oxide scale is rapid [2]. Metals and alloys that follows this rate law do not form protective oxides[17].

At high temperature, the oxidation of many metals follow the parabolic rate law which is controlled by the diffusion of ions and electrons though the initially formed oxide scale and is given by Eq. 2.6,

$$x^2 = k_p t + C \tag{2.6}$$

where x is the oxide thickness, k_p is the parabolic rate constant, t is the exposure time and C is the integration constant. Since the growth rate is controlled by the transport of ions and electrons through the oxide scale, the rate will decrease when the thickness is increased due to longer diffusion distance [2]. This parabolic rate law was first derived by Wagner [25] with a few assumptions and some are list below.

- The oxide layer is compact with good adhesion to the surface.
- Oxygen solubility in the metal is assumed to be negligible.
- Thermodynamic equilibrium is established in both interfaces (metal/oxide and oxide/gas).
- The migration of ions is rate-determining.

The third rate law, which is called logarithmic rate law, is used to describe oxidation of metals at low temperatures, generally around 300-400 °C. At the beginning, the oxidation rate is rapid but it will decelerate over time to low or negligible oxidation rates. This behavior follows either a direct or inverse logarithmic law and can be described by Eq. 2.7 and Eq. 2.8 respectively [2]:

$$x = k_{log} log(t + t_0) + A \tag{2.7}$$

$$\frac{1}{x} = B - k_{il} log(t) \tag{2.8}$$

where x represents the oxide thickness, t is the exposure time, k_{log} and k_{il} are the rate constant for direct and inverse logarithmic rate equations respectively and A and B are constants.

It has been found that the kinetics of oxidation of metals are not only governed by the three rate laws, as can be seen in Figure 2.13 the breakaway oxidation is also common. The breakaway oxidation is a combination of the rate laws. The oxidation kinetics at the beginning follows the parabolic rate law or logarithmic, then suddenly change to linear kinetics due to appearance of cracks and pores in the oxide layer which accelerate the growth rate or the protective oxide break down and a less protective oxide start to grow [2, 24]. This behavior is usually observed at high temperatures and in hash environments, where protective oxide layer break down and lose its protective properties.

2.3.5 Corrosion products

Depending on the alloy composition, different corrosion products are formed. For Fe-based alloys are wüstite ($Fe_{1-y}O$), hematite (Fe_2O_3), magnetite (Fe_3O_4) and mixed spinel ((Fe_{1-x}, $Cr_x)_3O_4$) common oxidation products. Other corrosion products are $(Cr_x)_3O_4$, chromium oxide (Cr_2O_3) and aluminium oxide (Al_2O_3). Some of these corrosion products are covered in the following subsections. But before getting into the corrosion products, one should keep in mind that the content of iron oxide in Fe-based alloys is higher nearest the metal. Furthermore, this also means that the oxygen partial pressure is higher nearest the source of the oxygen [2, 17].

Wüstite ($Fe_{1-y}O$)

The chemical notation of wüstite is $Fe_{1-y}O$. This indicate that $Fe_{1-y}O$ have some sorts of nonstoichiometry. The formula also implies that wüstite is metal deficient. Metal deficient means that a cation is missing in the lattice site and is a type of defect in the material. In order to obtain electrical neutrality the metal ions closest to the cations vacancies

get 2 positive charges instead. This is only possible to obtain in materials with metal ions of variable valencies such as iron. This in turned means that $Fe_{1-y}O$ is a p-type semiconductor [2, 17].

The crystal structure of wüstite is defined to have the NaCl structure, as can be seen in Figure 2.14. The NaCl structure is in turn referred to the FCC structure. However, since the structure of wüstite have low degree of stoichiometry a consequence regarding the rate of diffusion is that the ions diffuses more quickly than ions in other Fe-based oxides like hematite and magnetite as will be described later on. The rate of ion diffusion in wüstite is of importance because a high rate of diffusion provides a thick oxide scales at short times [2].

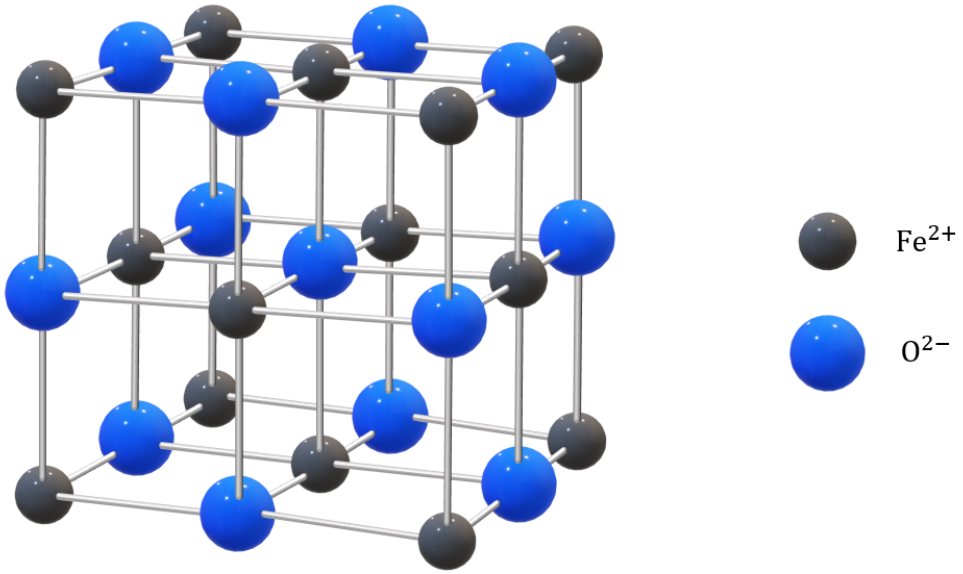

Figure 2.14: *Illustrates the NaCl structure of wüstite but with iron and oxygen ions instead.*

Hematite (Fe_2O_3)

α-Fe_2O_3 is the chemical formula for hematite and a common oxidation/corrosion product of Fe-based alloys. Hematite is one of the 16 different oxides obtained from iron and it is also the oldest known. Hematite have a crystal structure, known as the corundum structure and is shown in Figure 2.15 [26].

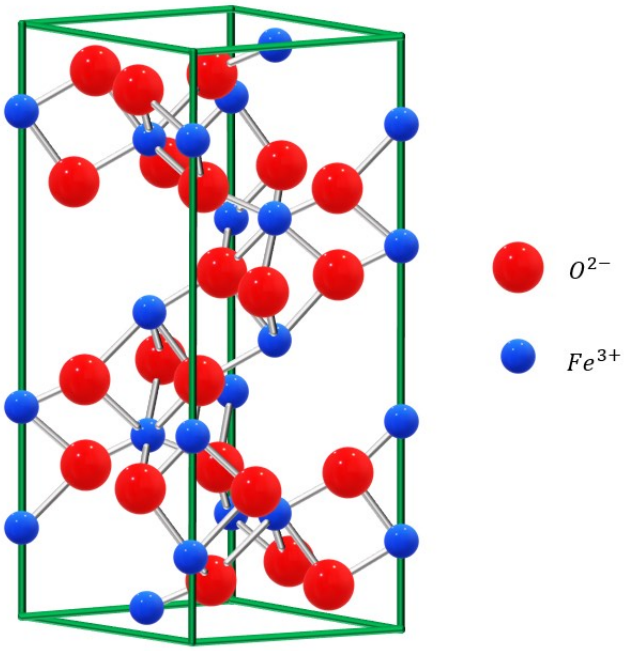

Figure 2.15: *Illustrates the corundum structure of hematite (α-Fe_2O_3). Inspiration from [27].*

When it comes to the diffusion of hematite, the self-diffusion of oxygen and iron is very slow in single-crystal Fe_2O_3 and this is due to the high degree of stoichiometry of hematite. Regarding the conductivity of Fe_2O_3 it has been shown that hematite act as an n-type semiconductor at temperatures between 650-800 °C and above 800 °C as an p-type semiconductor [2].

Magnetite (Fe_3O_4)

Magnetite have the chemical formula Fe_3O_4 and belongs to the crystal structure spinel. Magnetite can also appear as an inverse spinel structure and this happens at room temperature and at temperatures below room temperatures. The spinel structure of magnetite is defined to have a cubic crystal system where the iron ions (Fe^{2+} and Fe^{3+}) occupying the tetrahedral and octahedral sites. To be more precise for alloys, the Fe^{2+} ions compete and occupies the tetrahedral sites while the Fe^{3+} ions occupies the octahedral sites.

The oxygen ions has an cubic closed-packed system [2]. In terms of electric conductivity, magnetite has been determined to be an p-type semiconductor [17]. Magnetite has lower stoichiometry than hematite and this cause the ion diffusion to be faster in magnetite compared to hematite. As a result, this also means that the growth rate of the oxide scales is faster in magnetite than in hematite [2].

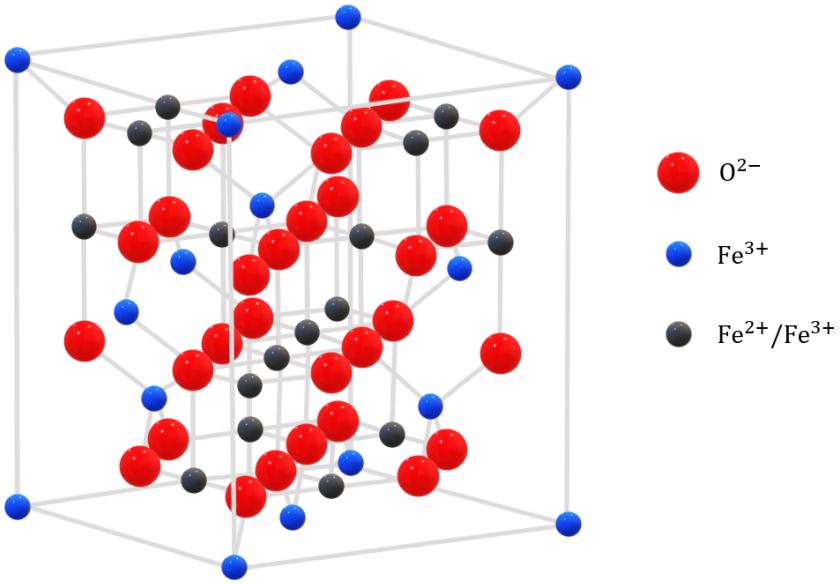

Figure 2.16: *Illustrates the inverse spinel structure of magnetite. The normal spinel structure is obtained if Fe^{2+}/ Fe^{3+} (black spheres) switch position with the Fe^{3+} (blue spheres). Inspiration from [28].*

Chromium oxide (Cr_2O_3)

Chromium oxide, Cr_2O_3 is a relevant corrosion product to know about especially in high temperature corrosion since it is the only stable solid Cr_2O_3 at high temperatures. The Cr_2O_3 has the corundum structure and this is the same structure as hematite, earlier shown in Figure 2.15 but in the case of Cr_2O_3 the Fe^{3+} ions is instead replaced by Cr^{3+} ions in Figure 2.15. This also means that the octahedral sites, more precise 2/3 of them are occupied of Cr ions. The oxygen ions is on the other hand close-packed in a hexagonal pattern [2].

On the subject of diffusion in chromium oxide, typically in the case of single-crystals of Cr_2O_3, the self-diffusion of Cr is extremely low. This indicate that the growth rate of the Cr scale is very low. This low growth rate still applies at high temperatures. Further on, this slow diffusion of Cr is connected to the high degree of stoichiometry that Cr_2O_3 have [2].

Regarding the conductivity of the Cr_2O_3 if it is a p-type or n-type semiconductor. The type of semiconductor depends on the partial pressure of O_2 [2].

Aluminium oxide (Al_2O_3)

Another type of metal oxide is the aluminum oxide, Al_2O_3 and is also called alumina. Alumina have the properties to be the only solid stable oxide of aluminium from a thermodynamic point of view. There are different types of alumina and α-Al_2O_3 and γ-Al_2O_3 are the two most common types of the oxide. Studies have shown that γ-Al_2O_3 is the type one can see below 900-1000°C and above this temperature range the α-Al_2O_3, but the α-phase can also occur at lower temperatures. The reason for why one often only see the γ-Al_2O_3 at lower temperature range is because it takes longer times for it to form. In other words this means that if long enough time have passed, the γ-Al_2O_3 transforms into α-Al_2O_3. The transformation from γ-Al_2O_3 to the α-Al_2O_3 in practice occur through heating. Studies have also shown that the α-Al_2O_3 is the form that are the stable one in terms of thermodynamics [2].

In the case of structure, both the α-type and the γ-type have the corundum structure like Cr_2O_3 and Fe_2O_3, but in this case with Al ions instead of Cr and Fe ions in Figure 2.15.

2.3.6 Primary & Secondary protection

The formed oxide may act protective or non-protective depending on the growth rate of the oxide. For stainless steel and Fe-based alloys, the primary protection relay on the formation of a thin, slow-growing Cr-rich (Cr_2O_3) or Al/Cr-rich (Al_2O_3/Cr_2O_3) corundum type oxide scale. These primary protective oxide scale acts as a barrier between the metal and the atmosphere and is slow-growing, well-adherent and dense [1, 2, 3].

However, in harsh or more corrosive environment where the primary corrosion protection rapidly breaks down, the oxidation will proceed through the formation of a faster-growing Fe-rich oxide. This breakdown is referred to as breakaway corrosion. The breakdown of the primary corrosion protection can also be induced by cracks and spallation, where the direct contact between the metal and the atmosphere will be restored which lead to acceleration of oxide growth and the protective oxide breaks down. The oxides formed after breakaway are thick, faster-growing multi-layered Fe-rich oxides (inward-growing mixed spinel ($(Fe,Cr,M)_3O_4$) and outward-growing Fe oxide (Fe_2O_3/Fe_3O_4)) [6, 7, 8, 9]. Moreover, recent studies have showed that the oxide scale formed after breakaway at 600 °C may act more or less protective depending on the chemical composition of the alloy [1, 29]. Thus, the protective properties of these oxides that are formed after breakaway can be improved and these type of oxides are referred as secondary corrosion protection.

The different corrosion regimes of Fe-based alloys were introduced by Persdotter et al. [1]

and is illustrated by means of growth kinetics in Figure 2.17. The figure clearly show the different corrosion regimes and the transition between the primary and secondary corrosion regimes (see A_1 and A_2). The most important to know from the graph for this thesis work is that there are two behavior within the secondary corrosion regime: fast-growing (see A_2, B) and a more slow-growing (see C). The former is referred as poor secondary corrosion protection and the latter as good corrosion protection. This indicates that the growth rate after breakaway corrosion can be influenced and that the corrosion resistance can be improved if the oxide is slow-growing.

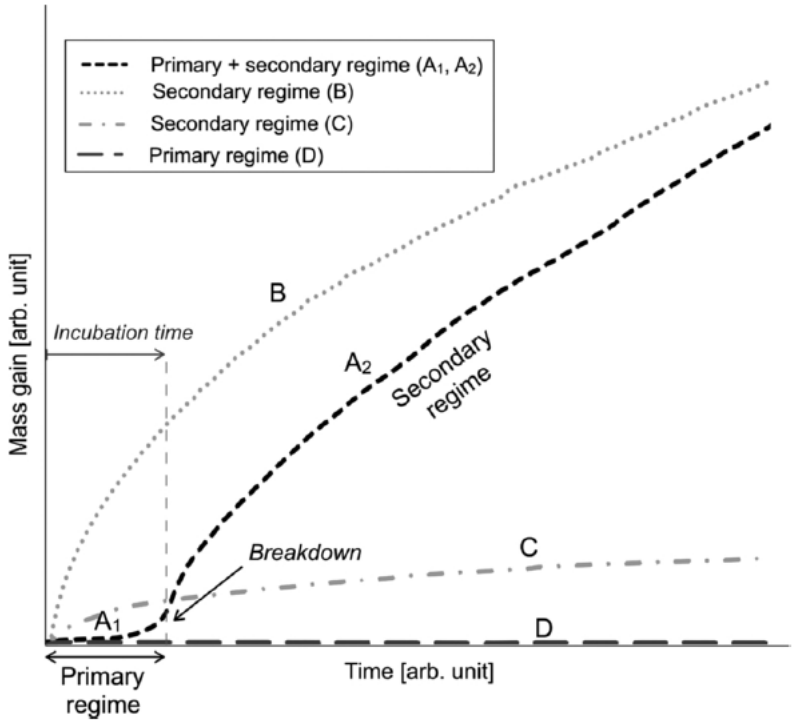

Figure 2.17: *Illustration of the different corrosion regimes for Fe-based alloys by means of growth kinetics.The transition from primary to secondary corrosion regimes are showed in curve A_1 and A_2 [1].*

2.3.7 Influence of salts

For studies in high temperature corrosion it is common to use different types of salts to induce the corrosion rates. Examples of such salts are KCl, NaCl, Na_2SO_4, K_2CO_3 and K_2SO_4. The salts can also be combined to form a salt mixture. This kind of salt-induced corrosion behavior when it comes to gaseous or solid salts are referred to hot corrosion. The influence of the corrosion behavior of salts depends on factors like velocity and composition of the gas, the salt condition and composition. There are various types of salts that can be used in hot corrosion but a common one include the usage of sulphates, e.g. Na_2SO_4 as earlier mentioned [2].

The mechanism of chloride-induced corrosion is not fully understood but have been investigated to a large extent. A early study, more specifically, a study by Grabke et al. [30] proposed a mechanism called active oxidation where Cl_2 played a major roll in the corrosion process. However, a more recent study which is by Folkesson et al. [31] indicated that the Cl_2 was not the diffusing species but chloride ions were. The diffusion of these chloride ions occurred inwards through grain boundaries where at the oxide/metal interface iron chlorides ($FeCl_2$) were formed. It have also been showed that the cations (e.g Na and K ions) react with Cr in the protective oxide scale and form alkali chromates (e.g. Na_2CrO_4 and K_2CrO_4) [32]. This reaction depleted the Cr-rich oxide which resulted in a rapid growing Fe-rich oxide [33, 34]. Thus, it was suggested that the initial break-down of the protective oxide was caused by Na/K and that Cl only play a minor roll. Cracks and spallation was however attributed to the presence of $FeCl_2$ [31].

3

Methodology

This master thesis work will be divided in two parts where the first part is a literature review to collect data from previous studies in order to gage the applicability of the concept of primary and secondary corrosion protection implemented by Persdotter et al. [20] in a broader temperature range and in different environmental conditions. The second part is an experimental part where materials known to form poor or good secondary protection will be investigated for the purpose of evaluating the influence of spallation on the corrosion resistance within the secondary corrosion regime.

The main part of the literature review is to search/collect information through different databases such as Web of science and SienceDirect, with the keywords: high temperature corrosion, breakaway corrosion and breakaway oxidation. The focus will however be on the applicability of the secondary protection in the temperature range 400-850 °C. Thereafter will the collected data be analyzed and discussed.

3.1 Selection of alloys

This section is intended to cover the Fe-based alloys that was investigated in the experimental part and these are listed in table 3.1.

Table 3.1: *Composition of the different Fe-based alloys that were studied. The chemical composition are based on wt-%.*

Alloy	*Fe*	*Cr*	*Al*
Fe5Cr3Al	Bal.	5	3
Fe10Cr3Al	Bal.	10	3
Fe18Cr3Al	Bal.	18	3
Fe25Cr3Al	Bal.	25	3

3.2 Sample preparation

The sample preparation and exposures and other experimental works in this thesis work were performed by the supervisor, Dr. Johan Eklund.

For the experimental part, the influence of spallation on the corrosion resistance within

the secondary corrosion regime was investigated. The investigated materials in this thesis were first prepared before the furnace exposures. The chosen alloys (see Table 3.1) were first melted, one at a time in a vacuum induction furnace to get 1 kg ingots. In order to get strips of each alloy, the ingots were hot-rolled and further machined to reach the thickness of 2 mm. The strips were heated one more time at 950°C to achieve even grain size distribution. Later on, the strips were cut into coupons with dimensions of 10 x 12 and a 1.5 mm hole was drilled in each coupon to simplify the weighing. The coupons were then ground on SiC paper (P4000 to P4000) and polished to a glossy mirror-like appearance with diamond suspension before exposure. In more detail the polishing step was divided into 2 steps. In the first step a diamond suspension with 3 µm particle size was used, and in the second step a diamond suspension with 1 µm particle size was used. The particle size of the diamond suspension influences the surface in the meaning that smaller particles makes the surface finer.

3.3 Exposure and conditions

The materials were exposed in an environment containing 5% O_2 + 95% N_2 at 600 °C in the presence of K_2CO_3. The purpose of adding K_2CO_3 was to trigger the breakdown of the primary corrosion protection to be able to study the secondary corrosion regime. A horizontal silica tube furnace was used for the exposure experiments with a specified flowrate and time.

The exposure was divided into two steps: a pre-oxidation and a second exposure after spallation. A balance called Sartorius^{TM} was used to weigh all coupon samples before the exposures. The balance have a resolution of micrograms. A solution containing water and K_2CO_3 was then sprayed on each sample side (front and backside). Warm air was used to accelerate the drying process of the deposited K_2CO_3 - solution on all samples. The samples were thereafter weighted again to be able to measure the amount of deposited K_2CO_3. This procedure was repeated continuously to reach a concentration of 1 mg/cm^2 of K_2CO_3 on each coupon, both front and backsides.

As mention before, the conditions for the exposure in the silica tub furnace were set to 600°C. The time needed for this exposure were select to be 48 hours. A Bios Definer 220M was used to calibrate the gas flow in the tub furnace to deliver a total flow rate of 2.5 cm/s. The composition of the gas was 5% O_2 and 95% N_2, as mention previously. Sample holders of alumina with three slits was used to hold the samples in a vertical direction relative to the tube furnace. After 48 hours of exposure, the samples was weighed to obtain the mass gain.

Before the second step of exposure, there were two ways to induce the spallation of the pre-formed oxide scale, either thermally or mechanically. The choice of induction method

for the spallation of the oxide scale was determined to be mechanically with grinding and polishing. After the spallation, the same procedure as for the pre-oxidation was repeated.

3.4 Analytical Techniques

In this section the analytical techniques needed for the experimental part is mentioned, motivated and briefly described.

In order to prepare cross sections of each sample, a thin silicon wafer was attached with glue on the surface. The glue was left to dry for approximately 24 hours. Afterwards, each sample was cut by a low speed diamond saw and milled by using broad ion beam (BIB) with a Leica TIC 3X instrument to obtain a smooth surface for more accurate analysis. The ion beam (3 argon guns) was operated for 4 hours with 8 kV. Further on, scanning electron microscopy (SEM) was used to analyze the cross sections of the resulting oxide scales.

The cross section of the oxide scales formed on the exposed sample was analysed by using scanning electron microscopy (SEM) and energy dispersive X-ray (EDX). The scanning electron microscopy was performed with an accelerating voltage of 10-20 kV using an FEI Quanta 200 equipped with an Oxford Instruments X-MaxN 80 T EDX detector. For the imaging backscattered electron (BSE) modes were used.

3.4.1 Scanning Electron Microscopy (SEM)

Scanning Electron Microscopy (SEM) is suitable to use because it provides information of the chemical composition and surface morphology of a sample. There exist different types of SEM setups, but the main components are the following: electron source, column for the electrons to travel, electron detector, sample chamber, computer and a display. The conventional working principle of SEM is that the sample surface is hit/scanned by a beam consisting of high-energy electrons (primary electrons). When these electrons scan the surface, it will penetrate the sample and give rise to different signals to detect. These signals are secondary electrons (SE), backscattered electrons (BSE), and characteristic X-rays [35, 36]. The different type of signals are emitted from different depths and interaction volumes that depends on the sample and the accelerating voltage (the voltage applied to accelerate the primary electrons), see Figure 3.1. Thus, the electrons will penetrate more deeply into the sample when increasing the voltage (energy) [37]. The backscattered electrons have high energy and can thus escape from a greater depth whereas the secondary electrons with a lower energy can only escape from a smaller volume near the surface. Consequently, the signals from BSEs will have lower spatial resolution than those from BEs [38].

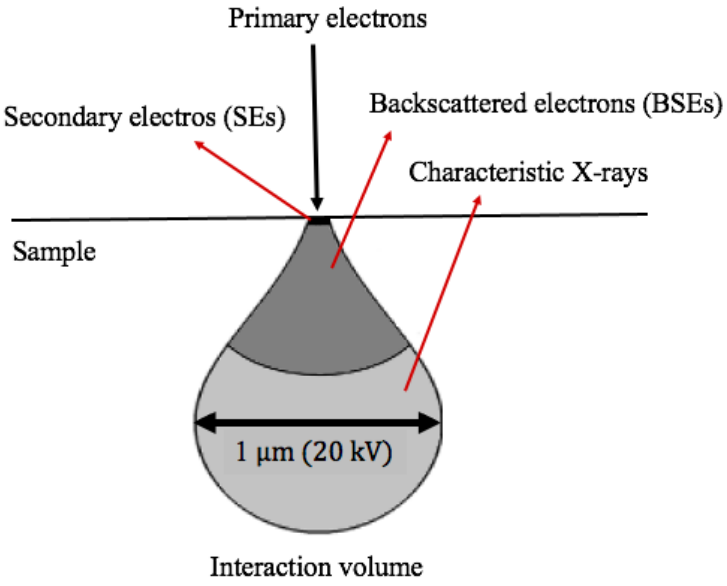

Figure 3.1: *Illustration of the interaction volume at different depths that generate different signals. The interaction volume in the figure is 1* µm *at 20 kV but the size can be varied dependent on the applied voltage [19].*

Detectors are used to collect these types of signals to create an image of the sample surface. The image is displayed on a computer screen [35, 36]. For a sample to be measured in SEM there are requirements that must be fulfilled. The sample needs to be conductive, and if the sample is non-conductive it can be measured in SEM if a thin layer of graphitic carbon or gold is coated on the sample. There are other types of conductive material for a non-conductive material to be coated with but gold and graphitic carbon are the most common. Another requirement is that the sample needs to be imaged in vacuum for conventional SEM [36].

3.4.2 Energy Dispersive X-ray Spectroscopy (EDX)

Energy Dispersive X-ray spectroscopy (EDX) can be used for chemical analysis and can be used in combination with SEM. EDX is an analytical technique based on the interaction of electron with the atom. The chemical composition can be obtained by bombarding the sample with SEM's electron beam. The electrons will be ejected from the atoms which are then filled with electron of higher state. To balance the energy, a characteristic x-ray is therefore emitted and can be detected by a EDX detector. Data obtained from EDX is presented as a spectra with peaks that corresponds to specific elements. Both quantitative and qualitative analysis are possible when using EDX. Elemental mapping is also possible where the intensity of characteristic x-ray is measured relative to lateral position on the surface [39].

4

Results & Discussion

In this section the results from the literature review and the experimental parts are presented/ compiled. Regarding the literature review the ambition and goal was to collect data for Fe-based alloys in the temperature range 400-850 °C and evaluate parameters such as, microstructure, behaviour, exposure time/cycles, mass gain, spallation, thickness, growth rate, types of oxides and corrosion regimes in different environments. However, the main part of the literature review was to investigate the applicability of the concept introduced by Persdotter et al. [1] about the secondary corrosion protection, in a broader temperature range and in varying environmental conditions. For the experimental part, 4 different alloys were investigated and the purpose of this practical work was to see if the spallation of a previously formed secondary protection affect the corrosion resistance of a new secondary protection.

4.1 Literature review

As mentioned in the introduction section, investigations regarding the protective properties of the oxide formed in the secondary corrosion regime are scarce. Examples of studies that have been investigating the oxides formed after breakaway at 600 °C in various environments are by Jonsson et al. [6, 7, 8], Pujilaksono et al. [9] and Petterson et al. [40]. These studies showed that the oxide scales formed in the secondary corrosion regime at 600 °C have similar microstructures (multi-layered Fe-rich oxide), despite the different environments and exposure conditions. Thus, it was suggested by Jonsson et al. [7] that the microstructures was governed by a diffusion controlled process. This is explained by the different diffusivities of cations in the spinel. The Cr^{3+} ions diffuse much slower than Fe^{2+} and O^{2-} in the spinel which explain why the outward-growing oxide scales are composed of almost pure Fe oxide (hematite/magnetite), whereas the inward-growing spinel composed of other alloying elements (with lower diffusivity than Fe) such as Cr and Al/Ni but also Fe. However, the species that are used to induce breakaway (e.g. water vapor or alkali salts) may influence the rate of oxidation as well as the microstructure of the inward-growing oxide after breakaway.

The oxide scale formed after breakaway behave differently for different Fe-based alloys and has been studied by Persdotter et al. [1]. The study investigated the protective properties of the oxides formed after breakaway by altering the composition of the alloys.

The study showed that the model alloys in the secondary regime displayed two different behaviors, fast and slow oxide scale growth. The results showed that the addition of Ni or a combination of Al/Cr influence the growth rate for some alloys but not for others. The results also suggested that the growth rate in the secondary regime at 600 °C is mostly diffusion-controlled. Therefore, simplified and generalized modeling tools that are used for various Fe-based alloys at 600 °C can also be used to model the oxide growth after breakaway (i.e. in secondary corrosion regime).

The aim of this thesis work was to investigate the applicability of the concept of primary and secondary corrosion regimes but mostly how the protective properties varies in the secondary corrosion regime. To investigate if the concept still holds with the data obtained from other authors/researchers and at different temperatures and environments. Thus, data from different authors and researchers has been collected and compared. Data from 21 different articles were collected and are tabulated in Appendix A. However only a few of these articles were evaluated. The reason is, among other things, too different parameters (composition, environments and exposure times) and hence difficult to compare and find any trend. The initial plan was to compare the growth rate of various Fe-based alloys collected from the articles but there were no SEM images for some of the articles to be measured. The collected data from the different articles will therefore mainly be evaluate by means of mass gain data since it give information about the oxidation rates and behavior. If possible, the combination of mass gain data and SEM images will be used. Moreover, note that the graphs that are presented in this section are re-created (using different trend lines) from the articles and thus can slightly differ from the original.

4.1.1 FeCr Alloys

This subsection summarize the observation from the collected data by different authors/researchers for Fe-Cr (ferritic) alloys in various environmental conditions and at different temperatures. The first set of data (by Cao et al. [41] and Ma et al. [42]) will investigate the secondary corrosion protection during isothermal oxidation, whereas the second set will include the effect of cyclic oxidation

Figure 4.1 show the collected data from Cao et al. [41] in which they investigated the effect of NaCl on the high temperature corrosion at 600 °C. The mass gain data clearly showed that the primary protection of the alloys rapidly broke down and had entered the secondary corrosion regime as in good agreement with previous studies. Alkali- and chlorine containing species generally have the ability to accelerate the growth rate of the produced oxide layer [40, 43, 32]. Both mass gain curves in Figure 4.1 were similar despite the different environmental conditions. However, the thickness of the oxides differ significantly. In the case with NaCl solution spray (NaCl particles and water vapor in

the air) a more compact oxide was formed with a measured thickness of 53 µm (29 outer and 24 inner layer), which consisted of hematite (Fe_2O_3), chromite ($FeCr_2O_4$) and a small amount of Cl distributed throughout the oxide. In solid NaCl deposit with water vapor, a thicker and more porous oxide scale was formed with the measured thickness of 85 µm, consisted of Fe_2O_3, $FeCr_2O_4$, Cr_2O_3, Na_2CrO_4 and residual NaCl, see Figure 4.2. The last mentioned oxides thickness (85 µm) was however not in agreement with the mass gain data with the calculated thickness (using equations in Appendix B) around 40 µm. Additionally, the thickness for Fe-20Cr in NaCl solution spray was also in disagreement with the calculated thickness, 53 µm compared to 43 µm. The calculations were based on the assumption that the oxide scale is dense and uniform which consist of only one iron oxide, in this case hematite. The formed oxide scales are usually not uniform and consist of different oxides. This may be the explanation why the measured and the calculated oxide thickness differs. Nevertheless, the microstructure of the oxide formed in both conditions are similar to those with an outward-growing Fe-rich oxide and inward-growing mixed spinel even though the one formed in the presence of solid NaCl was more damaged. The differences in the thickness may be influenced by the different form of the salt, but the synergistic effect of NaCl and water vapor may be the main reason. In addition, the direct contact between the solid NaCl and the metal may be one of the reasons. It have been observed by Jonsson et al. [33] that local oxide growth was rapid on the parts of the surface where there was a direct contact between the metal and salt. Also, it is suggested by several studies that the presence of water vapor promotes the formation of a more porous oxide scale [44].

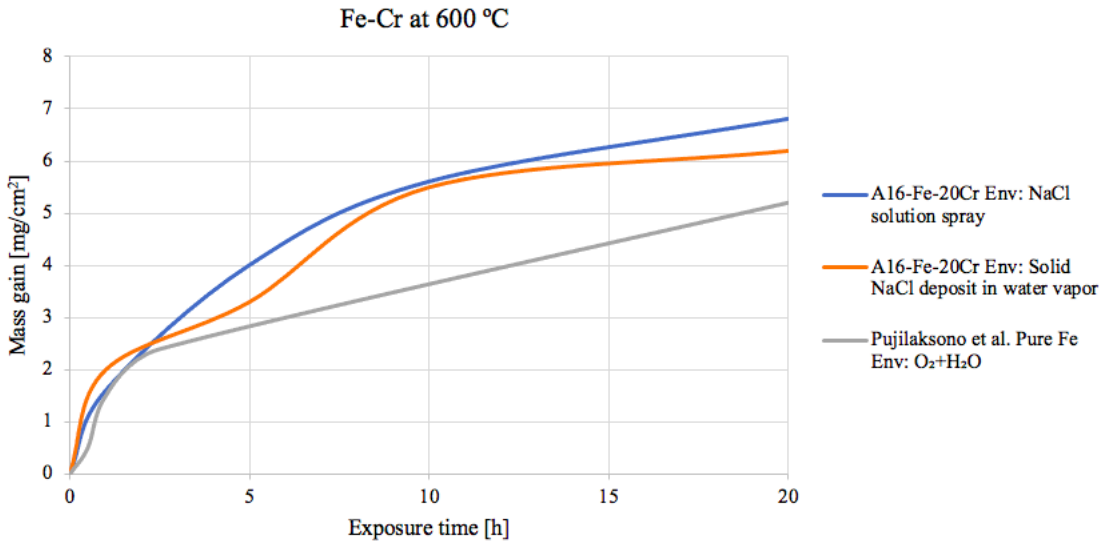

Figure 4.1: *Mass gain versus exposure time for Fe-20Cr exposed at 600 °C in NaCl solution spray and solid NaCl deposit in water vapor. The data are collected from Cao et al. [41]. Mass gain data obtained from Pujilaksono et al. [45] for pure Fe is also shown in the graph.*

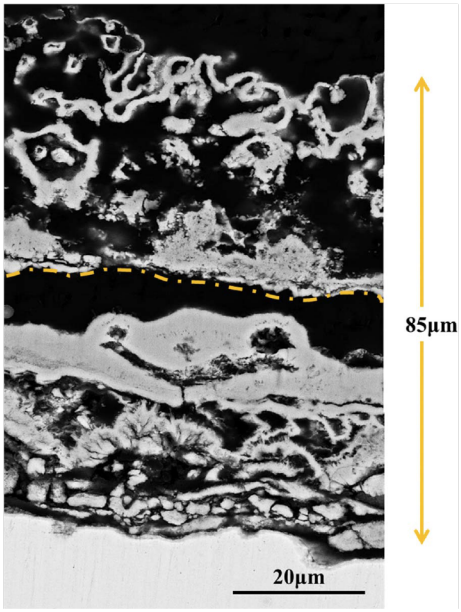

Figure 4.2: *Cross section of the oxide scale formed on Fe-20Cr after 20 h exposure in solid NaCl deposited in water vapor environment at 600 °C. Image from Cao et al. [41].*

Figure 4.1 indicated that NaCl-induced corrosion in the presence or absence of water vapor formed different oxide thickness as a result of the influence of the corrosive species (e.g. Na or Cl) and water vapor. Though the oxide formed in NaCl solution spray was thinner and more compact than the one in NaCl solid in water vapor, the kinetics at 600 °C were similar (fast-growing) which indicated that Fe-20Cr in both environment displayed a poor secondary corrosion protection.

Moreover, an important parameter in high temperature corrosion is of course the influence of the temperature. At elevated temperatures, the behavior of Fe-based alloys may not be the same as at lower temperatures. As discussed preciously, Fe-20Cr in presence of NaCl and the presence and absence of water vapor displayed a poor secondary corrosion protection at 600 °C. There were no data available with identical environmental parameters to be compared with at higher temperatures. The most similar was the exposure in O_2 containing 298 ppm KCl vapor by Ma et al. [42]. Studies have shown that KCl is equally corrosive as NaCl in water vapor to stainless steel and FeCrAl alloys at intermediately high temperatures [46, 47]. Thus, the data collected from Ma et al. [42] is relevant to compare to those obtained from Cao et al. [41].

Figure 4.3 show the collected data from Ma et al. [42]. As can be seen, pure Fe has the highest mass gain whereas there were no big difference in mass gain for Fe-20Cr and Fe-40Cr but the former has higher final mass gain. Thus, in comparison to oxide formed on pure Fe, the growth rate of oxide formed on Fe-20Cr and Fe-40Cr is much slower and the mass gain seems to stabilize at 4 mg/cm^2 after 8 hours. The cross sections for Fe-20Cr

and Fe-40Cr can be seen in Figure 4.4. Buckling and multilayers of the oxides scales can be observed for both Fe-20Cr and Fe-40Cr. This observation is similar to the Fe-20Cr in Figure 4.2 by Cao et al. [41].

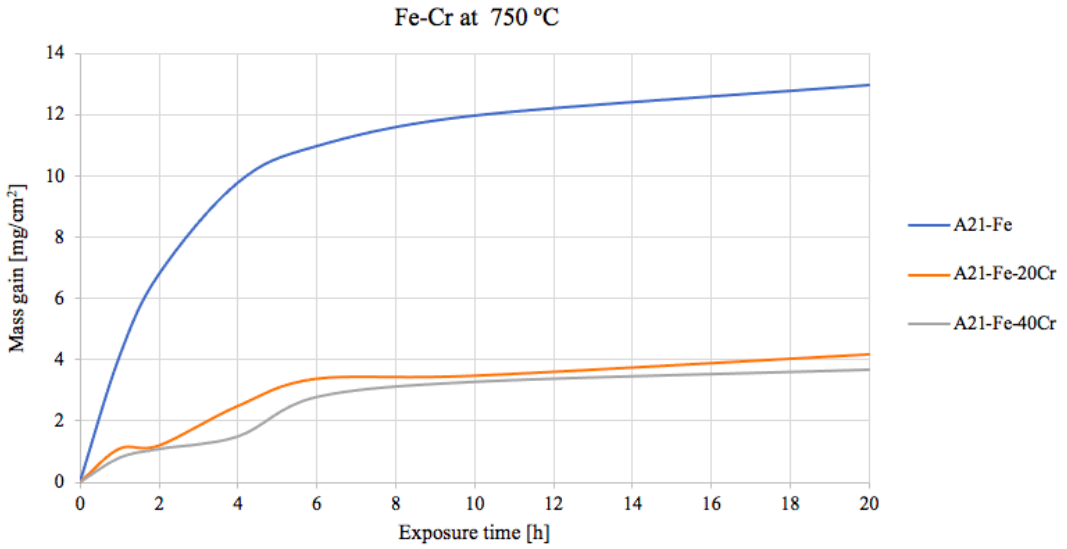

Figure 4.3: *Mass gain versus exposure time for pure Fe, Fe-20Cr and Fe-40Cr exposed at 750 °C in O_2 containing 298 ppm KCl. The data are collected from Ma et al. [42].*

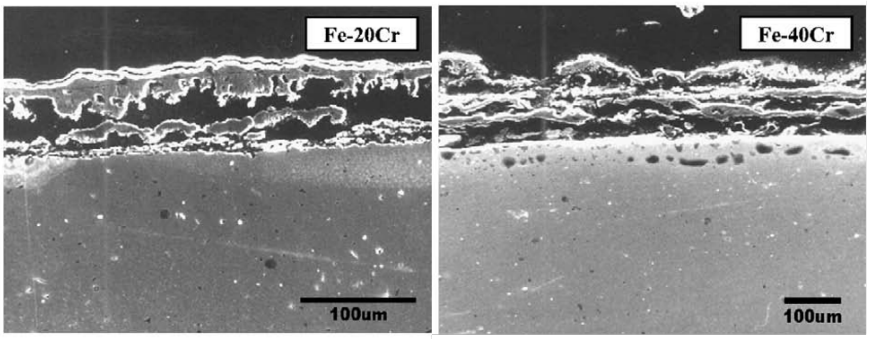

Figure 4.4: *Cross section of the oxide scale formed on Fe-20Cr and Fe-40Cr after 20 h exposure in O_2 containing 298 ppm KCl at 750 °C. Image from Ma et al. [42].*

The mass gain for Fe-20Cr from Figure 4.3 was ∼4 mg/cm^2 in comparison to ∼6 mg/cm^2 and ∼7 mg/cm^2 from Figure 4.1 which is summarized in Table 4.1. The comparison between these two studies suggested that the growth rate for Fe-20Cr decreased when increasing the temperature from 600 to 750 °C. Thus, at 600°C, 20 wt% Cr is not sufficient to form a good corrosion protection while at 750 °C, a good secondary protection could be obtained. This observation is interesting because higher temperature would increase the diffusion rate and thus the growth rate. For pure Fe at 600 °C (see Figure 4.1), the final mass gain is ∼5 mg/cm^2 [45] in comparison to at 750 °C with the final mass gain ∼13 mg/cm^2. Note that the environments for pure Fe at 600 °C is from a study by

Pujilaksono et al. [45] and in water vapor containing environment which is not the same environment as for pure Fe exposed at 750 °C. Nevertheless, this clearly shows that the higher temperature increases the growth rate of pure Fe. In contrast, for Fe-20Cr, higher temperature decrease the growth rate. One reasonable explanation is the formation of a healing layer which is a layer at the metal/oxide interface (beneath the iron oxides) that is Cr-rich or Al-rich. These layers will act as a diffusion barrier because the diffusion through them is slower than through iron oxide. There are two criteria that needs to be fulfilled for a healing layer to form; sufficient Cr content at the metal/oxide interface and the formation of the healing layer has to be faster than the growth rate of the Fe-rich oxides [19]. From the collected data by Cao et al. [41] and Ma et al. [42], it was suggested that at 750 degrees, the diffusion of chromium to the metal/oxide interface is faster than at 600 °C and thereby is able to form a healing layer faster. However, this observation should be treated with caution since more detailed microstructural analysis is needed to support this observation. In addition, the assumption about NaCl being as corrosive as KCl may not be valid at higher temperatures than 600 °C. Also, it has been showed that there are some differences between these two salts such as corrosion behavior and internal degradation [47].

Table 4.1: *Mass gains for Fe-20Cr alloys from Cao et al. [41] and Ma et al. [42].*

Ref.	*Alloy*	*Temperature [°C]*	*Mass gain [mg/cm^2]*
[41]	Fe-20Cr	600	∼6*
[41]	Fe-20Cr	600	∼7(*)
[42]	Fe-20Cr	750	∼4

* Solid NaCl deposit in water vapor and (*) NaCl solution spray

Until now, the discussion has been focused on the secondary corrosion protection of Fe-Cr alloys at different temperatures when isothermally exposed. It would also be of interest to see how the corrosion rates will be affected at different temperatures during cyclic oxidation. This is of interest because the alloys used in many application are subjected to thermal cycling, where the boilers for instance have to be turn on and off to reduce maintenance costs.

The collected data from Othman et al. [48] presented in Figure 4.5 and 4.9 covers the factor of interest. Figure 4.5 present the mass gain data as a function of number of cycles up to 400 cycles. The Fe-based alloys in varying amount of Cr (9, 17 and 25%), were exposed at 600 °C in two different environments, in O_2 and O_2 + H_2O. It can be observed from the figure that higher chromium content decelerated the growth rate in both environments

although the growth rates were higher in the presence of water vapor. The Fe-9Cr in both environment behave similarly (fast-growing) but the environment with water vapor have higher mass gain (16 mg/cm^2 compared to 10 mg/cm^2). Similarly, the presence of water vapor also accelerated the growth rate of Fe-17Cr, where in air, it has an incubation time of 40 cycles. However, Fe-17Cr exposed in the presence and absence of water vapor at 600 °C has lower mass gain than Fe-9Cr in the corresponding environments. Thus, the transition into a more slow-growing behavior, the Cr content must be higher than 17% in air. With the data obtained from this study, in presence of water vapor at 600 °C, all the alloys displayed a poor secondary protection. Additionally, it is worth to mention that Fe-25Cr (with 40 cycles incubation time) displayed the slowest growth in O_2 but in presence of water vapor, the sample remained in the primary corrosion regime and is thus not showed in Figure 4.5.

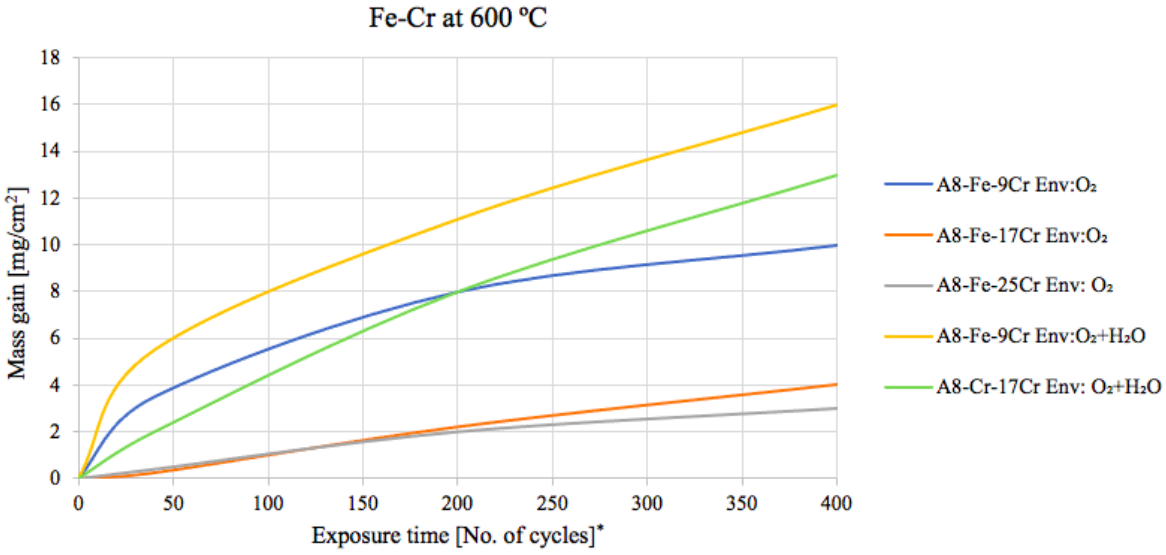

Figure 4.5: *Mass gain as a function of number of cycles for Fe-Cr alloys in O_2 and Ar-20O_2-5H_2O (vol.%) at 600 °C. *The cycles followed a schedule of 1h exposure and then 10 min cooling time to around 80 °C between the cycles. The data are collected from Othman et al. [48].*

A study that investigated Fe-Cr alloys in varying amounts of Cr at 600 °C in similar environments as Othman et al. [48] was performed by Pujilaksono et al. [9]. In the study, four Fe-based alloys (Fe-2.25Cr, Fe-10Cr, Fe-18Cr and Fe-25Cr) were isothermally exposed in air and in presence and absence of water vapor. The result indicated that water vapor accelerated the corrosion rate of those Fe-Cr alloys and thus displayed higher mass gain. The study proposed that the breakaway oxidation in wet O_2 was triggered by the evaporation of $CrO_2(OH)_2$. Thus, the chromium evaporation depletes the oxide and when the supply of Cr is insufficient, the breakaway oxidation occurs [49]. Moreover, the Fe-based alloys with 10-25 wt% Cr exposed in air remained in the primary corrosion

regime which is not in agreement with the obtained data from Othman et al. [48]. A reason could be that the exposures were carried out differently. Isothermal oxidation exposures in the case of Pujilaksono et al. [9] while Othman et al. [48] performed cyclic oxidation. The rapid change in temperature induces stresses in the oxide scale as a result of the different thermal expansion coefficients of alloys and oxide. This stress may cause cracks in the oxide scale or spallation of the entire or part of the oxide scale which leads to the alloy surface being exposed to the surrounding atmosphere that accelerate the growth even further [50]. Another disagreement was that Fe-25Cr did not breakdown in presence of water vapor at 600 °C by Othman et al. [48] but it did in the study by Pujilaksono et al. [9]. A possible explanation may be that the study by Pujilaksono et al. [9] used more water vapor (40% compared to 5% water vapor). However, there were nodules on the surface at 600 °C in water vapor which indicated a sign of breakaway corrosion, see Figure 4.7b.

It should also be mentioned that the Fe-17Cr exposed in O_2 in Figure 4.5 and 4.6 went into breakaway but the Fe-rich oxide formed was not continuous which indicated that the breakdown was not fully complete. As can be seen from the Figure 4.6, some parts of oxide had developed a Fe-rich oxide while some parts (not shown) may not. The gap that separated the different oxide layer may be the consequence of the thermal stress. For Fe-25Cr, the breakdown in O_2 was more complete than for Fe-17Cr, with approximately uniform oxide scale as shown in Figure 4.7. This result may suggest that Fe-17Cr was more resistance to breakaway corrosion in comparison to Fe-25Cr when expose in O_2 under cyclic conditions. However, due to the scarcity of data to compare with, coupled with the fact that Fe-25Cr did break down in air but not in presence of water vapor contradicted the previous studies, this observation should be treated with caution.

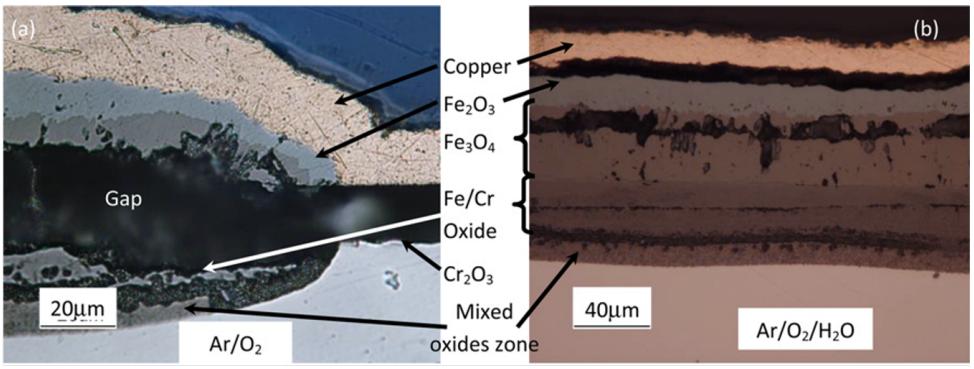

Figure 4.6: *Cross section of the oxide scale formed on Fe-17Cr after 400 cycles exposure in a) O_2 and b) $O_2 + H_2O$ at 600 °C. The data are collected from Othman et al. [48].*

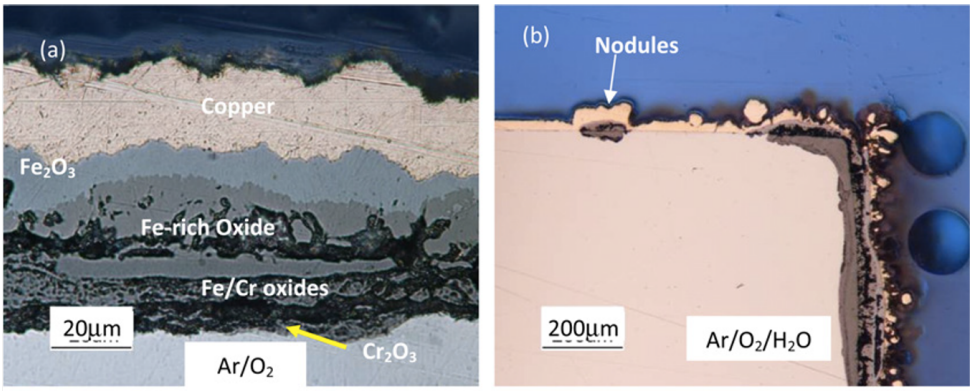

Figure 4.7: *Cross section of the oxide scale formed on Fe-25Cr after 400 cycles exposure in a) O_2 and b) $O_2 + H_2O$ at 600 °C. The data are collected from Othman et al. [48].*

At higher temperature, at 650 °C, it was observed that the effect of thermal cycling increased the growth rate of Fe-Cr alloys, see Figure 4.5 and 4.8. Figure 4.8 present the mass gain data as a function of cycles for Fe-Cr alloys with varying amount of chromium content 10-20 wt% , collected from a study by Peraldi et al. [51]. The environment condition is similar to the previous one in presence of water vapor (air + 10% water vapor) but here the exposure is up to 100 cycles. It can be observed that higher Cr contents (Cr >18 wt%) delayed the breakaway corrosion by 20 cycles. However, after breakaway corrosion, all alloys displayed a fast-growing behavior but the growth rate decreased with increasing Cr contents as previously been observed from Figure 4.5.

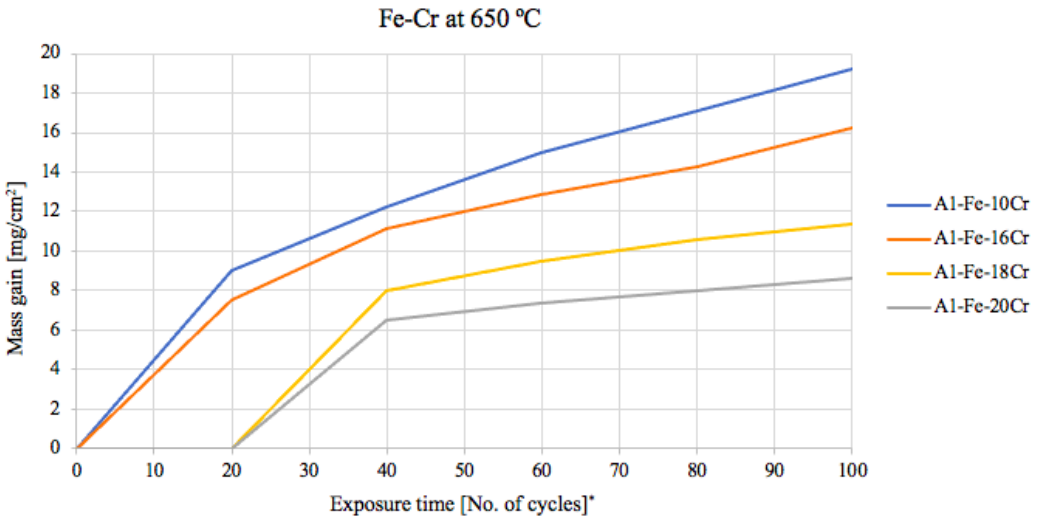

Figure 4.8: *Mass gain as a function of cycle-time for Fe-Cr alloys in the environment containing air and 10 % water vapor at 650 °C. *The cycles followed a schedule of 1h exposure and then 10 min cooling time to around 30 °C between the cycles. The data are collected from Peraldi et al. [51].*

Increasing the temperature to 700 °C also increased the growth rates of Fe-Cr alloys, see Figure 4.9. After 180 cycles, the mass gain for Fe-9Cr reached 41 mg/cm^2 in O_2, whereas in presence of water vapor the mass gain was lower (39 mg/cm^2 after 260 cycles). For Fe-17Cr in O_2 + H_2O, the mass gain was the lowest with the value of 30 mg/cm^2. Moreover, all the alloys in Figure 4.9 displayed high oxidation rates despite the presence or absence of water vapor. However, the initial oxidation rate of Fe-9Cr in O_2 was slower until 100 cycles where it grow faster than the other alloys exposed in the presence of water vapor. For Fe-9Cr and Fe-17Cr in presence of water vapor, it can be observed that, after 50 cycles both follow a linear kinetic meaning that these are not diffusion controlled. This can be explained by crack formation that provide the direct contact between gas and metal and thus following a linear kinetic behavior. Moreover, at 700 °C, Fe-17Cr and Fe-25Cr did not break down in air. In presence of water vapor, Fe-17Cr did break down but not Fe-25Cr. Nevertheless, this clearly showed that the corrosion rate is accelerated at elevated temperature in both environments and for all the alloys that had entered the secondary corrosion regime.

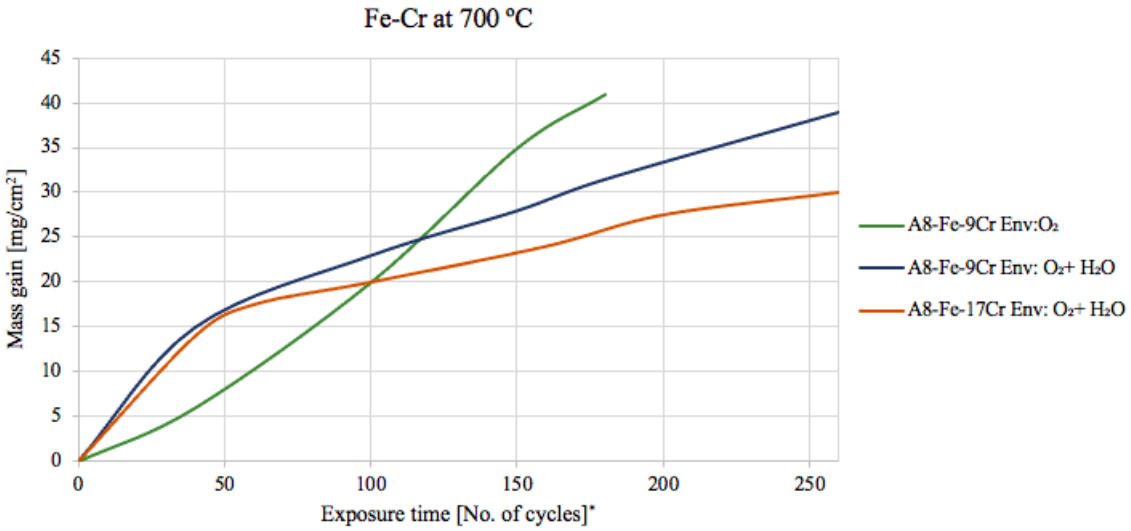

Figure 4.9: *Mass gain as a function of number of cycles for Fe-Cr alloys in O_2 and Ar-20O_2-5H_2O (vol.%) at 700 °C. *The cycles followed a schedule of 1h exposure and then 10 min cooling time to around 80 °C between the cycles. The data are collected from Othman et al. [48].*

The last temperature and also the highest, is at 800 °C, the data is presented in Figure 4.10. In Figure 4.10, the mass gain at 800 °C only present for Fe-10Cr and Fe-14Cr. Fe-16Cr, Fe-18Cr and Fe-20Cr did not break down and thus not shown here. This indicated that Fe-Cr with higher than 16wt% Cr remained in the primary corrosion regime. As can be observed from the graph, Fe-10Cr and Fe-14Cr have similar final mass gain but displayed different behavior. For Fe-9Cr is more parabolic while for Fe-14Cr is almost linear. However, both show no sign for stabilization. Again, this can be explained by the formation of crack in the oxide scales which restores the contact between the metal and the oxidizing atmosphere. Nevertheless, the growth rates were significantly enhanced at 800 °C in comparison to at lower temperatures for the alloys that have entered the secondary corrosion regime.

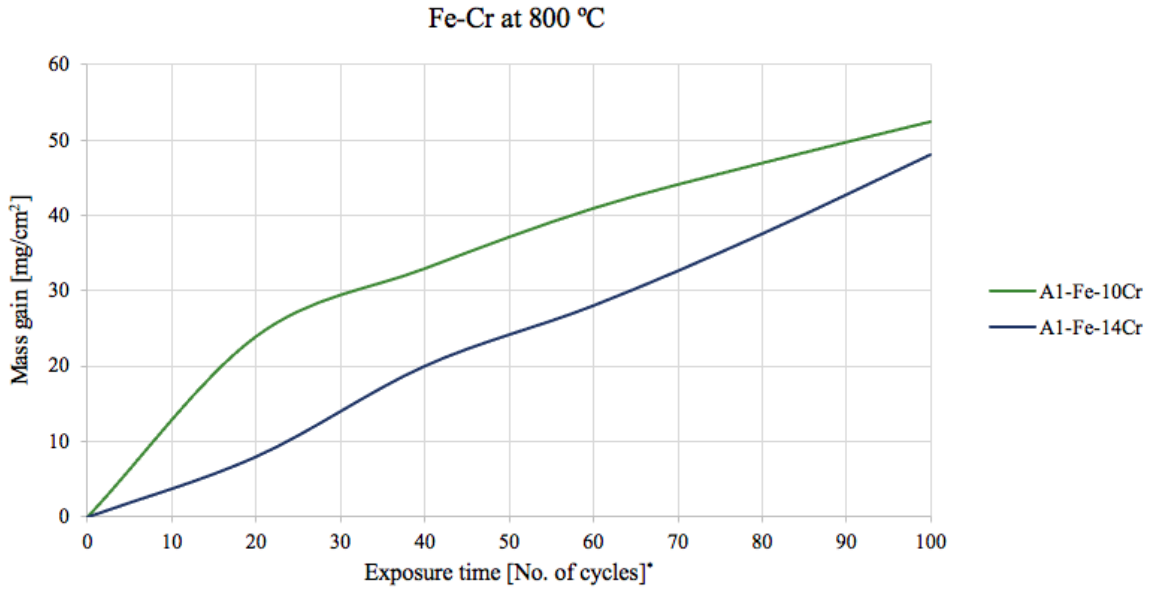

Figure 4.10: *Mass gain as a function of cycle-time for Fe-Cr alloys in the environment containing air and 10 % water vapor at 800 °C. *The cycles followed a schedule of 1h exposure and then 10 min cooling time to around 30 °C between the cycles. The data are collected from Peraldi et al. [51].*

Overall, higher temperatures will accelerate the growth rates for those alloys that have entered the secondary corrosion regime when exposed in cyclic conditions, as summarized in Table 4.2 and 4.3. This suggest that the effect of cyclic oxidation is more severe at elevated temperature. As mentioned before, the thermal stresses induced in the oxide scales is the result of the difference in thermal expansion coefficients of the alloys and the oxide when heating and cooling. Thus, if the difference in thermal expansion coefficient is large, then compressive stresses will be induced in the oxide scales when cooling [2, 44]. Higher exposure temperature leads to higher temperature differences, in this case, from 800 °C to 30° when cooling. This may be a possible explanation to why the growth rates are higher and no sign of stabilization at elevated temperature, because of the rapid temperature change from the high exposure temperature to the cooling temperature that may result in higher level of thermal stresses. When stresses are induced in the scale, cracks formation may result. The oxygen can thus enter through the cracks and directly react with the metal which results in a linear kinetic growth.

A sidenote, which is also interesting, both data from Othman et al. [48] and Peraldi et al. [51] shows that at lower temperature (i.e. 600 °C), around 20 wt% Cr could not form a protective oxide scale but at 800 °C, 16wt% Cr was sufficient for retaining the primary corrosion protection in presence of water vapor. A possible explanation may be the faster diffusion of chromium. Increasing the temperatures will facilitate the supply of chromium to the surface, thereby retaining chromia scale growth [48].

To summarize, the investigation on the effect of cyclic oxidation suggest that Fe-Cr alloys that have a good secondary protection or even a primary corrosion protection during isothermal oxidation, will not have the same protective properties when exposed in cyclic conditions of temepratures. The effect of cyclic oxidation was shown to be more severe at higher temperatures due to crack formation. In addition, all of the Fe-Cr ferritic alloys exposed in the presence or absence of water vapor during cyclic oxidation at 600-800 °C showed to form poor secondary corrosion protections. However, all Fe-Cr alloys showed not to spall off even though it could be observed that the formed oxide scale were damaged with cracks and buckling.

Table 4.2: *Comparison of mass gain for Fe-9Cr/Fe-10Cr at various temperatures in similar environments containing water vapor during cyclic oxidation up to 100 cycles. The data are collected from Othman et al. [48] and Peraldi et al. [51].*

Ref.	*Alloy*	*Temperature [°C]*	*Mass gain [mg/cm^2]*
[48]	Fe-9Cr	600	8
[51]	Fe-10Cr	650	19
[48]	Fe-9Cr	700	23
[51]	Fe-10Cr	800	52

Table 4.3: *Comparison of mass gain for Fe-16Cr/Fe-17Cr at various temperatures in similar environments containing water vapor during cyclic oxidation up to 100 cycles. The data are collected from Othmna et al. [48] and Peraldi et al. [51].*

Ref.	*Alloy*	*Temperature [°C]*	*Mass gain [mg/cm^2]*
[48]	Fe-17Cr	600	5
[51]	Fe-16Cr	650	16
[48]	Fe-17Cr	700	20
[51]	Fe-14Cr	800	48

4.1.2 FeCrNi Alloys

To evaluate different alloys and put this into a broader perspective not only Fe-based alloys containing varying amounts of chromium was investigated. In Figure 4.11 and 4.12 one can see how the content of nickel influences the mass gain as a function of cycle time. As a result, these two graphs clearly show that the presence of Ni caused spallation of the formed oxide scales of mostly all the alloys. The risk of spallation may be due to thermal expansion between the layers of the metal and the oxide. Depending on the model alloy, the degree of thermal expansion is varying and examples of coefficients for thermal expansion of metal/alloys and their corresponding oxide are shown in Table 4.4 [2].

Table 4.4: *Examples of thermal coefficients for the systems (metal/oxide) Fe/FeO, Fe/Fe_2O_3, Ni/NiO, Cr/Cr_2O_3, Sanicro® 28 and Sandvik 4C54 [2, 52, 53].*

Ref.	*Metal/oxide*	*Metal coefficient ($\times 10^{-6}$)*	*Oxide coefficient ($\times 10^{-6}$)*
[2]	Fe/FeO	15.3	12.2
[2]	Fe/Fe_2O_3	15.3	14.9
[2]	Ni/NiO	17.6	17.1
[2]	Cr/Cr_2O_3	9.5	7.3
[52]	Sanicro® 28	∼17	-
[53]	Sandvik 4C54	∼13	-

From Table 4.4 one can see that the system Ni/NiO have higher thermal coefficients (metal) than Fe/FeO, Fe/Fe_2O_3 and Cr/Cr_2O_3 [2]. However, in this thesis mostly ferritic and austenitic alloys had been evaluated and this means that the value for pure Ni in Table 4.4 may not be in agreement of austenite since austenite contain more than just Ni. An alloy, containing more than 10 wt% Ni are usually austenitic while Fe-Cr alloys are ferritic. Moreover, studies have shown that austenitic materials have higher thermal expansion than ferritic materials [54, 55]. One example of an austenitic steel is Sanicro® 28 and that typical alloy have a thermal expansion coefficient ∼17, which is relatively similar to pure Ni [52]. In Table 4.4 one can also see an example of a ferritic steel, called Sandvik 4C54 and have a thermal expansion coefficient ∼13, which is relatively close to pure iron [53]. From Table 4.4 it also seems true that the coefficients of thermal expansion of ferrite and iron oxide differ much less than austenite and iron oxide. A higher difference in the coefficient of thermal expansion between the metal and the oxide leads to higher stresses in the Fe-rich oxide scale and thus the risk of spallation increases, especially in the case were cyclic oxidation occurs, as in the case in Figure 4.11 and 4.12 showed.

Furthermore, in Figure 4.11 one can also see a trend when comparing the Fe-16Cr-10Ni, Fe-16Cr-15Ni and Fe-16Cr-20Ni. The observed trend between those 3 alloys with the same Cr content but with varying Ni content is that when the Ni content increases, it seems to delay the spallation event. This delay can be a reason for why the Fe-16Cr-20Ni don't show spallation in Figure 4.11 yet and that one can predict that the oxide scale will show a spallation behavior if the cycle time had proceeded. Moreover, the spallation behavior seems to also be influenced by the Cr content and not only by the content of Ni. A comparision of Fe-16Cr-10Ni with Fe-18Cr-10Ni, and Fe-16Cr-15Ni with Fe-18Cr-15Ni resulting in the conclusion that the spallation occur later if the Cr content is increased while the Ni content remains the same. Overall, this leads to the conclusion that spallation occurs for Fe-Cr-Ni alloys and that the event happens earlier if both the Cr and Ni content is low and much later if both the Cr and Ni content is higher. This results was interesting since studies by Persdotter et al. [1] have evaluated the Fe-18Cr-10Ni also but in a different environment, temperature and exposure-route than Peraldi et al. [51]. The data from Figure 4.11 and 4.12 are extracted from Peraldi et al. [51]. The differences in exposure conditions are tabulated in Table 4.5 for the alloy Fe-18Cr-10Ni.

Table 4.5: *Comparision of the alloy Fe-18Cr-10Ni [1, 51].*

Ref.	*Alloy*	*Environment*	*Exposure time*	*Temperature [°C]*
[1]	Fe-18Cr-10Ni	5% O_2 + 95% N_2 + K_2CO_3(s)	48 h	600
[51]	Fe-18Cr-10Ni	Air + 10% water vapor	100 cycles	650

Despite the differences between the exposure conditions for the model alloy Fe-18Cr-10Ni, the influence of Ni showed in both studies [1, 51] that the mass gain were affected to the extent that the mass gain decreased if the Ni content increased. Persdotter et al. [1] stated also that the mass gain were almost constant if the content of Ni were >5 wt-%. This is in good agreement with Peraldi et al. [51], since the graphs in Figure 4.11 and 4.12 regarding the Fe-18Cr-10Ni shows a constant mass gain for that alloy until ∼40 cycles. The observed behavior after ∼40 cycles (spallation) can be explained by thermal stresses and thermal expansions for cyclic oxidation as discussed earlier.

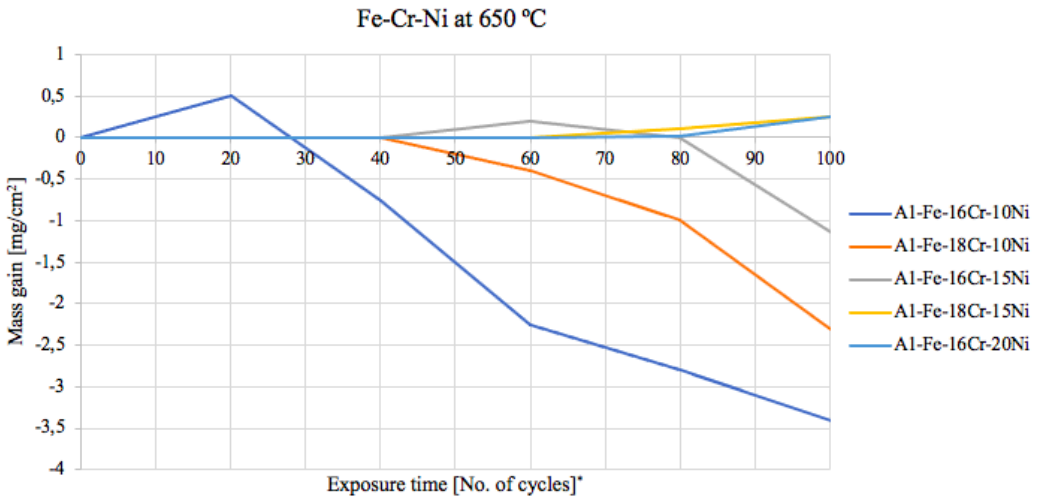

Figure 4.11: *Showing mass gain [mg/cm^2] as a function of cycle-time for Fe-Cr-Ni alloys in the environment containing air and 10 % water vapor at 650 °C. * The cycles followed a schedule of 1h exposure and then 10 min cooling time to around 30 °C between the cycles. The graph also showing the effect of varying the Ni content. The data are collected from Peraldi et al. [51].*

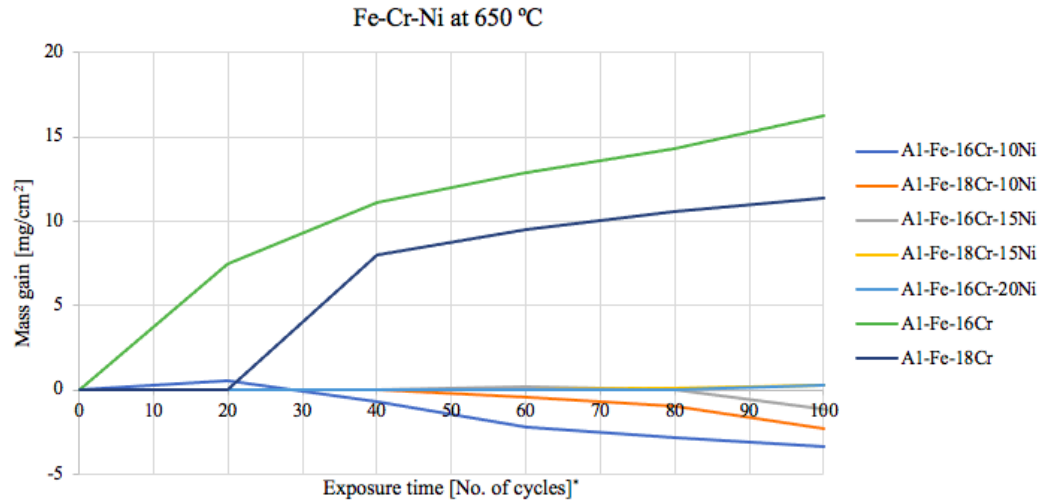

Figure 4.12: *Showing mass gain [mg/cm^2] as a function of cycle-time for Fe-Cr-Ni and Fe-Cr alloys in the environment containing air and 10 % water vapor at 650 °C. * The cycles followed a schedule of 1h exposure and then 10 min cooling time to around 30 °C between the cycles. In the graph both Fe-Cr-Ni and Fe-Cr alloys has been plotted to see the effect of varying the Ni content. The data are collected from Peraldi et al. [51].*

Another study have been done on Fe-based alloys containing Cr and Ni by Aye et al. [56]. They studied the effect of silicon on Fe-20Cr-20Ni and Fe-20Cr in different environments containing wet CO_2 with and without HCl at a temperature of 650 °C. The extracted data from Aye et al. [56] can be seen in Figure 4.13. The graph represent the mass gain [mg/cm^2] as a function of exposure time. A thing to be aware of in this graph is that isothermal exposure time had been used and means that the sample have been exposed continuously for a certain time and temperature. However, in Figure 4.13 one can easily distinguish the results of each sample. As mentioned in the theory section in this thesis, the influence of salts and Cl-ions generally have the ability to accelerate the oxidation processes on metals and alloys. Thus, alloys generally displays a higher mass gain when exposed in environments containing a higher concentration of HCl. When it comes to the influence of Ni one can also in this case see a reduced mass gain in comparison to the alloys without any Ni, even if the environment is different from the study by Peraldi et al. [51]. A notation regarding the sensitiveness of the spallation risk of Ni containing alloys is difficult to say in this case but one can predict that the risk of spallation is lower when the samples do not experience thermal cycling.

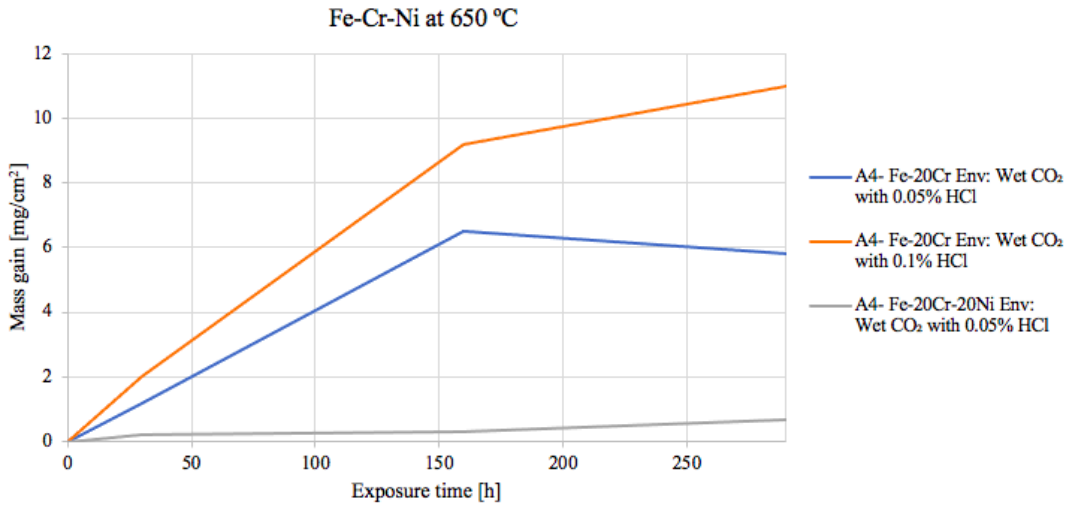

Figure 4.13: *The data obtained from Aye et al. [56] and shows mass gain as a function of exposure time at 650 °C in wet CO_2 with 2 different concentrations of HCl of the alloy Fe-20Cr, and Fe-20Cr-20Ni with 0.05 % HCl in wet CO_2.*

Moreover, earlier discussions in this thesis regarding Ni-containing alloys had been on the temperature 650 °C. To see how the influence of temperature affect Ni-containing Fe-based alloys with chromium Peraldi et al. [51] also studied alloys at 800 °C, as seen in Figures 4.14, 4.15 and 4.16.

From Figures (4.14-4.16), one can clearly observe that spallation of the oxide scales occurred already in the beginning to some extent for all the alloys in the graphs. None of these alloys in the environment with air and 10% water vapor at 800 °C showed a promising behavior of a good secondary corrosion protection. Since the protective oxide scales was immediately spalled off followed by a fast-growing oxide scales that not showed a tendency to stabilize for none of the alloys. Studies of different alloys in high temperature corrosion have shown that the influence of temperature is of importance when it comes to the rate of corrosion. This means that a higher temperature accelerate the corrosion event and thus also the occurring spallations in Figures (4.14-4.16), meaning that spallation occurs earlier at elevated temperatures when cyclic oxidation occurs.

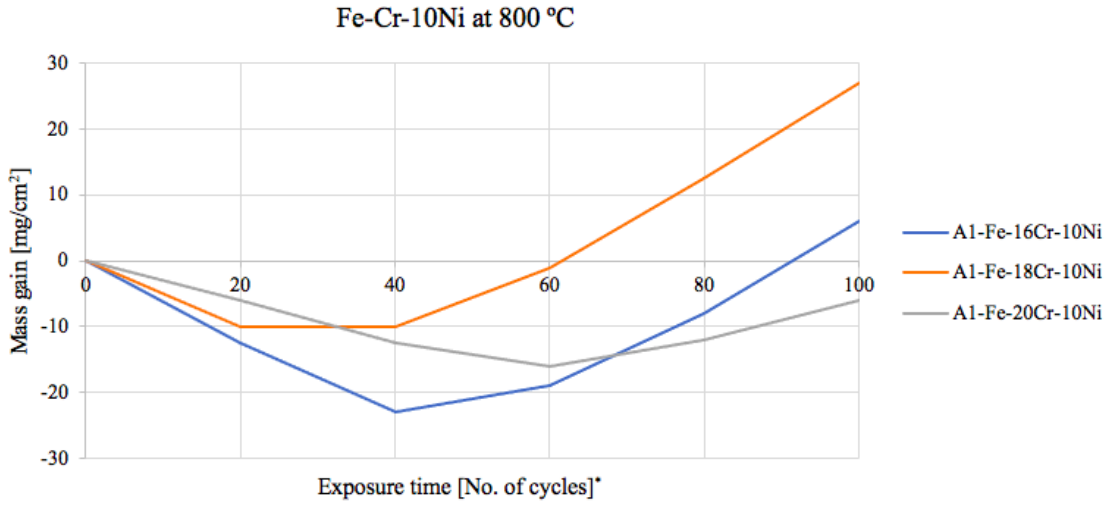

Figure 4.14: *Showing the behavior of Fe-Cr-Ni alloys at 800 °C in the environment containing air and 10 % water vapor. *The exposure was performed using cycles and 1 cycle means that the sample had been exposed for 1 hour at 800 °C followed by 10 min cooling time to a temperature of 30 °C. The data are collected from Peraldi et al. [51].*

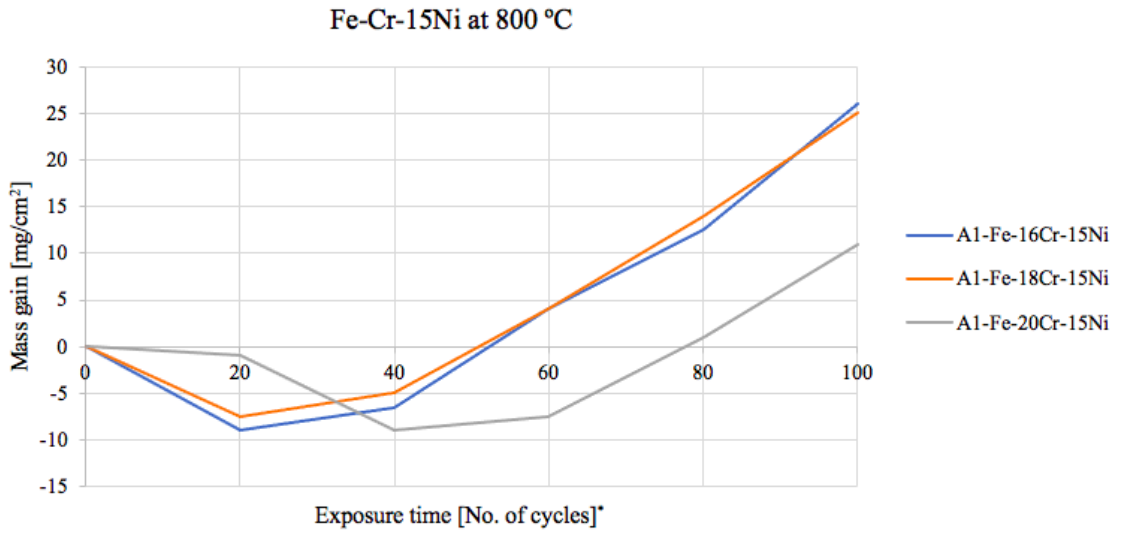

Figure 4.15: *Showing the result of mass gain as a function of cycle-time for the 3 alloys Fe-16Cr-15Ni, Fe-18Cr-15Ni and Fe-20Cr-15Ni at 800 °C in the environment with air and 10 % water vapor. *The cycles was performed by 1 hours exposure followed by 10 min cooling time to around 30 °C. The data are collected from Peraldi et al. [51].*

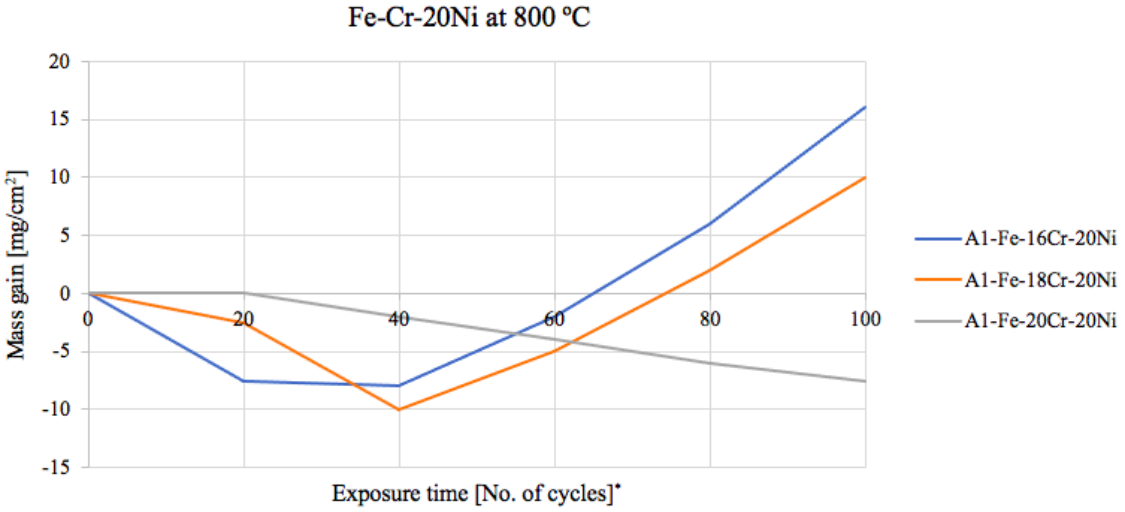

Figure 4.16: *Illustrate the result of mass gain as a function of cycle-time for the 3 alloys Fe-16Cr-20Ni, Fe-18Cr-20Ni and Fe-20Cr-20Ni at 800 °C in the environment with air and 10 % water vapor. *The cycles was performed by 1 hours exposure followed by 10 min cooling time to around 30 °C. The data are collected from Peraldi et al. [51].*

Until now in this thesis, Fe-based alloys containing nickel contents between 5-20% have been covered and discussed, but how will alloys containing lower amounts of Ni behaves? A stuby performed by Abu-Warda et al. [57] investigate the corrosion behavior of 4 steels, named AISI 304, T24, T92 and VM12 in the environment with KCl-K_2SO_4. The chemical composition of the alloys in the study by Abu-Warda et al. [57] are shown in Table 4.6.

Table 4.6: *The composition of the alloys studied by Abu-Warda et al. [57].*

Alloy	*Composition*
AISI 304	Fe-17.3Cr-8Ni
T24	Fe-2.4Cr
T92	Fe-9Cr-0.3Ni
VM12	Fe-12Cr-0.3Ni

Each alloy in Table 4.6 are plotted in the same way as the rest of the evaluated alloys in this thesis with mass gain against exposure time, see Figure 4.17.

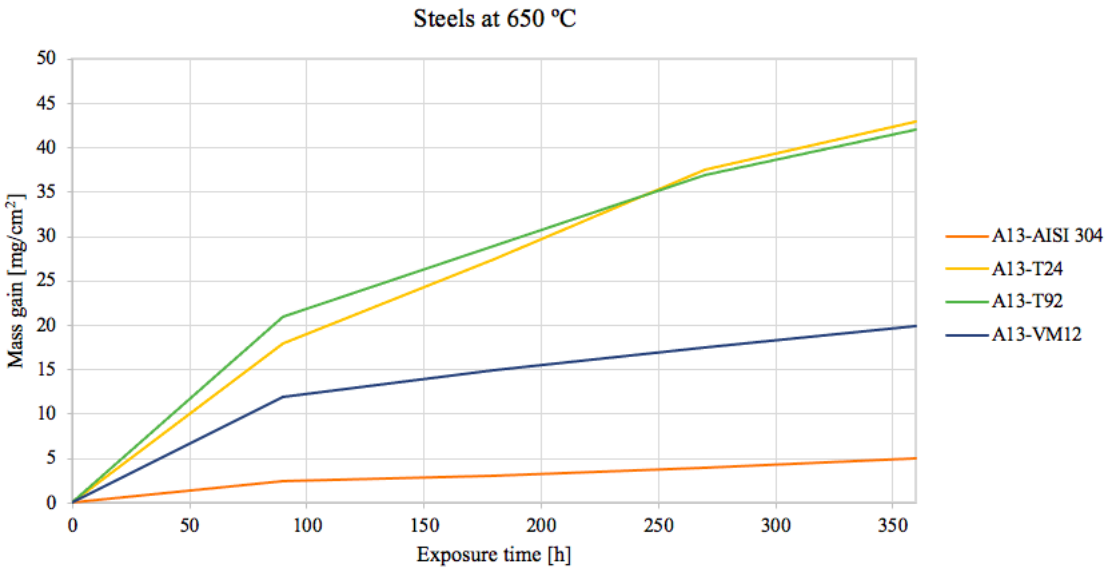

Figure 4.17: *The evaluated data from Abu-Warda et al. [57] showing the behavior of 4 types of steels named AISI 304, T24, T92 and VM12 at 650 °C in the environment with KCl-K_2SO_4.*

The alloys in Figure 4.17 in the environment with KCl-K_2SO_4 at 650 °C support earlier conclusions that the presence of Ni affect the mass gain in such a way that the growth of the oxide scales decreases with increasing Ni content except for the steel T24. As a first observation it is quite strange that T24 without any Ni seems to have lower mass gain in comparison to the steel T92 with both Cr and Ni in the beginning of the exposure. On the other hand, previous studies by Persdotter et al. [1] proved among other things that it needs a certain amount of Cr/Ni to have some sorts of effect regarding the mass gain. The amount of Cr and Ni in this case is relatively low and one can therefore assume that it has no major effect. This may be a possible explanation for the observed behavior between the steels T24 and T92. Furthermore, the effect of Ni in Figure 4.17 also support the assumption that thermal cycling increase the sensitiveness of spallation since no spallation could be observed in Figure 4.17 with isothermal oxidation.

4.2 Experimental work

In the experimental part of the project, 4 different model alloys were investigated, Fe-5Cr-3Al, Fe-10Cr-3Al, Fe-18Cr-3Al and Fe-25Cr-3Al. After the first exposure, 48h in the environment containing 5% O_2 + 95% N_2 in presence of K_2CO_2 SEM-images was performed on each sample and the thickness of the Fe-rich oxide layer was measured from the SEM-images and are summarized in Table 4.7 together with the average calculated thickness and mass gain. The average calculated thickness is a theoretical thickness based on the formation of magnetite and the method for the calculations is explained in Appendix B.

Table 4.7: *Measured oxide thickness of model alloys after exposure in 5% O_2 + 95% N_2 in presence of K_2CO_2 for 48 hours at 600 °C.*

First exposure			
Alloy	*Thickness [μm]*	*Avg. calculated thickness [μm]*	*Mass gain [mg/cm^2]*
Fe-5Cr-3Al	36	29.296	4.186
Fe-10Cr-3Al	33	27.949	3.994
Fe-18Cr-3Al	2.5	6.527	0.933
Fe-25Cr-3Al	0.5	-1.084*	-0.155*

* Negative values due to mass loss as a result of low mass gain and that unreacted salt has been detached from the sample after the exposure.

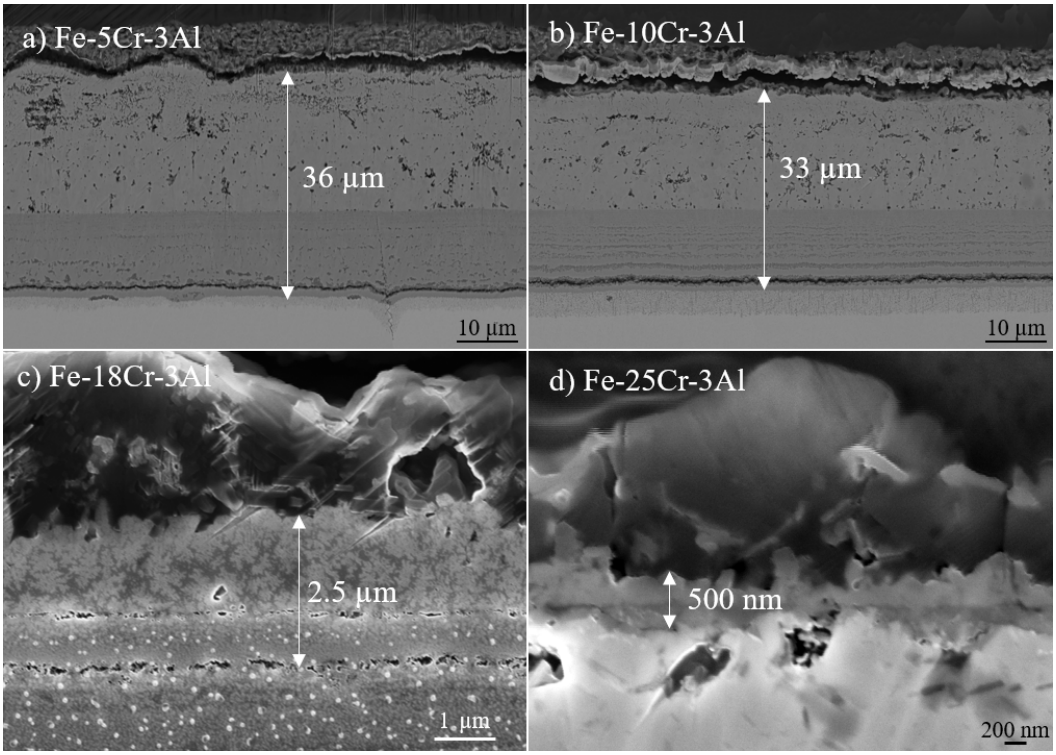

Figure 4.18: *SEM images after 48h of exposure in the environment containing 5% O_2 and 95% N_2 in presence of K_2CO_3 at 600 °C on (a) Fe-5Cr-3Al, (b) Fe-10Cr-3Al, (c) Fe-18Cr-3Al, (d) Fe-25Cr-3Al alloys.*

As can be seen in Figure 4.18, the thickness decreases with increased chromium content (5-25 wt% Cr) which is in good agreement with the obtained data by Persdotter et al. [1]. It can also be seen in these SEM-images that the measured thickness between the Fe-5Cr-3Al and Fe-10Cr-3Al was similar (∼33-36 µm). The thickness from these two alloys are considered as a thick Fe-rich oxide layer with a high growth rate. A high growth rate and a thick oxide layer indicate a poor secondary corrosion protection. For the other alloys, Fe-18Cr-3Al and Fe-25Cr-3Al an opposite behavior was obtained compared to Fe-5Cr-3Al and Fe-10Cr-3Al. They formed slow-growing Fe-rich oxide scales with thicknesses of 2.5 µm (Fe-18Cr-3Al) and 0.5 µm (Fe-25Cr-3Al). As a result from the first exposure the alloys with 18 and 25-wt% Cr showed a good secondary corrosion protection.

In order to investigate if spallation of a previously formed iron-rich oxide scale will affect the corrosion resistance of a new secondary protection, a second exposure was done on 2 selected alloys, Fe-10Cr-3Al and Fe-18Cr-3Al. These 2 alloys were selected to represent an alloy with a poor and a good secondary corrosion protection, respectively. However, before the second exposure, the oxide scale was partially removed in some areas and completely removed in other areas. This was done to investigate if different degrees of spallation influence the propagation of the oxidation process differently.

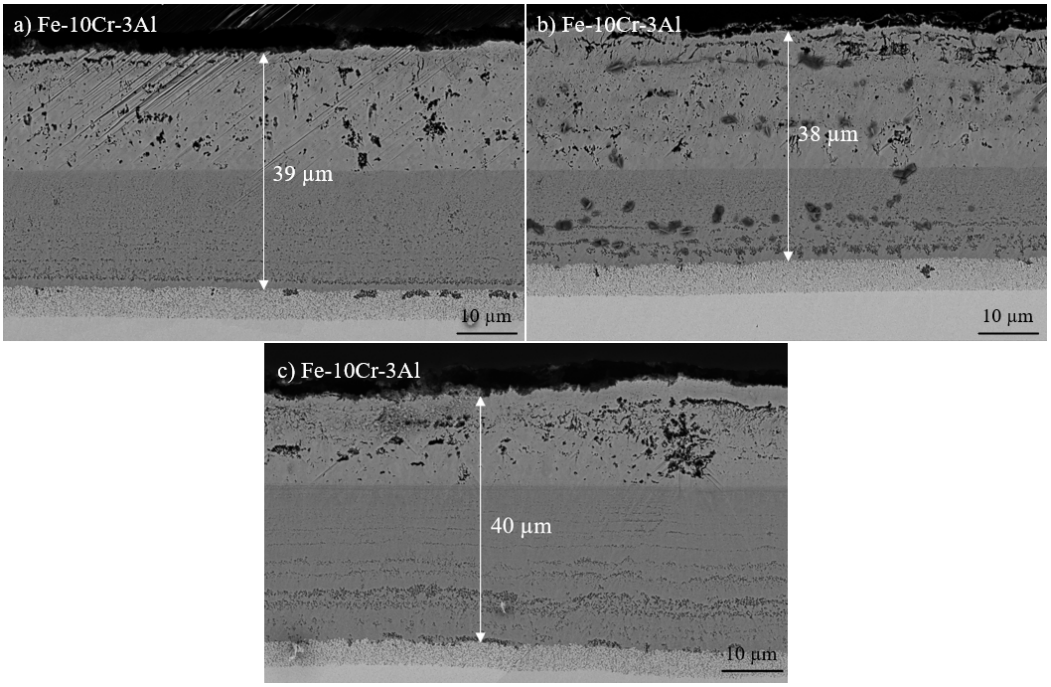

Figure 4.19: *SEM images after the second exposure of the Fe-10Cr-3Al alloy. In (a) the whole outward-growing Fe-rich oxide has been removed and some of the inward-growing spinel, in (b) the whole oxide has been removed and in (c) only little of the outward-growing Fe-oxide has been removed. In image (a)-(c) the respectively thicknesses after the second exposure is shown for the different spallation parts.*

After the first exposure a thickness of about 33 µm was obtained for the Fe-10Cr-3Al alloy as mentioned earlier. The thicknesses obtained for the alloy Fe-10Cr-3Al after the second exposure are shown in Figure 4.19. Moreover, this alloy reached a thickness of 40 µm after spallation of some of the outward-growing Fe-rich oxide. Furthermore, a thickness of 39 µm was obtained when the whole outward-growing oxide and some of the inward-growing spinel was removed. The last case of the studied Fe-10Cr-3Al was to see what happens if the whole oxide is removed. Measurement showed that a thickness of 38 µm was obtained. Since these 3 thicknesses are relatively similar independent of which part of the first secondary protection oxide scale that was removed the behavior of Fe-10Cr-3Al indicate that spallation does not affect the growth rate of the new Fe-rich oxide for model alloys that forms a poor secondary protection, since the Fe-rich oxide scale seems to stabilize ∼40 µm, as seen in the SEM-images in Figure 4.19. On the contrary, the model alloy Fe-18Cr-3Al was more affected by the partial removal of the Fe-rich oxide scale, as seen in Figure 4.20 (a). A thickness of 15 µm was obtained when the entire outward-growing oxide and some of the inward-growing spinel was removed. Furthermore, a thickness of about 700 nm (0.7 µm) was reached when the entire oxide was removed. These obtained measurements on the Fe-18Cr-3Al showed a good new secondary protection in the case when the whole oxide was spalled of since it behaved as if the alloy was being re-exposed

for new. However, it should be noticed that the new secondary protection became much thinner (0.7 µm) after the second exposure compared to the first exposure (2.5 µm). One possible cause for this behavior could be due to that different polishing/grinding methods had been used for the different exposures. In the first exposure both SiC-paper and diamond-suspension was used and in the second exposure only SiC-paper was used. In the methodology, two different spallation-induced methods was mentioned, which could be either thermally or mechanically. To fully understand if the choice of spallation-induced method have an influence one need to study them both, but this is not covered in this thesis and could be a potential future work opportunity.

However, another observation regarding the Fe-18Cr-3Al was that the thickness became about 15 µm after the second exposure with the pre-treatment when some of the inward-growing spinel and the whole outward-growing oxide was spalled of before the second exposure. After the first exposure a thickness of 2.5 µm was obtained. A possible explanation of this behavior is that when some part of the oxide is spalled of, it will grow faster in the beginning until it stabilized after some time, and that the growth rate are higher in comparison to if the oxide haven't spalled of. There are some important aspects to consider regarding the stabilizing mechanisms in this case. Usually a stabilization of the Fe-rich oxide occurs when it becomes thick enough so that the diffusion of ions between the oxide/metal interface takes long time or that a "healing layer" has formed of alumina/chromia as mentioned earlier in the Fe-Cr section. It is possible that Fe-18Cr-3Al has formed this type of healing layer during the first exposure and thus stabilizes at 2.5 µm. Moreover, if some of the oxides are grinded away and then more salt is added, the salt could then react with the healing layer and break it down. This leads to the question why it seems to take so long time for the alloy to form a new healing layer during the second exposure compared to the first exposure. This could be explained by depletion zones of chromium since depletion zones for chromium are usually seen under a chromium-rich oxide, as a lot of chromium has gone to the surface to form the chromium oxide and therefore depletes the metal underneath. If it is a relatively long depletion zone from the first exposure, it can be assumed that it will take a little bit longer time before a healing layer can be formed since there is not enough chromium at the metal surface. This would also explain why it goes more quickly to form a healing layer where the entire oxide has been grounded away.

The results from the experimental part regarding the influence of spallation for a set of model Fe-based alloys (Fe-5Cr-3Al, Fe-10Cr-3Al, Fe-18Cr-3Al and Fe-25Cr-3Al) suggested that an alloy with an already poor secondary corrosion protection were not sensitive against spallation and showed similar behavior and was stabilized at the same Fe-rich oxide thickness independent on the degree of spallation. While an alloy with a good secondary protection was more affected and deteriorated considerably in the case when some of the Fe-rich oxide was removed. This is an important conclusion when it comes to applications were thermal cycling occur.

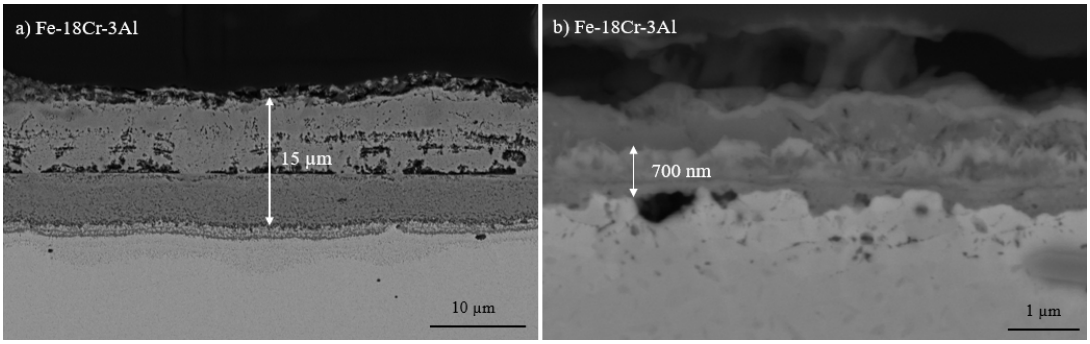

Figure 4.20: *These SEM images illustrate the result after the second exposure of the alloy Fe-18Cr-3Al. Before the second exposure 2 different spallation modifications was done. In SEM image (a) one can see the resulting thickness after spallation of the entire outward-growing oxide and some of the inward-growing spinel after the second exposure. In SEM image (b) the resulting thickness after spallation of the entire oxide after the second exposure is shown.*

5

Conclusion

This master thesis work investigated the applicability of the concept regarding primary and secondary corrosion protection of alloys in harsh environments. The focus was on the secondary protection in the temperature range 600-850 °C and in varying environmental conditions. The results from the literature review show that the concept can be applied in a broader temperature range, but also that the ability of an alloy to achieve a good secondary protection is more complex than previously known and that several factors have to be taken into consideration. Intuitively, a higher temperature is expected to lead to a faster oxide growth rate. However, initiating breakaway oxidation of an Fe-20Cr alloy at 600 and 750 °C showed that the higher temperature enabled the alloy to form a good secondary protection in contrast to the lower temperature at which the alloy displayed a poor secondary protection. This clearly shows that the concept of the secondary protection is more complex. This observation needs further investigation to confirm its reliability.

Furthermore, by altering the alloy composition, both positive and negative effects were observed depending on the alloying elements, temperatures, environmental and exposure conditions. It was observed that during cyclic oxidation, increasing the temperature increased the mass gain and thus the iron oxide growth rate of Fe-Cr alloys. Higher Cr content decreased the growth rate but due to crack formation, good secondary protection could not be formed. In addition, these Fe-Cr alloys exposed under cyclic oxidation at 600-800 °C were damaged with cracks and buckling but they were shown not to spall off.

Similar results as for the Fe-Cr alloys were also observed for Fe-based alloys containing Ni regarding that a higher temperature seemed to accelerate the Fe-rich oxide growth even more. On the contrary to Fe-Cr alloys, studies showed that an alloying element, such as Ni, increased the risk of spallation due to thermal stresses between the layers of the metal and the oxide, when cyclic oxidation occurred. This could be connected to the thermal expansion of austenitic alloys (10% Ni) since the thermal expansion is very different between austenite and iron oxide. However, a higher Ni content seemed to delay the spallation. Therefore, it is important to balance the Ni content depending on the conditions and thus not select an austenitic alloy when thermal cycling occurs.

From the experimental results regarding the model alloys Fe-5Cr-3Al, Fe-10Cr-3Al, Fe-18Cr-3Al and Fe-25Cr-3Al one could clearly see that the spallation of the oxide scales affect the new formed secondary protection in some way. The most important observations was that an alloy with an already poor secondary protection does not became worse and

was stabilized at the same thickness of the Fe-rich oxide scale, independent on the partial removal, while an alloy with a good secondary protection was more sensitive towards partial removal of the formed oxide scale and obtained a higher Fe-rich oxide thickness than before. Thus, the results of this master thesis indicate that the need and understanding of Fe-based alloys are necessary in order to improve the corrosion resistance of the secondary protection in order to select a proper alloy for the right application.

6

Future work

The focus of this thesis has been to extract data from a range of scientific articles and evaluating the data obtained from these articles. From the literature review one could clearly see that cyclic oxidation affect the alloys, especially those with Ni. A potential future work could be to study the same alloy in the same environment and temperature but with both cyclic oxidation and isothermal exposure. What happened with an alloy that have been previously exposed for a long time and then changing it into short cycles? It could also be of interest to investigate different cycle times with each other in order to see if short or long cycle times influence the secondary protection positively or more badly.

Regarding the experimental work, two different spallation-induced methods were mentioned and these were thermal or mechanical. In this master thesis a mechanical spallation-induced method was used in order to see if spallation influences the formation of a new secondary corrosion protection. The conclusion was that the spallation actually influences the new formed secondary protection. A possible future work could therefore be to investigate if the choice of spallation-induced method behave similarly or differently when it comes to the influence of the new secondary protection.

Bibliography

[1] A. Persdotter, J. Eklund, J. Liske, T. Jonsson. "Beyond breakaway corrosion – Influence of chromium, nickel and aluminum on corrosion of iron-based alloys at 600 °C". In: *Corrosion Science* 177 (2020), p. 108961.

[2] P. Kofstad. *High temperature corrosion*. London; New York: Elsevier applied science, 1988.

[3] D.J. Young. *High Temperature Oxidation and Corrosion of Metals*. 2nd ed. Elsevier Scinece & Technology, 2016.

[4] B. Gleeson. "1.09 - Thermodynamics and Theory of External and Internal Oxidation of Alloys". In: *Shreir's Corrosion*. Ed. by B. Cottis, M. Graham, R. Lidsay, S. Lyon, T. Richardson, D. Scantlebury, H. Stott. Elsevier, 2010. Chap. 1.09, pp. 180–194.

[5] J-O. Andersson, T. Helander, L. Höglund, P. Shi, B. Sundman. "Thermo-Calx & DICTRA, computational tools for materials science". In: *Calphad* 26 (2002), pp. 273–312.

[6] T. Jonsson, B. Pujilaksono, H. Heidari, F. Liu, J.-E. Svensson, M.Halvarsson, L.-G. Johansson. "Oxidation of Fe-10Cr in O_2 and O_2 + H_2O Environment at 600 °C: A microstructural investigation". In: *Corrosion Science* 75 (2013), pp. 326–336.

[7] T. Jonsson, S. Karlsson, H. Hooshyar, M. Sattari, J. Liske, J.-E. Svensson, L.-G. Johansson. "Oxidation After Breakaway of the Chromium-Rich Scale on Stainless Steels at High Temperature: Internal Oxidation". In: *Oxid Met* 85 (2016), pp. 509–536.

[8] T. Jonsson, H. Larsson, S. Karlsson, H. Hooshyar, M. Sattari, J. Liske, J.-E. Svensson, L.-G. Johansson. "High-Temperature Oxidation of FeCr(Ni) Alloys: The Behavior After Breakaway". In: *Oxid Met* 87 (2017), pp. 333–341.

[9] B. Pujilaksono, T. Jonsson, H. Heidari, M.Halvarsson, J.-E. Svensson, L.-G. Johansson. "Oxidation of Binary FeCr Alloys (Fe-2.25Cr, Fe-10Cr, Fe-18Cr and Fe-25Cr) in O_2 and O_2 + H_2O Environment at 600 °C". In: *Oxid Met* 75 (2011), pp. 183–207.

[10] The Editors of Encyclopaedia Britannica. *Alloy metallurgy*. URL: https://www.britannica.com/technology/alloy. (accessed: 09.06.2021).

[11] M. Knyazeva & M. Pohl. "Duplex Steels: Part I: Genesis, Formation, Structure". In: *Metallography, Microstructure, and Analysis* 2 (2013), pp. 113–121.

[12] C. Kittel. *Introduction to Solid State Physics*. 8th ed. United States of America: John Wiley & Sons, Inc, 2005.

[13] Callister & Rethwisch. *Body Centered Cubic Structure (BCC)*. URL: https://www.e-education.psu.edu/matse81/node/2132. (accessed: 01.06.2021).

[14] The Editors of Encyclopaedia Britannica. *Ferrite iron oxide compound*. URL: https://www.britannica.com/science/ferrite-iron-oxide-compound. (accessed: 10.06.2021).

[15] I. Persechino. "Development of a polycrystal plasticity simulation tool including recrystallization (DRX) phenomena". In: *PhD thesis, Università degli studi di Cassino e del Lazio Meridionale, Cassino, Italy* (2017).

[16] ThoughtCo. *The Characteristics of Austenitic Stainless Steel*. URL: https://www.thoughtco.com/metal-profile-austenitic-stainless-2340126. (accessed: 10.06.2021).

[17] E. McCafferty. *Introduction to Corrosion Science*. New York: Springer Science Business Media, 2010.

[18] G.B. Gibbs & R. Hales. "The influence of metal lattice vacancies on the oxidation of high temperature materials". In: *Corrosion Science* 17 (1977), pp. 487–507.

[19] J. Eklund. "High Temperature Corrosion of FeCrAl Alloys in Biomass- and Wastefired Boilers." In: *Department of Chemistry and Chemical Engineering* (2020).

[20] A. Persdotter. "A microstructural investigation of chlorine induced high temperature corrosion of a low alloyed steel". In: *Master thesis, Chalmers University of Technology(CTH), Gothenburg, Sweden* (2016).

[21] G.H. Meier N. Birks and F.S. Pettit. *Introduction to the High- Temperature Oxidation of Matals*. 2nd ed. Cambridge University Press, 2006.

[22] The Editors of Encyclopaedia Britannica. *Crystal defect-crystallography*. URL: https://www.britannica.com/science/crystal-defect. (accessed: 10.05.2021).

[23] C.W. D Jr. *Materials science and engineering: an introduction*. 8th ed. John Wiley & Sons. Inc, 2007.

[24] A.S Khanna. *Introduction to High Temperature Oxidation and Corrosion*. London; New York: ASM International, 2002.

[25] C. Wagner. *Beitrag zur theorie des anlaufvorgangs*. Zeitschrift für Physikalische Chemie, 21B:25–41, 1933.

[26] Kristine Rodulfo Tolod, Simelys Hernández, Elsje Alessandra Quadrelli, Nunzio Russo. "Horizons in Sustainable Industrial Chemistry and Catalysis". In: *Studies in Surface Science and Catalysis* 178 (2019), pp. 65–84.

[27] W. Ahmad, M. H. Mamat, A. S. Zoolfakar, Z. Khusaimi, M. Rusop. "A review on hematite α-Fe_2O_3 focusing on nanostructures, synthesis methods and applications". In: *2016 IEEE Student Conference on Research and Development (SCOReD)* (2016).

[28] W. Wu, Z. Wu, T. Yu, C. Jiang, W-S. Kim. "Recent progress on magnetic iron oxide nanoparticles: synthesis, surface functional strategies and biomedical applications". In: *Science and technology of advanced materials* 16 (2015).

[29] J. Eklund, B. Jönsson, A. Persdotter, J.Liske, J.-E. Svensson, T. Jonsson. "The influence of silicon on the corrosion properties of FeCrAl model alloys in oxidizing environments at 600 °C". In: *Corrosion Science* 144 (2018), pp. 266–276.

[30] H. J. Grabke, E. Reese and M. Spiegel. "The effects of chlorides, hydrogen chloride, and sulfur dioxide in the oxidation of steels below deposits". In: *Corrosion Science* 7 (1995), pp. 1023–1043.

[31] N.Folkeson, T. Jonsson, M. Halvarsson, L.-G. Johansson, J.-E. Svensson. "The influence of small amounts of KCl(s) on the high temperature corrosion of a Fe-2.25Cr-1Mo steel at 400 and 500°C". In: *Materials and Corrosion* 62 (2011), pp. 606–615.

[32] J.Pettersson, H. Asteman, J.-E. Svensson L.-G. Johansson. "KCl Induced Corrosion of a 304-type Austenitic Stainless Steel at 600°C; The Role of Potassium". In: *Oxid Met* 64 (2005), pp. 23–41.

[33] T. Jonsson, J. Froitzheim, J. Pettersson, J.-E. Svensson, L.-G. Johansson, M. Halvarsson. "The Influence of KCl on the Corrosion of an Austenitic Stainless Steel (304L) in Oxidizing Humid Conditions at 600°C: A Microstructural Study". In: *Oxid Met* 72 (2009), pp. 213–239.

[34] J. Pettersson, J.-E. Svensson, L.-G. Johansson. "KCl-Induced Corrosion of a 304-type Austenitic Stainless Steel in O_2 and in O_2 + H_2O Environment: The Influence of Temperature". In: *Oxid Met* 72 (2009), pp. 159–177.

[35] Y. Yan. "Tribology and tribocorrosion testing and analysis of metallic biomaterials: Scanning Electron Microscopy". In: *Woodhead Publishing Series in Biomaterials* (2019), pp. 213–234.

[36] Mark T. Weller and Nigel A. Young. *Characterisation methods in inorganic chemistry.* Madison Avenue, New York: Oxford University Press, 2017.

[37] J. Goldstein, D.E. Newbury, D.C. Joy, C.E. Lyman, P. Echlin, E. Lifshin, L. Sawyer and J.R. Mikael. *Scanning Electron Microscopy and X-Ray Microanalysis.* 3rd ed. Springer Science + Business Media, LLC, 2007.

[38] T. Jonsson. "Microscopy of high temperature oxidation of iron and some stainless steel". In: *Department of Chemistry and Chemical Engineering* (2007).

[39] Materials Evaluation and Inc. Engineering. *Energy Dispersive X-ray Spectroscopy (EDX).* URL: `https://www.mee-inc.com/hamm/energy-dispersive-x-ray-spectroscopyeds/`. (accessed: 11.05.2021).

[40] J. Pettersson, N. Folkeson, L-G. Johansson & J-E. Svensson. "The Effect of KCl, K_2SO_4 and K_2CO_3 on the High Temperature Corrosion of a 304-Type Autenitic Stainless Steel". In: *Oxidation of Metals* 76 (2011), pp. 93–109.

[41] M. Cao, L. Liu, Z. Yu, L. Fan, L. Ying & F. Wang. "Studies on the corrosion behavior of Fe-20Cr alloy in NaCl solution spray at 600°C". In: *Corrosion Science* 133 (2018), pp. 165–177.

[42] H.T. Ma, C.H. Zhou & L. Wang. "High temperature corrosion of pure Fe, Cr and Fe–Cr binary alloys in O_2 containing trace KCl vapour at 750°C". In: *Corrosion Science* 51 (2009), pp. 1861–1867.

[43] N. Israelsson, K. Hellström, J.-E. Svensson, L.-G. Johansson. "KCl-Induced Corrosion of the FeCrAl Alloy Kanthal AF at 600 °C and the Effect of H_2O". In: *Oxid Met* 83 (2015), pp. 1–27.

[44] S.R.J. Sauders, M. Monteiro, F. Rizzo. "The oxidation behaviour of metals and alloys at high temperatures in atmospheres containing water vapour: A review". In: *Progress in Materials Science* 53 (2008), pp. 775–837.

[45] B. Pujilaksono, T. Jonsson, M.Halvarsson, J.-E. Svensson, L.-G. Johansson. "Oxidation of iron at 400-600 °C in dry and wet O_2". In: *Corrosion Science* 52 (2010), pp. 1560–1569.

[46] S. Karlsson, J. Pettersson, L.-G. Johansson, J.-E. Svensson. "Alkali Induced High Temperature Corrosion of Stainless Steel: The Influence of NaCl, KCl and $CaCl_2$". In: *Oxid Met* 78 (2012), pp. 83–102.

[47] S. Enestam, D. Bankiewicz, J. Tuiremo, K. Makela, M. Hupa. "Are NaCl and KCl equally corrosive on superheater materials of steam boilers?" In: *Fuel* 104 (2013), pp. 294–306.

[48] N.K. Othman, J. Zhang & D.J. Young. "Temperature and water vapour effects on the cyclic oxidation behaviour of Fe–Cr alloys". In: *Corrosion Science* 52 (2010), pp. 2827–2836.

[49] B. Pujilaksono, T. Jonsson, M.Halvarsson, I. Panas, J.-E. Svensson, L.-G. Johansson. "Paralinear Oxidation of Chromium in O_2 + H_2O Environment at 600-700 °C". In: *Oxid Met* 70 (2008), pp. 163–188.

[50] N.K Othman, J. Zhang & D.J. Young. "Effect of water vapour on cyclic oxidation of Fe-Cr alloys". In: *Materials and Corrosion* 62 (2011), pp. 496–503.

[51] R. Peraldi & B.A. Pint. "Effect of Cr and Ni Contents on the Oxidation Behavior of Ferritic and Austenitic Model Alloys in Air with Water Vapor". In: *Oxidation of Metals* 61 (2004), pp. 463–483.

[52] SANDVIK. *SANICRO® 28 Tube and pipe, seamless.* URL: `https://www.materials.sandvik/en/materials-center/material-datasheets/tube-and-pipe-seamless/sanicro-28/`. (accessed: 22.06.2021).

[53] SANDVIK. *SANDVIK 4C54 Tube and pipe, seamless.* URL: `https://www.materials.sandvik/en/materials-center/material-datasheets/tube-and-pipe-seamless/sandvik-4c54/`. (accessed: 22.06.2021).

[54] F.C. Hull, S.K. Hwang, J.M. Wells, & R.I. Jaffee. "Effect of composition on thermal expansion of alloys used in power generation". In: *Journal of Materials Engineering* 9 (1987), pp. 81–92.

[55] Valves Instruments Plus Ltd. *Thermal Expansion.* URL: `https://www.vip-ltd.co.uk/Expansion/Thermal_Expansion.pdf`. (accessed: 08.06.2021).

[56] K.K. Aye, T.D Nguyen, J. Zhang & D.J. Young. "Effect of silicon on corrosion of Fe-20Cr and Fe-20Cr-20Ni alloys in wet CO_2 with and without HCl at 650°C". In: *Corrosion Science* 179 (2021).

[57] N. Abu-Warda, A.J. López, F. Pedraza & M.V. Utrilla. "Corrosion behavior of T24, T92, VM12 and AISI 304 steels exposed to KCl-NaCl-K_2SO_4 salt mixtures". In: *Materials and Corrosion* 72 (2020), pp. 936–950.

[58] G.H. Meier, K. Jung, N. Mu, N.M. Yanar, F.S. Pettit, J.P. Abellán, T. Olszewski, L.N Hierro, W.J. Quadakkers & G.R. Holcomb. "Effect of Alloy Composition and Exposure Conditions on the Selective Oxidation Behavior of Ferritic Fe–Cr and Fe–Cr–X Alloys". In: *Oxidation of Metals* 74 (2010), pp. 319–340.

[59] Y. Xie, Y. Cai, J. Zhang, B. Gleeson & D.J. Young. "Effects of Sulphate Deposits on Corrosion Behaviour of Fe-Based Alloys in Wet CO_2 Gas at 750°C". In: *Oxidation of Metals* 95 (2020), pp. 23–43.

[60] T. Gheno, D. Monceau & D.J. Young. "Kinetics of breakaway oxidation of Fe–Cr and Fe–Cr–Ni alloys in dry and wet carbon dioxide". In: *Corrosion Science* 77 (2013), pp. 246–256.

[61] A. Col, V. Parry & C. Pascal. "Oxidation of a Fe–18Cr–8Ni austenitic stainless steel at 850°C in O_2: Microstructure evolution during breakaway oxidation". In: *Corrosion Science* 114 (2017), pp. 17–27.

[62] M.P. Brady, J.R. Keiser, K.L. More, M. Fayek, L.R. Walker, R.A. Peascoe-Meisner, L.M. Anovitz, D.J. Wesolowski & D.R. Cole. "Comparison of Short-Term Oxidation Behavior of Model and Commercial Chromia-Forming Ferritic Stainless Steels in Dry and Wet Air". In: *Oxidation of Metals* 78 (2012), pp. 1–16.

[63] Z. Yu, M. Chen, C. Shen, S. Zhu & F. Wang. "Oxidation of an austenitic stainless steel with or without alloyed aluminum in O_2 + 10% H_2O environment at 800°C". In: *Corrosion Science* 121 (2017), pp. 105–115.

[64] M.I. Sahri, N.K. Othman, Z. Shamsu & A.R. Daud. "Investigation of high temperature corrosion behavior on 304L austenite stainless steel in corrosive environments". In: *AIP Conference Proceedings 1614* (2014), pp. 152–157.

[65] Z. Shen, D. Tweddle, H. Yu, G. He, A. Varambhia, P. Karamched, F. Hofmann, A.J. Wilkinson, M.P. Moody, L. Zhang & S. Lozano-Perez. "Microstructural understanding

of the oxidation of an austenitic stainless steel in high-temperature steam through advanced characterization". In: *Acta Materialia* 194 (2020), pp. 321–336.

[66] F. Wang & Y. Shu. "Influence of Cr Content on the Corrosion of Fe–Cr Alloys: The Synergistic Effect of NaCl and Water Vapor". In: *Oxidation of Metals* 59 (2003), pp. 201–214.

[67] Y.S. Li, M. Spiegel & S. Shimada. "Corrosion behaviour of various model alloys with NaCl-KCl coating". In: *Materials Chemistry and Physics* 93 (2005), pp. 217–223.

[68] Y.S. Li & M. Spiegel. "Internal Oxidation of Fe-Al Alloys in a KCl-Air Atmosphere at 650°C". In: *Oxidation of Metals* 61 (2004), pp. 303–322.

[69] Y.S. Li, Y. Niu & M. Spiegel. "High temperature interaction of Al/Si-modified Fe-Cr alloys with KCl". In: *Corrosion Science* 49 (2007), pp. 1799–1815.

[70] H. Asteman & M. Spiegel. "Investigation of the HCl (g) attack on pre-oxidized pure Fe, Cr, Ni and commercial 304 steel at 400°C". In: *Corrosion Science* 49 (2007), pp. 3626–3637.

A

Appendix

Table A.1: *Article 1 (1/4): Effect of Cr and Ni Contents on the Oxidation Behavior of Ferritic and Austenitic Model Alloys in Air with Water Vapor [51].*

Environment: air + 10% water vapor							
Alloys	**Microstructure**	**Temperature 650 °C**					
		Behavior	**Exposure time (h)**	**Cycles**	**Comments**	**Growth rate/mass gain**	**Comments**
Fe-10Cr	Ferrite	AA	-	-	-	-	-
Fe-12Cr	Ferrite	AA	-	-	-	-	-
Fe-14Cr	Ferrite	AA	-	-	-	-	-
Fe-16Cr	Ferrite	AA	-	-	-	-	-
Fe-18Cr	Ferrite	AA	-	20x1hr	-	-	-
Fe-20 Cr	Ferrite	AA	-	20x1hr	-	-	-
Fe-20Cr-30Ni	Austenite	POS	-	100x1hr	-	-	-
Fe-20Cr-25Ni	Austenite	POS	-	100x1hr	-	-	-
Fe-20Cr-20Ni	Austenite	POS	-	100x1hr	-	-	-
Fe-20Cr-15Ni	Austenite	POS	-	100x1hr	-	-	-
Fe-20Cr-10Ni	Austenite+Ferrite	POS +AA	-	100x1hr	-	-	-
Fe-18Cr-30Ni	Austenite	POS	-	100x1hr	-	-	-
Fe-18Cr-25Ni	Austenite	POS	-	100x1hr	-	-	-
Fe-18Cr-20Ni	Austenite	POS	-	100x1hr	-	-	-
Fe-18Cr-15Ni	Austenite	POS	-	80x1hr	-	-	-
Fe-18Cr-10Ni	Austenite+Ferrite	AAS	-	40x1hr	-	-	-
Fe-16Cr-30Ni	Austenite	POS	-	100x1hr	-	-	-
Fe-16Cr-25Ni	Austenite	POS	-	100x1hr	-	-	-
Fe-16Cr-20Ni	Austenite	AA	-	80x1hr	-	-	-
Fe-16Cr-15Ni	Austenite	AAS	-	80x1hr	-	-	-
Fe-16Cr-10Ni	Austenite+Ferrite	AAS	-	20x1hr	-	-	-

Table A.2: *Article 1 (2/4): Effect of Cr and Ni Contents on the Oxidation Behavior of Ferritic and Austenitic Model Alloys in Air with Water Vapor [51].*

Environment: air + 10% water vapor								
Alloys	**Microstructure**	**Temperature 650 °C**						
		Spallation	**Comments**	**Thickness**	**Growth rate (µm/h)**	**Type of oxide**	**Comments**	**Corrosion regime**
Fe-10Cr	Ferrite	No	-	150 µm (SP)	1.5	-	100x1hr cycles	Secondary
Fe-12Cr	Ferrite	No	-	-	-	-	-	Secondary
Fe-14Cr	Ferrite	No	-	-	-	-	-	Secondary
Fe-16Cr	Ferrite	No	-	140 µm (SP)	1.4	-	100x1hr cycles	Secondary
Fe-18Cr	Ferrite	No	-	-	-	-	-	Secondary
Fe-20 Cr	Ferrite	No	-	60 µm (SP)	0.6	-	100x1hr cycles	Secondary
Fe-20Cr-30Ni	Austenite	No	-	1 µm (PP)	0.01	-	100x1hr cycles	Primary
Fe-20Cr-25Ni	Austenite	No	-	-	-	-	-	Primary
Fe-20Cr-20Ni	Austenite	No	-	-	-	-	-	Primary
Fe-20Cr-15Ni	Austenite	No	-	-	-	-	-	Primary
Fe-20Cr-10Ni	Austenite+Ferrite	No	-	12 µm(SP) 1 m (PP)	0.12	-	100x1hr cycles	Primary
Fe-18Cr-30Ni	Austenite	No	-	-	-	-	-	Primary
Fe-18Cr-25Ni	Austenite	No	-	-	-	-	-	Primary
Fe-18Cr-20Ni	Austenite	No	-	-	-	-	-	Primary
Fe-18Cr-15Ni	Austenite	No	-	-	-	-	-	Secondary
Fe-18Cr-10Ni	Austenite+Ferrite	Yes	-	-	-	-	-	Secondary
Fe-16Cr-30Ni	Austenite	No	-	2 µm (PP)	0.02	-	100x1hr cycles	Primary
Fe-16Cr-25Ni	Austenite	No	-	-	-	-	-	Primary
Fe-16Cr-20Ni	Austenite	No	-	-	-	-	-	Secondary
Fe-16Cr-15Ni	Austenite	Yes	-	-	-	-	-	Secondary
Fe-16Cr-10Ni	Austenite+Ferrite	Yes	-	26 µm (SP)	0.26	-	100x1hr cycles	Secondary

Table A.3: *Article 1 (3/4): Effect of Cr and Ni Contents on the Oxidation Behavior of Ferritic and Austenitic Model Alloys in Air with Water Vapor [51].*

Environment: air + 10% water vapor							
Alloys	**Microstructure**	**Temperature 800 °C**					
		Behavior	**Exposure time**	**Cycles**	**Comments**	**Growth rate/mass gain**	**Comments**
Fe-10Cr	Ferrite	AA	-	-	-	-	-
Fe-12Cr	Ferrite	AA	-	-	-	-	-
Fe-14Cr	Ferrite	AA	-	-	-	-	-
Fe-16Cr	Ferrite	POS	-	mass loss after 20 cycles	-	-	-
Fe-18Cr	Ferrite	POS	-	mass loss after 20 cycles	-	-	-
Fe-20 Cr	Ferrite	POS	-	mass loss after 20 cycles	-	-	-
Fe-20Cr-30Ni	Austenite	AA	-	-	-	-	-
Fe-20Cr-25Ni	Austenite	AA	-	-	-	-	-
Fe-20Cr-20Ni	Austenite	AAS	-	-	-	-	-
Fe-20Cr-15Ni	Austenite	AAS	-	-	-	-	-
Fe-20Cr-10Ni	Austenite+Ferrite	AAS	-	-	-	-	-
Fe-18Cr-30Ni	Austenite	AA	-	-	-	-	-
Fe-18Cr-25Ni	Austenite	AA	-	-	-	-	-
Fe-18Cr-20Ni	Austenite	AAS	-	-	-	-	-
Fe-18Cr-15Ni	Austenite	AAS	-	-	-	-	-
Fe-18Cr-10Ni	Austenite+Ferrite	AAS	-	-	-	-	-
Fe-16Cr-30Ni	Austenite	AA	-	-	-	-	-
Fe-16Cr-25Ni	Austenite	AAS	-	-	-	-	-
Fe-16Cr-20Ni	Austenite	AAS	-	-	-	-	-
Fe-16Cr-15Ni	Austenite	AAS	-	-	-	-	-
Fe-16Cr-10Ni	Austenite+Ferrite	AAS	-	-	-	-	-

Table A.4: *Article 1 (4/4): Effect of Cr and Ni Contents on the Oxidation Behavior of Ferritic and Austenitic Model Alloys in Air with Water Vapor [51].*

Environment: air + 10% water vapor								
Alloys	**Microstructure**	**Temperature 800 °C**						
		Spallation	**Comments**	**Thickness**	**Growth rate (µm/h)**	**Type of oxide**	**Comments**	**Corrosion regime**
Fe-10Cr	Ferrite	No	-	360 µm (SP)	3.6	-	100x1hr cycles	Secondary
Fe-12Cr	Ferrite	No	-	-	-	-	-	Secondary
Fe-14Cr	Ferrite	No	-	-	-	-	-	Secondary
Fe-16Cr	Ferrite	No	-	2 µm (PP)	0.02	-	100x1hr cycles	Primary
Fe-18Cr	Ferrite	No	-	-	-	-	-	Primary
Fe-20 Cr	Ferrite	No	-	4 µm (PP)	0.04	-	100x1hr cycles	Primary
Fe-20Cr-30Ni	Austenite	No	-	20 µm (SP)	0.2	-	100x1hr cycles	Secondary
Fe-20Cr-25Ni	Austenite	No	-	-	-	-	-	Secondary
Fe-20Cr-20Ni	Austenite	Yes	-	-	-	-	-	Secondary
Fe-20Cr-15Ni	Austenite	Yes	-	-	-	-	-	Secondary
Fe-20Cr-10Ni	Austenite+Ferrite	Yes	-	180 µm (SP)	1.8	-	100x1hr cycles	Secondary
Fe-18Cr-30Ni	Austenite	No	-	-	-	-	-	Secondary
Fe-18Cr-25Ni	Austenite	No	-	-	-	-	-	Secondary
Fe-18Cr-20Ni	Austenite	Yes	-	-	-	-	-	Secondary
Fe-18Cr-15Ni	Austenite	Yes	-	-	-	-	-	Secondary
Fe-18Cr-10Ni	Austenite+Ferrite	Yes	-	-	-	-	-	Secondary
Fe-16Cr-30Ni	Austenite	No	-	110 µm (SP)	1.1	-	100x1hr cycles	Secondary
Fe-16Cr-25Ni	Austenite	Yes	-	-	-	-	-	Secondary
Fe-16Cr-20Ni	Austenite	Yes	-	-	-	-	-	Secondary
Fe-16Cr-15Ni	Austenite	Yes	-	-	-	-	-	Secondary
Fe-16Cr-10Ni	Austenite+Ferrite	Yes	-	270 µm (SP)	2.7	-	100x1hr cycles	Secondary

Table A.5: *Article 2 (1/1): Effect of Alloy Composition and Exposure Conditions on the Selective Oxidation Behavior of Ferritic Fe-Cr and Fe-Cr-X Alloys [58].*

Temperature: 650 °C								
Alloys	**Microstructure**	**Environment: Ar-30% H_2O**						
		Behavior	**Exposure time (h)**	**Cycles**	**Comments**	**Growth rate/mass gain**	**Comments**	
Fe-10Cr	Ferrite	AA	96	-	-	21.03 mg/cm^2	-	
Fe-13.5Cr	Ferrite	AA	96	-	-	16.56 mg/cm^2	-	
Fe-22Cr	Ferrite	POS	96	-	-	0.65 mg/cm^2	-	
		Spallation	**Comments**	**Thickness (µm)**	**Growth rate (µm/h)**	**Type of oxide**	**Comments**	**Corrosion regime**
Fe-10Cr	Ferrite	-	-	∼158	1.5625	Thick scale with layered Fe-oxides. Fe_3O_4 & FeO	-	Secondary
Fe-13.5Cr	Ferrite	-	-	∼142	1.4375	Thick scale with layered Fe-oxides. Fe_3O_4 & FeO	-	Secondary
Fe-22Cr	Ferrite	-	-	-	-	Thin chromia scale Cr_2O_3	-	Secondary
		Environment: 70% CO_2-30% H_2O						
		Behavior	**Exposure time (h)**	**Cycles**	**Comments**	**Growth rate/mass gain**	**Comments**	
Fe-10Cr	Ferrite	AA	96	-	-	33.06 mg/cm^2	-	
Fe-13.5Cr	Ferrite	AA	96	-	-	19.61 mg/cm^2	-	
Fe-22Cr	Ferrite	POS	96	-	-	1.04 mg/cm^2	-	
		Spallation	**Comments**	**Thickness (µm)**	**Growth rate (µm/h)**	**Type of oxide**	**Comments**	**Corrosion regime**
Fe-10Cr	Ferrite	-	-	∼243	2.53125	Thick scale with layered Fe-oxides. Fe_3O_4 & FeO	-	Secondary
Fe-13.5Cr	Ferrite	-	-	∼170	1.69792	Thick scale with layered Fe-oxides. Fe_3O_4 & FeO	-	Secondary
Fe-22Cr	Ferrite	-	-	-	-	Thin chromia scale Cr_2O_3	-	Primary

Table A.6: *Article 3 (1/2): Effects of Sulphate Deposits on Corrosion Behaviour of Fe-based Alloys in Wet CO_2 Gas at 750 °C [59].*

Temperature: 750 °C								
Alloys	**Microstructure**	**Environment: H_2O + CO_2 without salt deposits**						
		Behavior	**Exposure time**	**Cycles**	**Comments**	**Growth rate/mass gain**	**Comments**	
Fe-25Cr	Ferrite	POS	300	-	After 300 h each sample cooled down to room temp. in the furnace and then analyzed	-	No mass gain-time curve found in the article	
Fe-25Cr-2Mn-1Si	Ferrite	POS	300	-	After 300 h each sample cooled down to room temp. in the furnace and then analyzed	-	No mass gain-time curve found in the article	
Fe-25Cr-20Ni	Austenite	AAS	300	-	After 300 h each sample cooled down to room temp. in the furnace and then analyzed	-	No mass gain-time curve found in the article	
310 stainless steel	Austenite	POS+AA	300	-	After 300 h each sample cooled down to room temp. in the furnace and then analyzed	-	No mass gain-time curve found in the article	
		Spallation	**Comments**	**Thickness (µm)**	**Growth rate (µm/h)**	**Type of oxide**	**Comments**	**Corrosion regime**
Fe-25Cr	Ferrite	No	-	0.85 µm (0.9±0.1 µm)	0.00283	Cr_2O_3 and minor $FeCr_2O_4$	$FeCr_2O_4$ not visible in the SEM image due to small amounts -Protective chromia scale.	Primary
Fe-25Cr-2Mn-1Si	Ferrite	No	-	1.14 µm (1±0.2 µm total thickness)	0.00380	Cr_2O_3, Mn_3O_4 and $MnCr_2O_4$, SiO_2 (sublayer)	-	Primary
Fe-25Cr-20Ni	Austenite	Yes	Spallation of the outer layer (Fe_2O_3+$NiFe_2O_4$)	19.29 µm total thickness (outer scale: (Fe,Ni)-rich layer: 12±2 µm, intermediate mixed (Fe,Ni,Cr) oxides: 4.5±0.4 µm, inner Cr_2O_3 band: 1.5±0.2 µm)	0.06430	Outer scale layer as Fe_2O_3+ $NiFe_2O_4$ mixture, the inner layer as mixed (Ni,Cr,Fe)-oxide, and the innermost layer as Cr_2O_3	-	Secondary
310 stainless steel	Austenite	No	-	3.89 µm (Fe,Ni)-rich nodules ∼8.3 µm, local chromia scale	0.01297	Cr_2O_3, Fe_2O_3 and $(Ni,Cr,Fe)_3O_4$, SiO_2	Thin oxide scale was found	Primary + Secondary (onset)

Table A.7: *Article 3 (2/2): Effects of Sulphate Deposits on Corrosion Behaviour of Fe-based Alloys in Wet CO_2 Gas at 750 °C [59].*

Temperature: 750 °C								
Alloys	**Microstructure**	**Environment: H_2O + CO_2 with salt deposits**						
		Behavior	**Exposure time (h)**	**Cycles**	**Comments**	**Growth rate/mass gain**	**Comments**	
Fe-25Cr	Ferrite	POS	300	-	After 300 h each sample cooled down to room temp. in the furnace and then analyzed	No mass gain-time curve found in the article	-	
Fe-25Cr-2Mn-1Si	Ferrite	POS	300	-	After 300 h each sample cooled down to room temp. in the furnace and then analyzed	No mass gain-time curve found in the article	-	
Fe-25Cr-20Ni	Austenite	POS+AA	300	-	After 300 h each sample cooled down to room temp. in the furnace and then analyzed	No mass gain-time curve found in the article	-	
310 stainless steel	Austenite	POS+AA	300	-	After 300 h each sample cooled down to room temp. in the furnace and then analyzed	No mass gain-time curve found in the article	-	
		Spallation	**Comments**	**Thickness (µm)**	**Growth rate (µm/h)**	**Type of oxide**	**Comments**	**Corrosion regime**
Fe-25Cr	Ferrite	No	-	4.29 µm chromia scale: 3.7±0.2 µm	0.01430	External chromia scale (mostly)	The chromia scale is locally overlaid by randomly distributed, thin regions of (Fe,Cr)-oxide, sparse intergranular internal sulphides.	Primary
Fe-25Cr-2Mn-1Si	Ferrite	No	-	2.15µm (total: 1.8±0.3 µm)	0.00717	Thin scale of (Mn,Cr)-rich oxide near the surface and chromia beneath.	Si near the interface scale-alloy, no sulphides	Primary
Fe-25Cr-20Ni	Austenite	No	-	6.25 µm Nodules (outer(Fe,Ni)-rich layer: 3.7 ±0.4 µm, Cr_2O_3 band: 2.1±0.3 µm)+local Cr_2O_3 scale	0.02083	Thin chromia scale (Fe,Ni)-oxide	Shallow nodules, inter- and intragranular internal sulphides	Primary + Secondary
310 stainless steel	Austenite	No	-	3.14 µm ∼ 4.2 µm (Fe,Ni)-rich nodules	0.01047	Fe-oxide + (Fe,Ni)-oxide (outer layer), Cr-rich oxide with high content of Mn (inner layer).	Intergranular internal sulphides	Primary + Secondary

Table A.8: *Article 4 (1/2): Effect of silicon on corrosion of Fe-20Cr and Fe-20Cr-20Ni alloys in wet CO_2 with and without HCl at 650 °C [56].*

Temperature: 650 °C								
Alloys	**Microstructure**	**Environment: N_2-10CO_2-10H_2O**						
		Behavior	**Exposure time (h)**	**Cycles**	**Comments**	**Growth rate/mass gain**	**Comments**	
Fe-20Cr	Ferrite	AA	290	-	Each sample was exposed only once	∼1.7 mg/cm^2	Mass gain after 290h	
Fe-20Cr-20Ni	Austenite	POS	290	-	Each sample was exposed only once	<0.2 mg/cm^2	Oxidation rate is slow	
		Spallation	**Comments**	**Thickness (µm) (measured after 290h)**	**Growth rate (µm/h)**	**Type of oxide**	**Comments**	**Corrosion regime**
Fe-20Cr	Ferrite	No	-	∼85.7 µm (20±10)	0.29552	Fe_2O_3 and $(Fe,Cr)_3O_4$	Oxide nodules. 50 procent surface coverage (The depth of inner oxide measured below the orginal alloy surface)	Primary + Secondary
Fe-20Cr-20Ni	Austenite	Yes	-	To low surface coverage so there was no "scale" to measure (10±7)	-	Fe_2O_3 and Fe_3O_4	Oxide nodules. ∼40 % surface coverage (The depth of inner oxide measured below the orginal alloy surface)	Primary + Secondary

Table A.9: *Article 4 (2/2): Effect of silicon on corrosion of Fe-20Cr and Fe-20Cr-20Ni alloys in wet CO_2 with and without HCl at 650 °C [56].*

Temperature: 650 °C								
Alloys	**Microstructure**	**Environment: wet carbon dioxide (N_2-10CO_2-10H_2O) with HCl (0.05 % and 0.1 %)**						
		Behavior	**Exposure time (h)**	**Cycles**	**Comments**	**Growth rate/mass gain (mg/cm^2)**	**Comments**	
Fe-20Cr	Ferrite	AA	290	-	-	with 0.05 % HCl: ∼6.6 (150h) to ∼5.8 (290h) With 0.1 % HCl: ∼11 (290h) slightly reduced growth rate after 160h	weigh gain was about 6 times higher with 0.01% HCl than without. After 160h the weight gain increase in 0.1% HCl but slightly decrease in 0.05% HCl	
Fe-20Cr-20Ni	Austenite	AA	290	-	-	with 0.05% HCl: 0.3 after 160h ∼0.68 after 290 With 0.1 procent HCI: 0.28 after 160h 0.95 after 290	The reaction rate accelerated after 160h in both cases	
		Spallation	**Comments**	**Thickness (µm) (measured after 290h)**	**Growth rate (µm/h)**	**Type of oxide**	**Comments**	**Corrosion regime**
Fe-20Cr	Ferrite	No	slightly mass loss in 0.05% HCl	∼114.3 µm (0.05% HCl) ∼171.4 (0.1% HCl) 50±25(0.05% HCl) 70±10 (0.1% HCl)	0.39414 0.59103	Fe_2O_3 and $(Fe,Cr)_3O_4$	100% surface coverage The accelerating effect became more significant when HCl increased from 0.05 to 0.1% Thicker and more porous oxide layers in 0.1% HCl The depth of inner oxide measured below the original alloy surface	Secondary
Fe-20Cr-20Ni	Austenite	No	-	∼42.9 (0.05% HCl) ∼85.7 (0.1% HCl) 30± 15(0.05% HCl) 60±15 (0.1% HCl)	0.14793 0.29552	Fe_2O_3 and Fe_3O_4	100% surface coverage (0.05% HCl) 70% surface coverage (0.1% HCl) Formed more porous outer Fe-rich oxide scale. The depth of inner oxide measured below the original alloy surface	Secondary

Table A.10: *Article 5 (1/1): The Effect of KCl, K_2SO_4 and K_2CO_3 on the High Temperature Corrosion of a 304-Type Autenitic Stainless steel [40].*

Environment: 5% O_2 + 40% H_2O in the presence of K_2CO_3/KCl (1.35 µmol K^+/cm^2)								
Alloys	**Microstructure**	**Temperature: 500 °C**						
		Behavior	**Exposure time (h)**	**Cycles**	**Comments**	**Growth rate/mass gain After 168h**	**Comments**	
304L (Fe-18.5Cr-10.2Ni)	Austenite	-	168	-	-	∼0.225 mg/cm^2	-	
		Spallation	**Comments**	**Thickness (µm)**	**Growth rate (µm/h)**	**Type of oxide 24h**	**Comments**	**Corrosion regime**
304L (Fe-18.5Cr-10.2Ni)	Austenite	-	Is not discussed in the article	Thin	-	Fe_2O_3 and Fe_3O_4	salts are still detected after 24h. Formation of K_2CrO_4 (Potassium chromate)	Secondary
		Temperature: 600 °C						
		Behavior	Exposure time (h)	Cycles	Comments	Growth rate/mass gain After 168h	Comments	
304L (Fe-18.5Cr-10.2Ni)	Austenite	AA	168	-	-	1.34 mg/cm^2	-	
		Spallation	Comments	Thickness (µm)	**Growth rate (µm/h)**	Type of oxide 24h	Comments	Corrosion regime
304L (Fe-18.5Cr-10.2Ni)	Austenite	-	Is not discussed in the article	6-9 (mean: 7.5)	(mean: 0.04464286)	Fe_2O_3 and Fe_3O_4	Formation of K_2CrO_4 (Potassium chromate)	Secondary

Table A.11: *Article 6 (1/2): Kinetics of breakaway oxidation of Fe-Cr and Fe-Cr-Ni alloys in dry and wet carbon dioxide [60].*

Temperature: 650 °C								
Alloys	**Microstructure**	**Environment: dry carbon dioxide (Ar-20CO_2)**						
		Behavior	**Exposure time (h)**	**Cycles**	**Comments**	**Growth rate/mass gain 336h reaction**	**Comments**	
Fe-20Cr	Ferrite	AA	Different for different cases	-	-	∼1.5 mg/cm^2	20% nodule surface area fraction	
Fe-25Cr	Ferrite	AA	Different for different cases	-	-	∼1.7 mg/cm^2	47% nodule surface area fraction	
Fe-20Cr-10Ni	Austenite+Ferrite	Showed limited breakaway	Different for different cases	-	-	∼1 mg/cm^2	21% nodule surface area fraction	
Fe-20Cr-20Ni	Austenite	Showed limited breakaway	Different for different cases	-	-	<0.5 mg/cm^2	2% nodule surface area fraction	
Fe-25Cr-10Ni	Austenite+Ferrite	POS	Different for different cases	-	-	-	-	
Fe-25Cr-20Ni	Austenite	POS	Different for different cases	-	-	-	-	
		Spallation	**Comments**	**Thickness (µm)**	**Growth rate (µm/h)**	**Type of oxide**	**Comments**	**Corrosion regime**
Fe-20Cr	Ferrite	-	Not discussed in the article	-	-	Cr_2O_3, Fe_3O_4 and Fe_2O_3	-	Primary + Secondary
Fe-25Cr	Ferrite	-	Not discussed in the article	-	-	Cr_2O_3, Fe_3O_4 and Fe_2O_3	-	Primary + Secondary
Fe-20Cr-10Ni	Austenite+Ferrite	-	Not discussed in the article	-	-	Cr_2O_3, Fe_3O_4 and Fe_2O_3	-	Primary + Secondary
Fe-20Cr-20Ni	Austenite	-	Not discussed in the article	-	-	Cr_2O_3, Fe_3O_4 and Fe_2O_3	-	Primary + Secondary
Fe-25Cr-10Ni	Austenite+Ferrite	-	Not discussed in the article	-	-	Cr_2O_3	-	Primary
Fe-25Cr-20Ni	Austenite	-	Not discussed in the article	-	-	Cr_2O_3	-	Primary

Table A.12: *Article 6 (2/2): Kinetics of breakaway oxidation of Fe-Cr and Fe-Cr-Ni alloys in dry and wet carbon dioxide [60].*

Temperature: 650 °C								
Alloys	**Microstructure**	**Environment: wet carbon dioxide (Ar-20CO_2-20H_2O)**						
		Behavior	**Exposure time (h)**	**Cycles**	**Comments**	**Growth rate/mass gain 336h reaction**	**Comments**	
Fe-20Cr	Ferrite	AA	120	-	-	∼17 mg/cm^2	100% nodule surface area fraction	
Fe-25Cr	Ferrite	AA	120	-	-	∼7.5 mg/cm^2	100% nodule surface area fraction	
Fe-20Cr-10Ni	Austenite+Ferrite	Showed limited breakaway	120	-	-	<1 mg/cm^2	10% nodule surface area fraction	
Fe-20Cr-20Ni	Austenite	Showed limited breakway	120	-	-	∼0.5 mg/cm^2	14% nodule surface area fraction	
Fe-25Cr-10Ni	Austenite+Ferrite	POS	120	-	-	-	-	
Fe-25Cr-20Ni	Austenite	POS	120	-	-	-	-	
		Spallation	**Comments**	**Thickness (µm)**	**Growth rate (µm/h)**	**Type of oxide**	**Comments**	**Corrosion regime**
Fe-20Cr	Ferrite	-	Not discussed in the article	-	-	Cr_2O_3, Fe_3O_4 and Fe_2O_3	-	Secondary
Fe-25Cr	Ferrite	-	Not discussed in the article	-	-	Cr_2O_3, Fe_3O_4 and Fe_2O_3	-	Secondary
Fe-20Cr-10Ni	Austenite+Ferrite	-	Not discussed in the article	-	-	Cr_2O_3, Fe_3O_4 and Fe_2O_3	-	Primary + Secondary
Fe-20Cr-20Ni	Austenite	-	Not discussed in the article	-	-	Cr_2O_3, Fe_3O_4 and Fe_2O_3	-	Primary + Secondary
Fe-25Cr-10Ni	Austenite+Ferrite	-	Not discussed in the article	-	-	Cr_2O_3	-	Primary
Fe-25Cr-20Ni	Austenite	-	Not discussed in the article	-	-	Cr_2O_3	-	Primary

Table A.13: *Article 7 (1/1): Oxidation of a Fe-18Cr-8Ni austenitic stainless steel at 850 °C in O_2: Microstructure evolution during breakaway oxidation [61].*

Environment: O_2								
Alloys	**Microstructure**	**Temperature: 850 °C**						
		Behavior	**Exposure time (h)**	**Cycles**	**Comments**	**Growth rate/mass gain**	**Comments**	
AISI 304L (Fe-18Cr-8Ni)	Austenite	POS	48-96	-	-	No mass gain -time curve found in article -	-	
		Spallation	**Comments**	**Thickness (µm)**	**Growth rate (µm/h)**	**Type of oxide 72h**	**Comments**	**Corrosion regime**
AISI 304L (Fe-18Cr-8Ni)	Austenite	No	-	∼6	-	$Fe_{2-x}Cr_xO_3$ Cr_2O_3 and $MnCr_2O_4$	90% of spectra 10% of spectra	Primary
		Temperature: 600 °C						
		Behavior	**Exposure time (h)**	**Cycles**	**Comments**	**Growth rate/mass gain After 168h**	**Comments**	
AISI 304L (Fe-18Cr-8Ni)	Austenite	AAS	110-312	-	-	No mass gain -time curve found in the article	Rapid oxide growth	
		Spallation	**Comments**	**Thickness (µm)**	**Growth rate (µm/h)**	**Type of oxide 312h**	**Comments**	**Corrosion regime**
AISI 304L (Fe-18Cr-8Ni)	Austenite	Yes	During cooling and metallographic preparation	-	-	Fe_2O_3 (hematite) and small amount of Fe-rich corondum-type solid solution $Fe_{2-x}Cr_xO_3$ Fe-Cr spinel-type oxide	60% of spectra Unspalled area 40% of spectra Spalled area	Secondary

Table A.14: *Article 8 (1/2): Temperature and water vapour effects on the cyclic oxidation behaviour of Fe-Cr alloys [48].*

Temperature: 600 °C								
Alloys	**Microstructure**	**Environment: Ar-20O_2 (in vol.%)**						
		Behavior	**Exposure time (h)**	**Cycles**	**Comments** **Number of cycles inducing onset of breakaway oxidation**	**Growth rate/mass gain** **400 cycles** **(value from the article)**	Comments	
Fe-9Cr	Ferrite	-	-	400x1hr	10min in a cooling zone at 80 °C	∼11 (10) mg/cm^2	<5 cycles	
Fe-17Cr	Ferrite	-	-	400x1hr	-	∼4 (4) mg/cm^2	∼40 cycles	
Fe-25Cr	Ferrite	-	-	400x1hr	-	∼3.25 (3) mg/cm^2	∼40 cycles	
		Spallation	**Comments**	**Thickness (µm)**	**Growth rate (µm/h)**	**Type of oxide** **Scale surface oxide identified by XRD after indicated number of cycles**	**Comments** **The different layers from top to bottom**	**Corrosion regime**
Fe-9Cr	Ferrite	No	-	∼41.8 (500 cycles)	0.08360	Fe_2O_3	$Fe_2O_3/Fe_3O_4/Fe_3O_4$ + spinel/ mixed oxides	Secondary
Fe-17Cr	Ferrite	No	-	28.9	0.07225	Fe_2O_3 and trace of Cr_2O_3	-	Secondary
Fe-25Cr	Ferrite	No	-	∼47 (400 cycles)	0.11750	Fe_2O_3	Fe_2O_3/Fe_3O_4 and Fe_3O_4 + spinel/ discont. Cr_2O_3	Secondary
		Environment: Ar-20O_2-5H_2O (in vol.%)						
		Behavior	**Exposure time (h)**	**Cycles**	**Comments**	**Growth rate/mass gain** **400 cycles** **(value from the article)**	**Comments**	
Fe-9Cr	Ferrite	-	-	400x1hr	-	∼16 (16) mg/cm^2	<5 cycles	
Fe-17Cr	Ferrite	-	-	400x1hr	-	∼13 (13) mg/cm^2	∼20 cycles	
Fe-25Cr	Ferrite	-	-	400x1hr	-	∼1.6 (1.5) mg/cm^2	∼160 cycles	
		Spallation	**Comments**	**Thickness (µm)**	**Growth rate (µm/h)**	**Type of oxide** **Scale surface oxide identified by XRD after indicated number of cycles**	**Comments** **The different layers from top to bottom**	**Corrosion regime**
Fe-9Cr	Ferrite	No	-	∼50.9 (gap) and ∼41.8 (500 cycles)	0.08360	Fe_2O_3	$Fe_2O_3/Fe_3O_4/Fe_3O_4$ + spinel and gap/mixed oxides	Secondary
Fe-17Cr	Ferrite	No	-	∼95.6 (400 cycles)	0.23900	Fe_2O_3	Fe_2O_3/Fe_3O_4/(Fe/Cr oxide)/ mixed oxide	Secondary
Fe-25Cr	Ferrite	No	-	(400 cycles)	-	Cr_2O_3 and Fe_2O_3	Thin chromia scale with iron-rich oxide nodules at corners and edges	Primary + Secondary?

Table A.15: *Article 8 (2/2): Temperature and water vapour effects on the cyclic oxidation behaviour of Fe-Cr alloys [48].*

Temperature: 700 °C								
Alloys	**Microstructure**	**Environment Ar-20O_2 (in vol.%)**						
		Behavior	**Exposure time (h)**	**Cycles**	**Comments** **Number of cycles inducing onset of breakaway oxidation**	**Growth rate/mass gain** **180 cycles** **(value from the article)**	**Comments**	
Fe-9Cr	Ferrite	-	-	260x1hr	10min in a cooling zone at 80 °C	40 mg/cm^2	<5 cycles	
Fe-17Cr	Ferrite	-	-	260x1hr	-	0.2 mg/cm^2	>260 cycles	
Fe-25Cr	Ferrite	-	-	260x1hr	-	0.2 mg/cm^2	>400 cycles	
		Spallation	**Comments**	**Thickness (µm)**	**Growth rate (µm/h)**	**Type of oxide** **Scale surface oxide identified by XRD after indicated number of cycles**	**Comments**	**Corrosion regime**
Fe-9Cr	Ferrite	No	-	∼295.5 (180 cycles)	1.64167	Fe_2O_3	-	Secondary
Fe-17Cr	Ferrite	No	-	(260 cycles)	-	Cr_2O_3	-	Primary
Fe-25Cr	Ferrite	No	-	-	-	Cr_2O_3	-	Primary
		Environment: Ar-20O_2-5H_2O (in vol.%)						
		Behavior	**Exposure time (h)**	**Cycles**	**Comments**	**Growth rate/mass gain** **180 cycles** **(value from the article)**	**Comments**	
Fe-9Cr	Ferrite	-	-	-	-	30 mg/cm^2	<5 cycles	
Fe-17Cr	Ferrite	-	-	-	-	24 mg/cm^2	<5 cycles	
Fe-25Cr	Ferrite	-	-	-	-	0.2 mg/cm^2	>400 cycles	
		Spallation	**Comments**	**Thickness (µm)**	**Growth rate (µm/h)**	**Type of oxide** **Scale surface oxide identified by XRD after indicated number of cycles**	**Comments** **The different layers from top to bottom**	**Corrosion regime**
Fe-9Cr	Ferrite	No	-	∼311.1 (260 cycles)	1.19654	Fe_2O_3	$Fe_2O_3/Fe_3O_4/Fe_3O_4$ + spinel	Secondary
Fe-17Cr	Ferrite	No	-	∼217.6 (260 cycles)	0.83692	Fe_2O_3	Fe_2O_3/Fe_3O_4 and gap/ $FeCr_2O_4$ + Fe_3O_4	Secondary
Fe-25Cr	Ferrite	No	-	-	-	Cr_2O_3	-	Primary

Table A.16: *Article 9 (1/1): Effect of water vapour on cyclic oxidation of Fe-Cr alloys [50].*

Temperature: 700 °C								
Alloys	**Microstructure**	**Environment:Ar-20O_2-5H_2O (in vol.%)**						
		Behavior	**Exposure time (h)**	**Cycles**	**Comments**	**Mass gain (mg/cm2)∼260 cycles**	**Comments**	
Fe-9Cr	Ferrite	-	-	1hr x	10min at 80 °C	38	Parabolic	
Fe-17Cr	Ferrite	-	-	1hr x	10min at 80 °C	30	Parabolic	
Fe-25Cr	Ferrite	-	-	1hr x	10min at 80 °C	0.2	(400 cycles)	
		Spallation	**Comments**	**Thickness (µm) 260 cycles**	**Growth rate (µm/h)**	**Type of oxide Outermost**	**Comments**	**Corrosion regime**
Fe-9Cr	Ferrite	No	-	311	1.196154	Fe_2O_3	Fe_2O_3/Fe_2O_4/Fe_3O_4+spinel	Secondary
Fe-17Cr	Ferrite	No	-	222	0.853846	Fe_2O_3	Fe_2O_3/Fe_2O_4/Fe_3O_4+spinel. Gaps	Secondary
Fe-25Cr	Ferrite	Yes	-	-	-	Cr_2O_3	-	Primary
		Environment:Ar-5O_2-20H_2O (in vol.%)						
		Behavior	**Exposure time (h)**	**Cycles**	**Comments**	**Mass gain (mg/cm^2) 260 cycles**	**Comments**	
Fe-9Cr	Ferrite	-	-	-	-	55	Mass gain faster than lower water	
Fe-17Cr	Ferrite	-	-	-	-	34	-	
Fe-25Cr	Ferrite	-	-	-	-	4	-	
		Spallation	**Comments**	**Thickness (µm)**	**Growth rate (µm/h)**	**Type of oxide Outermost**	**Comments**	**Corrosion regime**
Fe-9Cr	Ferrite	-	-	Not showed in articles	-	Fe_2O_3	-	Secondary
Fe-17Cr	Ferrite	-	-	But similar to 5H_2O	-	Fe_2O_3	-	Secondary
Fe-25Cr	Ferrite	Yes	-	-	-	$(Fe,Cr)_2O_3$ + Cr_2O_3	Nodules	Primary+secondary

Table A.17: *Article 10 (1/2): Comparison of Short-Term Oxidation Behavior of Model and Commercial Chromia-Forming Ferritic Stainless Steels in Dry and Wet Air [62].*

Temperature: 700 °C								
Alloys	**Microstructure**	**Environment: Dry air**						
		Behavior	**Exposure time**	**Cycles**	**Comments**	**mass gain (mg/cm^2)**	**Comments**	
Fe-20Cr	Ferrite	-	24	-	-	0.06 ± 0.02	-	
430 (Fe-16.18Cr-0.47Ni)	Ferrite	-	24	-	-	0.02 ± 0.01	-	
		Spallation	**Comments**	**Thickness (µm)**	**Growth rate (µm/h)**	**Type of oxide**	**Comments**	**Corrosion regime**
Fe-20Cr	Ferrite	-	-	-	-	-	Thin, adherent oxide scale	Primary
430 (Fe-16.18Cr-0.47Ni)	Ferrite	-	-	-	-	-	Thin, adherent oxide scale	Primary
		Environment: Wet air (10% water vapor)						
		Behavior	**Exposure time**	**Cycles**	**Comments**	**mass gain (mg/cm^2)**	**Comments**	
Fe-20Cr	Ferrite	-	24	-	-	7.03 ± 0.84	-	
430 (Fe-16.18Cr-0.47Ni)	Ferrite	-	24	-	-	0.06 ± 0.03	-	
		Spallation	**Comments**	**Thickness (µm)**	**Growth rate (µm/h)**	**Type of oxide**	**Comments**	**Corrosion regime**
Fe-20Cr	Ferrite	-	-	∼50-70	-	Outer scale: hematite	Outer region of Fe-oxide and an inner subscale of Fe-Cr rich oxide	Secondary
430 (Fe-16.18Cr-0.47Ni)	Ferrite	-	-	-	-	-	Thin, adherent oxide scale	Primary

Table A.18: *Article 10 (2/2): Comparison of Short-Term Oxidation Behavior of Model and Commercial Chromia-Forming Ferritic Stainless Steels in Dry and Wet Air [62].*

Temperature: 800 °C								
Alloys	**Microstructure**	**Environment: Dry air**						
		Behavior	**Exposure time**	**Cycles**	**Comments**	**mass gain (mg/cm^2)**	**Comments**	
Fe-20Cr	Ferrite	-	24	-	-	0.15 ± 0.01	-	
430 (Fe-16.18Cr-0.47Ni)	Ferrite	-	24	-	-	0.10± 0.01	-	
		Spallation	**Comments**	**Thickness (µm)**	**Growth rate (µm/h)**	**Type of oxide**	**Comments**	**Corrosion regime**
Fe-20Cr	Ferrite	-	-	∼2-2.5	0.10417	Cr_2O_3	Thin, adherent oxide scale Voids at alloy-oxide interface	Primary
430 (Fe-16.18Cr-0.47Ni)	Ferrite	-	-	∼1	0.04167	Outer: $(Cr,Mn)_3O_4$ spinel Inner: Cr_2O_3 and SiO_2 at alloy-oxide interface	Thin, adherent oxide scale Voids	Primary
		Environment: Wet air (10% water vapor)						
		Behavior	**Exposure time**	**Cycles**	**Comments**	**mass gain (mg/cm^2)**	**Comments**	
Fe-20Cr	Ferrite	-	24	-	-	0.13 ± 0.01	-	
430 (Fe-16.18Cr-0.47Ni)	Ferrite	-	24	-	-	0.10 ± 0.02	-	
		Spallation	**Comments**	**Thickness (µm)**	**Growth rate (µm/h)**	**Type of oxide**	**Comments**	**Corrosion regime**
Fe-20Cr	Ferrite	-	-	∼1-1.3	-	Cr_2O_3 with little Fe incorporation in the outer scale	Thin, adherent oxide scale Voids at alloy-oxide interface	Secondary (100-200 h)
430 (Fe-16.18Cr-0.47Ni)	Ferrite	-	-	∼1	-	Outer: $(Cr,Mn)_3O_4$ with little Fe incorporation Inner: Cr_2O_3 and Si enrichment at the alloy-oxide interface	Thin, adherent oxide scale Voids	Primary

Table A.19: *Article 11 (1/1): Oxidation of an austenitic stainless steel with or without alloyed aluminum in O_2 + 10% H_2O environment at 800 °C [63].*

Environment: O_2 + 10% H_2O								
Alloys	**Microstructure**	**Temperature: 800 °C**						
		Behavior	**Exposure time (h) Short-term ox.**	**Cycles**	**Comments**	**Growth rate/mass gain**	**Comments**	
AFA (Fe-14.5r-20Ni-2.7Al)	Austenite	-	20	-	Mass change was discontinuous recorded every 20h exposure	-	Mass change was discontinuous recorded every 20h exposure	
CSS (Fe-14.9Cr-20.5Ni)	Austenite	-	20	-	-	-	-	
		Spallation	**Comments**	**Thickness (µm)**	**Growth rate (µm/h)**	**Type of oxide**	**Comments**	**Corrosion regime**
AFA (Fe-14.5r-20Ni-2.7Al)	Austenite	No	-	-	-	-	-	-
CSS (Fe-14.9Cr-20.5Ni)	Austenite	-	-	∼4-10	0.35000	-	-	-
		Behavior	**Exposure time (h) Long-term ox.**	**Cycles**	**Comments**	**Growth rate/mass gain**	**Comments**	
AFA (Fe-14.5r-20Ni-2.7Al)	Austenite	-	100	-	-	Mass change was discontinuous recorded every 20h exposure	-	
CSS (Fe-14.9Cr-20.5Ni)	Austenite	-	100	-	-	-	-	
		Spallation	**Comments**	**Thickness (µm)**	**Growth rate (µm/h)**	**Type of oxide**	**Comments**	**Corrosion regime**
AFA (Fe-14.5r-20Ni-2.7Al)	Austenite	-	-	-	-	-	-	-
CSS (Fe-14.9Cr-20.5Ni)	Austenite	-	-	-	-	-	-	-

Table A.20: *Article 12 (1/1): Investigation of high temperature corrosion behavior on 304L austenite stainless steel in corrosive enviroments [64].*

Temperature: 700 °C								
Alloys	**Microstructure**	**Environment: Molten salt (NaCl-50% Na_2SO_4)**						
		Behavior	**Exposure time (h)**	**Cycles**	**Comments**	**Mass gain(mg/cm^2)**	**Comments**	
304L (Fe-16Cr-12.20Ni)	Austenite	-	10	-	-	-0,8487 -	-	
		Spallation	**Comments**	**Thickness (µm)**	**Growth rate (µm/h)**	**Type of oxide**	**Comments**	**Corrosion regime**
304L (Fe-16Cr-12.20Ni)	Austenite	Yes	-	6.25	0.650	Fe_3O_4, chromium manganese nickle and chromium manganese oxide	Dense but non-continuous oxide layer	Secondary
		Environment: Molten salt + Dry oxygen						
		Behavior	**Exposure time (h)**	**Cycles**	**Comments**	**Mass gain (mg/cm^2)**	**Comments**	
304L (Fe-16Cr-12.20Ni)	Austenite	-	10	-	-	-	-13.5225	Mass loss due to the mixture of salt deposit and oxide scale peeled-off in the destilled water
		Spallation	**Comments**	**Thickness (µm)**	**Growth rate (µm/h)**	**Type of oxide**	**Comments**	**Corrosion regime**
304L (Fe-16Cr-12.20Ni)	Austenite	Yes	-	41	4.1	Fe_3O_4, chromium nickel (Cr_2Ni_3), pure Ni and iron nickel (Cu0.333Fe0.333Ni0.334)	Porous oxide layer with some cracks on the substrate	Secondary

Table A.21: *Article 13 (1/2): Corrosion behavior of T24, T92, VM12 and AISI 304 steels exposed to KCl-NaCl-K_2SO_4 salt mixtures [57].*

Temperature: 650 °C								
Alloys	**Microstructure**	**Environment: H_2O + CO_2 without salt deposits**						
		Behavior	**Exposure time**	**Cycles**	**Comments**	**mass gain (mg/cm^2)**	**Comments**	
T24 (Fe-2.4Cr)	Ferrite- Martensite	-	360	-	-	19	-	
T92 (Fe-9Cr-0.3Ni)	Ferrite- Martensite	-	360	-	-	2.5	-	
VM12 (Fe-12Cr-0.3Ni)	Ferrite- Martensite	-	360	-	-	5	-	
AISI 304 (Fe-17.3Cr-8Ni)	Austenite	-	360	-	-	4	-	
		Spallation	**Comments Average metal loss absolute values (µm)**	**Thickness (µm)**	**Growth rate (µm/h)**	**Type of oxide**	**Comments**	**Corrosion regime**
T24 (Fe-2.4Cr)	Ferrite- Martensite	Yes	165	120	0.333333	Fe2O3 & Fe3O4	-	Secondary
T92 (Fe-9Cr-0.3Ni)	Ferrite- Martensite	No	65	25	0.069444	Fe_2O_3 & Cr-rich oxides	-	Secondary
VM12 (Fe-12Cr-0.3Ni)	Ferrite- Martensite	No	90	25	0.069444	Fe_2O_3 & Cr-rich oxides	-	Secondary
AISI 304 (Fe-17.3Cr-8Ni)	Austenite	No	65	13	0.036111	Cr-rich oxides	-	Primary
Alloys	**Microstructure**	**Environment: NaCl-KCl**						
		Behavior	**Exposure time**	**Cycles**	**Comments**	**mass gain (mg/cm^2)**	**Comments**	
T24 (Fe-2.4Cr)	Ferrite- Martensite	-	360	-	-	59	-	
T92 (Fe-9Cr-0.3Ni)	Ferrite- Martensite	-	360	-	-	68	-	
VM12 (Fe-12Cr-0.3Ni)	Ferrite- Martensite	-	360	-	-	81	-	
AISI 304 (Fe-17.3Cr-8Ni)	Austenite	-	360	-	-	41	-	
		Spallation	**Comments Average metal loss absolute values (µm)**	**Thickness (µm)**	**Growth rate (µm/h)**	**Type of oxide**	**Comments**	**Corrosion regime**
T24 (Fe-2.4Cr)	Ferrite- Martensite	Yes	640	-	-	-	-	Secondary
T92 (Fe-9Cr-0.3Ni)	Ferrite- Martensite	-	420	-	-	-	-	Secondary
VM12 (Fe-12Cr-0.3Ni)	Ferrite- Martensite	-	600	-	-	-	-	Secondary
AISI 304 (Fe-17.3Cr-8Ni)	Austenite	-	400	-	-	-	-	Secondary

Table A.22: *Article 13 (2/2): Corrosion behavior of T24, T92, VM12 and AISI 304 steels exposed to KCl-NaCl-K_2SO_4 salt mixtures [57].*

Temperature: 650 °C								
Alloys	**Microstructure**	**Environment: NaCl-Na_2SO_4**						
		Behavior	**Exposure time**	**Cycles**	**Comments**	**mass gain (mg/cm^2)**	**Comments**	
T24 (Fe-2.4Cr)	Ferrite- Martensite	-	360	-	-	34	-	
T92 (Fe-9Cr-0.3Ni)	Ferrite- Martensite	-	360	-	-	34	-	
VM12 (Fe-12Cr-0.3Ni)	Ferrite- Martensite	-	360	-	-	32	-	
AISI 304 (Fe-17.3Cr-8Ni)	Austenite	-	360	-	-	28	-	
		Spallation	**Comments Average metal loss absolute values (µm)**	**Thickness (µm)**	**Growth rate (µm/h)**	**Type of oxide**	**Comments**	**Corrosion regime**
T24 (Fe-2.4Cr)	Ferrite-Martensite	No	420	-	-	-	Cracks	Secondary
T92 (Fe-9Cr-0.3Ni)	Ferrite-Martensite	-	350	-	-	-	-	Secondary
VM12 (Fe-12Cr-0.3Ni)	Ferrite-Martensite	-	410	-	-	-	Intergranular corrosion	Secondary
AISI 304 (Fe-17.3Cr-8Ni)	Austenite	-	340	-	-	-	Intergranular corrosion	Secondary
Alloys	**Microstructure**	**Environment: NaCl-K_2SO_4**						
		Behavior	**Exposure time**	**Cycles**	**Comments**	**mass gain (mg/cm^2)**	**Comments**	
T24 (Fe-2.4Cr)	Ferrite- Martensite	-	360	-	-	43	-	
T92 (Fe-9Cr-0.3Ni)	Ferrite- Martensite	-	360	-	-	42	-	
VM12 (Fe-12Cr-0.3Ni)	Ferrite- Martensite	-	360	-	-	20	-	
AISI 304 (Fe-17.3Cr-8Ni)	Austenite	-	360	-	-	5	-	
		Spallation	**Comments Average metal loss absolute values (µm)**	**Thickness (µm)**	**Growth rate (µm/h)**	**Type of oxide**	**Comments**	**Corrosion regime**
T24 (Fe-2.4Cr)	Ferrite-Martensite	-	430	-	-	-	-	Secondary
T92 (Fe-9Cr-0.3Ni)	Ferrite-Martensite	-	250	-	-	-	-	Secondary
VM12 (Fe-12Cr-0.3Ni)	Ferrite-Martensite	-	200	-	-	-	-	Secondary
AISI 304 (Fe-17.3Cr-8Ni)	Austenite	-	180	-	-	-	-	-

Table A.23: *Article 14 (1/1): Microstructural understanding of the oxidation of an austenitic stainless steel in high-temperature steam through advanced characterization [65].*

Environment: Steam								
Alloys	**Microstructure**	**Temperature: 600 °C**						
		Behavior	**Exposure time (h)**	**Cycles**	**Comments**	**mass gain (mg/cm^2)**	**Comments**	
Stainless steel (Fe-17Cr-9Ni)	Austenite	-	1500	-	-	-	-	
		Spallation	**Comments**	**Thickness (µm)**	**Growth rate (µm/h)**	**Type of oxide**	**Comments**	**Corrosion regime**
Stainless steel (Fe-17Cr-9Ni)	Austenite	-	-	120	0.080000	∼50µm outer Fe-rich layer ∼60µm inner Cr-rich layer ∼10µm beneath the outer-inner oxide layers	-	Secondary

Table A.24: *Article 15 (1/1): Influence of Cr content on the Corrosion of Fe-Cr Alloys: Synergistic Effect of NaCl and water vapor [66].*

Temperature: 600 °C								
Alloys	**Microstructure**	**Environment:Air + NaCl**						
		Behavior	**Exposure time (h)**	**Cycles**	**Comments**	**Mass gain (mg/cm^2)**	**Comments**	
Fe-5Cr	Ferrite	-	10	-	-	1.8	-	
Fe-15Cr	Ferrite	-	10	-	-	1.9	-	
Fe-25Cr	Ferrite	-	10	-	-	2.9	-	
		Spallation	**Comments**	**Thickness (µm)**	**Growth rate (µm/h)**	**Type of oxide Outermost**	**Comments**	**Corrosion regime**
Fe-5Cr	Ferrite	-	-	-	-	-	-	-
Fe-15Cr	Ferrite	-	-	-	-	-	-	-
Fe-25Cr	Ferrite	-	-	-	-	-	-	-
		Environment: O_2 + H_2O + NaCl						
		Behavior	**Exposure time (h)**	**Cycles**	**Comments**	**Mass gain (mg/cm^2)**	**Comments**	
Fe-5Cr	Ferrite	-	10	-	-	6	-	
Fe-15Cr	Ferrite	-	10	-	-	9	-	
Fe-25Cr	Ferrite	-	10	-	-	13	-	
		Spallation	**Comments**	**Thickness (µm)**	**Growth rate (µm/h)**	**Type of oxide Outermost**	**Comments**	**Corrosion regime**
Fe-5Cr	Ferrite	-	-	-	-	-	-	-
Fe-15Cr	Ferrite	-	-	-	-	-	-	-
Fe-25Cr	Ferrite	-	-	146	-	-	-	secondary

Table A.25: *Article 16 (1/1): Studies on the corrosion behavior of Fe-20Cr alloy in NaCl solution spray at 600 °C [41].*

Temperature: 600 °C								
Alloys	**Microstructure**	**Environment: NaCl solution spray**						
		Behavior	**Exposure time (h)**	**Cycles**	**Comments**	**Mass gain (mg/cm^2)**	**Comments**	
Fe-20Cr	-	-	20	-	-	6.8 -	-	
		Spallation	**Comments**	**Thickness (µm)**	**Growth rate (µm/h)**	**Type of oxide**	**Comments**	**Corrosion regime**
Fe-20Cr	-	No	Not discussed	53	2.65	Hematite (Fe_2O_3) & Chromite ($FeCr_2O_4$)	Outer: porous with many clear voids (29) inner: dense and no voids (24)	Secondary
		Environment: Solid NaCl deposit in water vapor						
		Behavior	**Exposure time (h)**	**Cycles**	**Comments**	**Mass gain (mg/cm^2)**	**Comments**	
Fe-20Cr	-	-	20	-	-	6.2	-	
		Spallation	**Comments**	**Thickness (µm)**	**Growth rate (µm/h)**	**Type of oxide**	**Comments**	**Corrosion regime**
Fe-20Cr	-	Yes	Poorly adherent	85	4.25	Fe_2O_3, $FeCr_2O_4$, Cr_2O_3 Na_2CrO_4 & residual NaCl	Thick, porous, heavily cracked and poor adherence with substrate	Secondary

Table A.26: *Article 17 (1/1): Corrosion behaviour of various alloys with NaCl-KCl coating [67].*

Temperature: 670 °C										
Environment: Environment: NaCl-KCl (1:1 molar ratio) deposit in air										
Alloys	**Microstructure**	**Behavior**	**Exposure time**	**Cycles**	**Comments**	**Mass loss (mg/cm^2)**	**Comments**			
Fe-10Al(at.%)	-	-	48	-		55	-			
Fe-20Al(at.%)	-	-	48	-	-	53	-			
Fe-45Al(at.%)	-	-	48	-	-	15	-			
Fe-21Cr-5Al(wt.%)	Ferrite	-	48	-	-	90	-			
Fe-35Cr(wt.%)	Ferrite	-	49	-	-	110	-			
		Spallation	**Comments**	**Thickness (µm)**	**Growth rate (µm/h)**	**Type of oxide**	**Comments**	**Corrosion regime**		
Fe-10Al(at.%)	-	-	-	356	7.416666	Fe_2O_3 & Fe/Al oxide	-	Secondary		
Fe-20Al(at.%)	-	-	-	511	10.645833	Fe_2O_3 & Al-rich oxide	-	Secondary		
Fe-45Al(at.%)	-	-	-	?	-	Al_2O_3+salt, Fe+Al-rich oxide, Fe bulk	-	Secondary		
Fe-21Cr-5Al(wt.%)	Ferrite	-	-	1320	27.5	Fe_2O_3, Al-rich Cr oxide & Fe+K/Cr oxie	-	Secondary		
Fe-35Cr(wt.%)	Ferrite	-	-	1156?	-	Fe_2O_3 & Fe/Cr oxide	-	Secondary		

Table A.27: *Article 18 (1/1): Internal Oxidation of Fe-Al Alloys in a KCl-Air Atmosphere at 650 °C [68].*

Temperature: 650 °C								
Alloys	**Microstructure**	**Environment: Air**						
		Behavior	**Exposure time (h)**	**Cycles**	**Comments**	**Mass gain (mg/cm^2)**	**Comments**	
Fe-10Al	-	-	96	-	-	1.6	-	
Fe-20Al	-	-	96	-	-	0.40	-	
Fe-45Al	-	-	96	-	-	-	-	
		Spallation	**Comments**	**Thickness (µm)**	**Growth rate (µm/h)**	**Type of oxide**	**Comments**	**Corrosion regime**
Fe-10Al	-	Yes	During cooling	11	0.1145833	Porous Fe_2O_3 spalled of, leaving an alumina-rich region on the alloy surface mixed with iron oxide	-	-
Fe-20Al	-	No	-	-	-	Well-adhearing alumina film with some Fe_2O_3 nodules	-	-
Fe-45Al	-	No	-	-	-	Cr_2O_3	-	-
		Environment: Air with solid KCl crystals of 1 mm thickness for each sample						
		Behavior	**Exposure time (h)**	**Cycles**	**Comments**	**Mass gain (mg/cm^2) 200 h in KCl vapor-air mix.**	**Comments Metal loss (mg/cm^2) 48h**	
Fe-10Al	-	-	48	-	-	10	14.5	
Fe-20Al	-	-	48	-	-	15	15.9	
Fe-45Al	-	-	48	-	-	-	8.5	
		Spallation	**Comments**	**Thickness (µm)**	**Growth rate (µm/h)**	**Type of oxide**	**Comments**	**Corrosion regime**
Fe-10Al	-	-	-	80.8	1.171875	Fe_2O_3 and mixed oxides of iron and aluminium with potassium impurities	-	Secondary
Fe-20Al	-	-	-	90	0.066666	Fe_2O_3 and mixed oxides of iron and aluminium with potassium impurities zons	-	Secondary
Fe-45Al	-	-	-	-	-	-	-	-

Table A.28: *Article 19 (1/1): High temperature interaction of Al/Si-modified Fe-Cr alloys with KCl [69].*

Temperature: 650 °C								
Alloys	**Microstructure**	**Environment: KCl vapour-air mixture**						
		Behavior	**Exposure time**	**Cycles**	**Comments**	**Mass gain (mg/cm^2)**	**Comments**	
Fe-15Cr	Ferrite	-	48	-	-	6.5	-	
Fe-35Cr	Ferrite	-	48	-	-	1.6	-	
Fe-15Cr-5Al	-	-	48	-	-	2.6	-	
Fe-15Cr-Si	-	-	48	-	-	1.8	-	
Fe-21Cr-5Al	-	-	48	-	-	-	-	
HK40 (Fe-25Cr-20Ni)	Austenite	-	48	-	-	0.6	-	
		Spallation	**Comments**	**Thickness (µm)**	**Growth rate (µm/h)**	**Type of oxide**	**Comments**	**Corrosion regime**
Fe-15Cr	Ferrite	-	-	63	1.3125	Fe_2O_3 & Fe/Cr oxide & Cr-rich oxide	-	Secondary
Fe-35Cr	Ferrite	-	-	18.3	0.38125	Chromate and Cr-rich oxides	-	-
Fe-15Cr-5Al	-	-	-	-	-	-	-	-
Fe-15Cr-Si	-	-	-	-	-	Potassium chromate & silica-rich layer	-	-
Fe-21Cr-5Al	-	-	-	-	-	-	-	-
HK40 (Fe-25Cr-20Ni)	Austenite	-	-	-	-	-	-	-
		Environment: KCl deposit in air						
		Behavior	**Exposure time**	**Cycles**	**Comments**	**Mass loss (mg/cm^2)**	**Comments**	
Fe-15Cr	Ferrite	-	48	-	-	16	-	
Fe-35Cr	Ferrite	-	48	-	-	21	-	
Fe-15Cr-5Al	-	-	48	-	-	13	-	
Fe-15Cr-Si	-	-	48	-	-	6	-	
Fe-21Cr-5Al	-	-	48	-	-	-	-	
HK40 (Fe-25Cr-20Ni)	Austenite	-	48	-	-	12	-	
		Spallation	**Comments**	**Thickness (µm)**	**Growth rate (µm/h)**	**Type of oxide**	**Comments**	**Corrosion regime**
Fe-15Cr	Ferrite	-	-	38	0.791666	-	-	-
Fe-35Cr	Ferrite	-	-	173	3.604166	-	-	-
Fe-15Cr-5Al	-	-	-	55	1.145833	-	-	-
Fe-15Cr-Si	-	-	-	5	0.1041666	-	-	-
Fe-21Cr-5Al	-	-	-	-	-	-	-	-
HK40 (Fe-25Cr-20Ni)	Austenite	-	-	30	0.625	-	-	-

Table A.29: *Article 20 (1/1): Investigation of the HCI (g) attack on pre-oxidized pure Fe,Cr,Ni and commercial 304 steel at 400 °C [70]*

Temperature: 400 °C								
Alloys	**Microstructure**	**Environment: Pre-oxidized in N_2-10 vol.% O_2**						
		Behavior	**Exposure time (h)**	**Cycles**	**Comments**	**Mass gain (mg/cm^2**	**Comments**	
304 (Fe-18Cr-10Ni)	-	-	24	-	-	-	-	
		Spallation	**Comments**	**Thickness (µm)**	**Growth rate (µm/h)**	**Type of oxide**	**Comments**	**Corrosion regime**
304 (Fe-18Cr-10Ni)	-	No	-	0.040-0.075	0.001666-0.00313	Fe-rich (Cr-Fe)$_2$O$_3$ in the outer part and a Cr-rich (Cr, Fe)$_2$O$_3$ in the inner part	Thin, well adherent	Primary
		Environment: N_2-10 vol.% O_2 - 500 ppm HCl+ 5 vol.% H_20						
		Behavior	**Exposure time (h)**	**Cycles**	**Comments**	**Mass gain (mg/cm^2)**	**Comments**	
304 (Fe-18Cr-10Ni)	-	-	100	-	-	-	-	
		Spallation	**Comments**	**Thickness (µm)**	**Growth rate (µm/h)**	**Type of oxide**	**Comments**	**Corrosion regime**
304 (Fe-18Cr-10Ni)	-	No	-	-	-	Same as in pre-oxidized but thicker	-	Primary

Table A.30: *Article 21 (1/1): High temperature of pure Fe, Cr and Fe-Cr binary alloys in O_2 containing trace KCl vapour at 750 °C [42].*

Temperature: 750 °C								
Alloys	**Microstructure**	**Environment: O_2 containing 298 ppm KCl vapour**						
		Behavior	**Exposure time**	**Cycles**	**Comments**	**Mass gain (mg/cm^2)**	**Comments**	
Fe-20Cr	Ferrite	-	20	-		4	-	
Fe-40Cr	Ferrite	-	20	-	-	3.8	-	
Fe-60Cr	Ferrite	-	20	-	-	3.2	-	
Fe-80Cr	Ferrite	-	20	-	-	2.1	-	
		Spallation	**Comments**	**Thickness (µm)**	**Growth rate (µm/h)**	**Type of oxide**	**Comments**	**Corrosion regime**
Fe-20Cr	Ferrite	-	-	80	-	Fe_2O_3 and few Cr_2O_3	Multilayer and bad adhesion & nodules	Secondary
Fe-40Cr	Ferrite	-	-	107?	-	$K_2Cr_2O_7$ & Fe_2O_3	More dense than Fe20Cr	Secondary
Fe-60Cr	Ferrite	-	-	38	-	$K_2Cr_2O_7$	Monolayer oxide	Secondary
Fe-80Cr	Ferrite	-	-	23	-	$K_2Cr_2O_7$	Monolayer oxide	Secondary

B

Appendix

Theoretical calculated thickness

Table B.1: Constants and parameters used to calculate the theoretical thickness.

Compound	*Mass, m [g]*	*Density, ρ [g/cm^3]*	*Weight fraction oxygen, O_{wf}*
Fe_2O_3	160	5.24	0.3
Fe_3O_4	232	5.17	0.276

Δm = mass gain [mg/cm^2]

Fe_2O_3:

$$Theo.thickness[\mu m] = \frac{\Delta m}{O_{wf} \cdot \rho_{Fe_2O_3} \cdot 10^{-1}} \tag{B.1}$$

Fe_3O_4:

$$Theo.thickness[\mu m] = \frac{\Delta m}{O_{wf} \cdot \rho_{Fe_3O_4} \cdot 10^{-1}} \tag{B.2}$$

DEPARTMENT OF CHEMISTRY AND CHEMICAL ENGINEERING
CHALMERS UNIVERSITY OF TECHNOLOGY
Gothenburg, Sweden 2021
www.chalmers.se

CHALMERS
UNIVERSITY OF TECHNOLOGY